(43)

Transport Processes in Well Confined High Temperature Plasmas and Collective Modes in their Partially Ionized Edge Region

by

William Scott Daughton

Submitted to the Department of Physics
in partial fulfillment of the requirements for the degree of

Doctor of Philosophy

at the

MASSACHUSETTS INSTITUTE OF TECHNOLOGY

February 1998

Author .....
.....
Department of Physics
September 19, 1997

Certified by.....
.....
Bruno Coppi
Professor of Physics
Thesis Supervisor

Accepted by .....
.....
George Koster
Chairman, Department Committee on Graduate Students

Transport Processes in Well Confined High Temperature Plasmas and Collective Modes in their Partially Ionized Edge Region

by

William Scott Daughton

Submitted to the Department of Physics
on September 19, 1997, in partial fulfillment of the
requirements for the degree of
Doctor of Philosophy

Abstract

In a partially ionized plasma, the charged particle population is coupled to the neutrals through charge exchange, ionization and recombination. An interchange instability is identified in which the driving factor is the neutral pressure gradient and the dominant collisional process is charge exchange. Regimes are considered in which the mean free path for neutral-ion collisions λ_{ni} is small in comparison to the macroscopic length scales. The instability is analogous to a gravitational interchange mode with an effective gravity $g_{eff} = \nu_{in} V_n$. The neutral flow $V_n = -\nabla p_n/(m_i n_i \nu_{in})$ results from a balance between the neutral pressure gradient and collisional friction with the ions. Previous work involving instabilities with neutrals have treated the neutral population as a uniform background insensitive to the perturbations in the plasma. In this analysis, perturbations in both the plasma and the neutral population are considered. Since we assume interchange modes ($k_{||} = 0$) with small gyro-radius, fluid equations are used to describe the ions while the Boltzmann equation is used to describe the neutrals. Using the local approximation, a dispersion relation is found which is valid for arbitrary $k_y \lambda_{ni}$. The limits $k_y \lambda_{ni} \ll 1$ and $k_y \lambda_{ni} \gg 1$ are discussed and the intermediate limit $k_y \lambda_{ni} \sim 1$ is examined numerically. A normal mode analysis is performed using fluid equations for both the plasma and the neutral population and a solution is found for the very short wavelength modes. Some of the realistic conditions under the which the considered modes may be excited are analyzed. Finite parallel wavelength is of particular importance since for realistic values of $k_{||}$ a coupling occurs between the unstable interchange mode and a stabilizing shear Alfvén mode. For plasmas in which the frozen-in law is valid, this coupling can dramatically alter the condition under which the mode can exist. For plasmas with significant resistivity, the coupling to the shear Alfvén mode is weakened resulting in a considerable reduction of the growth rate. The effect of equilibrium $\mathbf{E} \times \mathbf{B}$ drifts on the analysis is discussed and the possible relevance to divertor plasmas is considered.

Starting from an analysis of the transport properties of the plasmas produced by

the Alcator C-Mod machine over a rather wide variety of conditions, a novel form of a thermal transport coefficient which reproduces both ohmic and auxiliary heated L-mode discharges has been identified. This thermal transport coefficient involves the difference of two terms, one representing the normal outward diffusion of thermal energy and the other corresponding to a process reducing the outward flux. There are in fact theoretical arguments in support of a composite transport coefficient based on the symmetry properties of an appropriate transport matrix. The coefficient includes the constraint of profile consistency and is inspired by the properties of the toroidal ion and electron temperature gradient modes. In a series of transport simulations for plasmas produced by the Alcator C-Mod machine, the thermal transport coefficient is shown to reproduce the observed electron temperature profile, stored energy and loop voltage. The relevant scaling for the energy confinement time is also composed of two terms. The L-mode database assembled for the ITER project is used to compare DIII-D, JET, JT60, PDX, TFTR, FTU, and Alcator C-Mod with this analysis. With the exception of PDX, the comparison is substantially better than standard L-mode power law scalings. Based on this analysis, an extrapolation is made for the confinement time of two proposed ignition experiments.

Thesis Supervisor: Bruno Coppi
Title: Professor of Physics

Acknowledgments

I would like to thank my thesis advisor Bruno Coppi for the guidance and support I received on this thesis and for the wealth of experience he has shared with me during my time at MIT. His approach to solving problems, his insight and his sheer enthusiasm for physics will serve as an inspiration for years to come.

I would like to acknowledge and thank Peter Catto and Sergei Krasheninnikov for their help relating to the work on partially ionized plasmas. Sergei first suggested to me that there might be a flute instability with the neutrals providing an effective gravity and Peter spent considerable time and effort checking over my calculations and offering suggestions on how to proceed.

A special thanks to John Belcher who agreed to serve as a reader with very short notice, allowing me to finish during the summer term. I would also like to thank Stefano Migliuolo for agreeing to serve as a reader on this thesis and for the advice and suggestions he has offered during my time at MIT. Stefano was always willing to check over any idea I might have and I am grateful for the time and effort he spent providing criticism and feedback.

This work was supported in part by the Computational Science Graduate Fellowship Program of the Office of Scientific Computing in the Department of Energy. I am very grateful for this support which lasted four years and included both tuition and a stipend.

I would like to thank Martin Greenwald and the Alcator C-Mod team for allowing me access to the Alcator transport data and Stan Kaye and the ITER group for providing access to the ITER transport database. I would like to acknowledge Steve Wolfe who first pointed out that the scalings I was considering had a significant off-set term. I would like to thank Linda Sugiyama who was very patient in helping me get started with the BALDUR code and Francesca Bombarda who was extremely helpful in answering questions about the experimental data from Alcator C-Mod.

Finally, I would like to thank my wife Diane for putting up with me through five years of graduate school and for giving me three beautiful daughters along the way.

Contents

List of Figures

List of Tables

Chapter 1

Overview

This thesis is composed of two parts, one dealing with interchange instabilities in partially ionized plasmas and the second dealing with the transport of thermal energy in high temperature plasmas. These topics represent two separate research efforts and no attempt has been made in this thesis to unify the results. The only clear connection which I can see between these two topics is that the energy transport problem depends on the edge temperature as a boundary condition. In turn, the edge temperature is determined by the relevant physics in the edge and divertor regions which are often coupled to a neutral population through charge exchange, ionization and recombination. Thus, instabilities in the edge and divertor regions of a toroidal plasma have the potential to influence the overall energy confinement. This general idea has been around for some time in connection with the observed confinement of H-mode discharges and will not be explored in this thesis. In this chapter, a brief overview of the research is given with an emphasis on the original results.

Interchange instabilities in a partially ionized plasmas are of potential importance to a broad range of applications in space and in the laboratory. Past efforts in this area have treated the neutral population as an immobile background. This is well justified in certain regimes where the neutral density greatly exceeds the ion density but there are plasmas in both space and the laboratory where the neutral and ion densities are comparable. In these regimes, the dynamics of both the plasma and the neutral population are of importance. In this analysis, a particular instability is

considered in which the driving factor is a gradient in the neutral pressure and the dominant coupling term between the ions and the neutrals is charge exchange. This instability belongs to a larger well-know class of interchange modes which are driven by a relative velocity between a plasma and a neutral background. Although the general mechanism of this type of instability is well-known, the effect of neutrals on the instability has never been examined. The results from this analysis indicate that these effects are substantial and should not be neglected in regimes where the plasma and neutrals are strongly coupled. A dispersion relationship is found which includes the effect of neutral perturbations on the instability and various limits are analyzed. It is pointed out that the realistic conditions under which the mode can exist are quite different than predicted by a simple flute-mode analysis. Finite parallel wavelength and the resulting coupling to a shear Alfvén mode are of particular importance in assessing the realistic instability condition. It is pointed out that the results of this analysis might have relevance to the divertor region of a toroidal plasma.

Transport phenomena in high energy plasmas is a topic of great importance to fusion research and to the scientific understanding of plasmas. It is pointed out that recent claims of a true "first-principles" calculation of this phenomena are probably overstated. Research efforts toward this goal are certainly important but relatively simple models for tokamak confinement are also useful both as a predictive tool and for better understanding the plasma behavior. A modest effort is presented here which attempts to develop a comparatively simple model for the thermal transport based on a few key observations and inspired by the properties of the modes thought to be responsible for the transport. A physical description of the basic properties of these modes is given in Chapter 3. There are two main results of this research : a new thermal transport coefficient for ohmic and L-mode discharges and a novel scaling for the confinement expressed in terms of the relevant dimensionless parameters. Both the transport coefficient and the confinement scaling are composed of two terms one of which is related to the normal outward diffusion of energy and one associated with a process which tends to reduce the outward flux. Theoretical arguments in support of such a diffusion coefficient are examined and supporting evidence is presented.

The scaling derived in this analysis fits a broad range of experiments substantially better than any previous scaling. In addition, the transport coefficient is shown to reproduce the temperature profiles of a broad range of discharges from the Alcator C-Mod machine. The result is interesting from a scientific point of view since it suggests that transport in high energy plasmas is the result of multiple processes. In addition, the results are of importance for estimating the expected confinement of experiments envisioned to operate at or near ignition conditions.

Chapter 2

Interchange Instabilities in a Partially Ionized Plasma

2.1 Introduction

Low temperature plasmas are often coupled to a neutral population through charge exchange or elastic collisions. The edge and divertor region of toroidal plasmas and the ionosphere are a few well-known examples. The presence of neutrals within a plasma can give rise to new instabilities in several ways. It is well-know that positive dissipation can cause negative energy waves to become unstable [1]. Thus, the dissipation introduced by ion-neutral collisions can allow certain instabilities to proceed that would not otherwise occur. For example, the dissipative velocity shear instability proposed by Basu and Coppi [2, 3] is driven by a gradient in the field-aligned ion flow velocity but requires ion-neutral collisions to proceed.

Another way in which a neutral population can give rise to a plasma instability is by providing an additional driving factor. In this paper, an instability is identified which is driven by a neutral flow velocity resulting from a neutral pressure gradient. The instability is directly analogous to a gravitational interchange mode with the effective gravity arising from the collisional force the neutral flow exerts upon the plasma. The instability will occur when a flow of neutrals is directed opposite to the plasma density gradient. Conceptually, the instability is similar to the well-know

$\mathbf{E} \times \mathbf{B}$ instability [4, 5, 6, 7, 8] which occurs when a perpendicular electric field gives rise to a plasma flow in the presence of a background of immobile neutrals. In the frame of reference moving with the ions $\mathbf{V}_E = \mathbf{E} \times \mathbf{B}c/B^2$, the electric field is zero while the neutrals flow at $-\mathbf{V}_E$. Thus, it would appear at first glance that the two instabilities are identical apart from the factor driving the flow. However, there are two important differences between the $\mathbf{E} \times \mathbf{B}$ instability and the instability considered in this analysis which is driven by a neutral pressure gradient.

1. We consider regimes in which the neutral-ion mean free path λ_{ni} is small in comparison to the macroscopic length scale L. In this regime, the relative velocity between the plasma and the neutrals must be driven by a neutral pressure gradient. This is easily seen from the neutral momentum conservation since the exchange term $MN\nu_{ni}(\mathbf{V}_i - \mathbf{V}_n)$ must be balanced by another finite term in order to justify an equilibrium flow. Balancing the exchange term with viscous dissipation in the neutral fluid can only result in a small relative velocity $(\mathbf{V}_i - \mathbf{V}_n) \sim (\lambda_{ni}/L)^2$. Thus the relative motion between the plasma and the neutral background is small unless there is a neutral pressure gradient and the $\mathbf{E} \times \mathbf{B}$ instability is greatly diminished in this regime. To the best of our knowledge, this regime has not been considered in any previous analysis.

2. All previous researchers have treated the neutral population as an immobile background insensitive to the perturbations in the plasma. While this approximation is well justified for ionospheric plasmas where the plasma density is much less than the neutral density (so that $\lambda_{ni} > L$) , it is not valid in the case of many laboratory and space plasmas. In this analysis, a description of the neutral population is included using fluid equations in the limit of short neutral-ion mean free path $\lambda_{ni}k_y \ll 1$ and with the Boltzmann equation for intermediate $\lambda_{ni}k_y \sim 1$ and long mean free path $\lambda_{ni}k_y \gg 1$.

The regime considered in this analysis is for a magnetically confined partially ionized plasma under conditions which have not been analyzed earlier, where the neutral population is affected by the instability since the neutral density does not

greatly exceed the ion density. This type of regime is relevant to the divertor region of magnetically confined toroidal plasmas. Similar regimes can also occur in weakly magnetized and unmagnetized plasmas such as near the stagnation point of the heliosphere where the interstellar neutrals undergo charge exchange collisions with the ions in the solar wind[9].

Instabilities driven by a relative motion between a plasma and a neutral background are ubiquitous in nature. Linson and Workman [10] appear to be the first to suggest that a mechanism of this type can drive a plasma instability in connection with barium ion clouds released in the ionosphere above the E layer. Theory predicts that the leading edge of an ion cloud drifting through a background of neutrals will be stable while the trailing edge is unstable, in qualitative agreement with observations [10]. An interchange instability of this type was later proposed by researchers studying the equatorial spread F in the ionosphere where the driving factors can include neutral wind, equilibrium electric fields and real gravity [11, 12, 13]. The neutral wind in the F layer of the ionosphere is horizontal in the eastward direction. However, the F layer can often have a significant tilt such that a component of the neutral wind is either parallel (stabilizing) or anti-parallel (destabilizing) to the plasma density gradient [11]. More recently, it has been proposed that similar instabilities might occur in the heliopause near the stagnation point at the "nose" of the heliosphere [9]. In this region, where the solar wind reaches the interstellar medium, the flow of the interstellar ions is diverted around the nose of the heliosphere while the interstellar neutrals flow into the heliosphere and undergo charge exchange collisions with plasma from the solar wind. Thus an equilibrium is set up where the plasma density gradient points outward at the heliopause while a flow of interstellar neutrals is directed inward. Since the neutral and plasma densities are comparable in this region, one might expect the perturbed neutral dynamics to be important. This instability is examined numerically by Liewer, Karmesin and Brackbill [9] in the unmagnetized limit treating both the plasma and neutrals with a fluid description. The growth rate found in these simulations differs significantly from the theoretical values in which the perturbed neutral dynamics are ignored. As one final example, Ershkovich and

Mendis have proposed that instabilities of this nature are important in the sun-ward ionopause of comets [14, 15]. The geometry here is "inside-out" relative to the case of the heliopause. The partially ionized cometary plasma flows outward from the comet into the low density solar wind plasma. The MHD limit of the instability is derived and compared with observations of the comet Halley [15].

In this work, the flute mode stability of a magnetized plasma coupled to a neutral population is examined in plane geometry under the electrostatic approximation. The neutral population is treated first as a collisional fluid and then more generally using the Boltzmann equation with a charge exchange collision operator to determine the neutral response for both short and long neutral-ion mean free path regimes. A fluid description is used for the ions throughout this analysis since we are considering interchange instabilities ($k_{||} = 0$) with small gyro-radius $\rho_i k_y \ll 1$.

The equilibrium considered for this analysis is discussed in Sec. 2.2 and a physical description of the instability is given in Sec. 2.3. A quick heuristic derivation of the dispersion relation including the effect of neutral perturbations is given in Sec. 2.4. Comparisons between the various terms in the ion and neutral fluid equations are made in Sec. 2.5 and a simple dispersion relationship is obtained using the local approximation for short wavelength modes $k_y L \gg 1$. The importance of temperature perturbations on the instability is considered in Sec. 2.6. The neutral response to perturbations in the plasma is calculated from the Boltzmann equation in Sec. 2.7. Based on this result, a local dispersion relation is developed which is valid for arbitrary $k_y \lambda_{ni}$. In Sec. 2.7.2, the collisional limit of this dispersion relation is examined. The long mean free path limit is considered in Sec. 2.7.3 and it is formally shown that the neutral response becomes negligible for large $k_y \lambda_{ni} \gg 1$. The intermediate regime $k_y \lambda_{ni} \sim 1$ is examined numerically in Sec. 2.7.4 for a range of parameters. In Sec. 2.8, two coupled differential equations describing the normal modes of the system are derived using the MHD description for the plasma and fluid equations for the neutrals. For very short wavelength modes, the problem is shown to reduce to the harmonic oscillator equation from quantum mechanics. The realistic conditions for the mode to exist in the presence of finite $k_{||}$ are examined in Sec. 2.9 and the role $\mathbf{E} \times \mathbf{B}$ drifts play

in modifying the instability are discussed in Sec. 2.10. It is pointed out in Sec. 2.11, that the effect of neutral perturbations is quite different for a real gravity than for a neutral pressure gradient. The possible relevance of this instability to the divertor region of a tokamak is considered in Sec. 2.12 and conclusions are summarized in Sec. 2.13.

2.2 Equilibrium

Consider a partially ionized plasma in plane geometry as shown in Fig. 2-1. The ion density n_i and neutral density N vary in the **x** direction and a uniform magnetic field is in the **z** direction. Assuming that the mean free path for a neutral-ion collision is small in comparison to the size of the system and the macroscopic length scale, fluid equations are valid to describe the equilibrium. In this section, an equilibrium appropriate to a two fluid description of the plasma is given.

The equilibrium momentum balance on the ions is

$$0 \approx -\frac{\partial p_i}{\partial x} + \frac{eB}{c} V_{iy} n_i + MN\nu_{ni} \left(V_{nx} - V_{ix}\right) \ , \tag{2.1}$$

$$0 \approx -\frac{eB}{c} V_{ix} n_i + MN\nu_{ni} \left(V_{ny} - V_{iy}\right) \ , \tag{2.2}$$

where $\nu_{ni} = n_i \langle \sigma_x v \rangle$ is the neutral charge exchange frequency, σ_x is the charge exchange cross section, p_i is the ion pressure, $\mathbf{V}_i$ is the ion velocity and $\mathbf{V}_n$ is the neutral velocity. The equilibrium momentum balance on the neutrals is given by

$$0 \approx -\frac{\partial p_n}{\partial x} + MN\nu_{ni} \left(V_{ix} - V_{nx}\right), \tag{2.3}$$

$$0 \approx MN\nu_{ni} \left(V_{iy} - V_{ny}\right) \ , \tag{2.4}$$

where p_n is the neutral pressure. The convective and viscous terms in the neutral momentum equation are neglected since they are of order $(\lambda_{ni}/L)^2$ where $\lambda_{ni} = v_{th}/\nu_{ni}$. For simplicity, it is assumed that the plasma and neutrals are of equal constant tem-

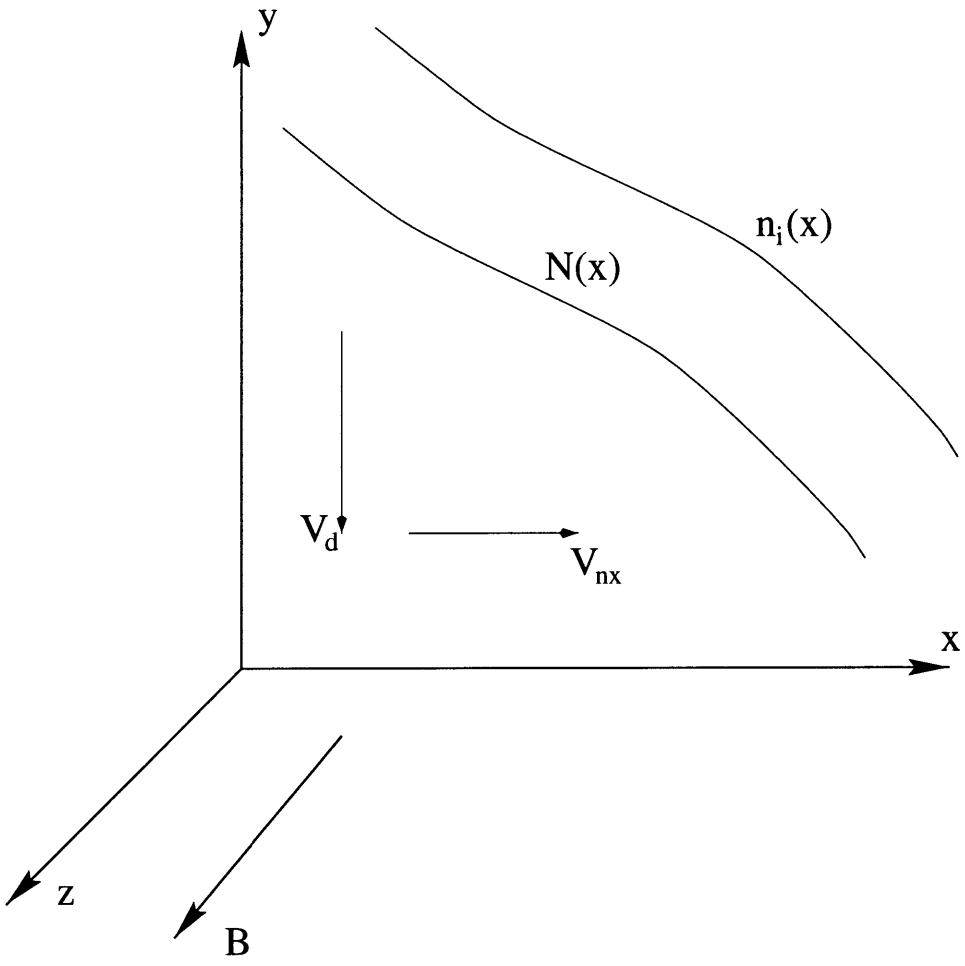

Figure 2-1: Plane geometry considered

perature, $T_i = T_e = T_n = T$. The resulting equilibrium velocities are given by

$$\begin{aligned} V_{ix} &= 0\,, \\ V_{iy} &= V_{ny} = V_d = -\frac{v_{th}^2}{2\Omega_{ci} n_i}\left(\frac{n_i}{L_i} + \frac{N}{L_n}\right)\,, \\ V_{nx} &= \frac{v_{th}^2}{2\nu_{ni} L_n}\,, \end{aligned} \tag{2.5}$$

where

$$\frac{1}{L_n} = -\frac{1}{N}\frac{dN}{dx} \qquad \frac{1}{L_i} = -\frac{1}{n_i}\frac{dn_i}{dx}\,,$$

and $v_{th}^2 = 2T/M$. The equilibrium continuity equation for the neutrals gives the

additional condition

$$\frac{dV_{nx}}{dx} = \frac{V_{nx}}{L_n} \ . \tag{2.6}$$

Neglecting electron-neutral collisions $\nu_{en} \ll \Omega_{ce}$ and electron-ion collisions $\nu_{ei} \ll \Omega_{ce}$, the equilibrium momentum balance on the electrons requires

$$0 \approx -\nabla p_e - e\frac{n_i}{c}\left(\mathbf{V}_e \times \mathbf{B}\right) \ , \tag{2.7}$$

which gives the standard diamagnetic drift for the electrons

$$V_{ey} = -\frac{cT_e}{eBn_i}\frac{dn_i}{dx}. \tag{2.8}$$

2.3 Physical Picture

The equilibrium described in Sec. 2.2 is subject to an interesting instability which in the simplest limit is directly analogous to a gravitational interchange mode. The presence of a neutral pressure within the plasma gives rise to a neutral flow velocity. In equilibrium, the neutral flow velocity is determined by a balance between the neutral pressure and collisional exchange with the ions. The resulting force the neutrals exert on the ions $\mathbf{F} = Mn_i\nu_{in}\mathbf{V}_{nx}$ is in the $\mathbf{x}$ direction and can be thought of as the effective gravity with $g = \nu_{in}V_{nx}$ and $\nu_{in} = N\langle\sigma_x v\rangle$. Consider a perturbation in which a region of higher plasma density is displaced as shown in Fig. 2.3. The effective gravity arising from the neutral flow gives a guiding center drift $\mathbf{V}_d \propto \mathbf{F} \times \mathbf{B}$ in the $\mathbf{y}$ direction for the ions. The resulting charge separation creates an $\mathbf{E} \times \mathbf{B}$ drift in the $\mathbf{x}$ direction that reinforces the initial perturbation. The growth rate of the instability can be calculated quickly under the assumption that the neutrals provide the effective gravity in the equilibrium but are not perturbed by the instability. The growth rate of a collisional interchange instability is of the form [16]

$$\gamma_o = \frac{g}{\nu_{in}L_i} \ . \tag{2.9}$$

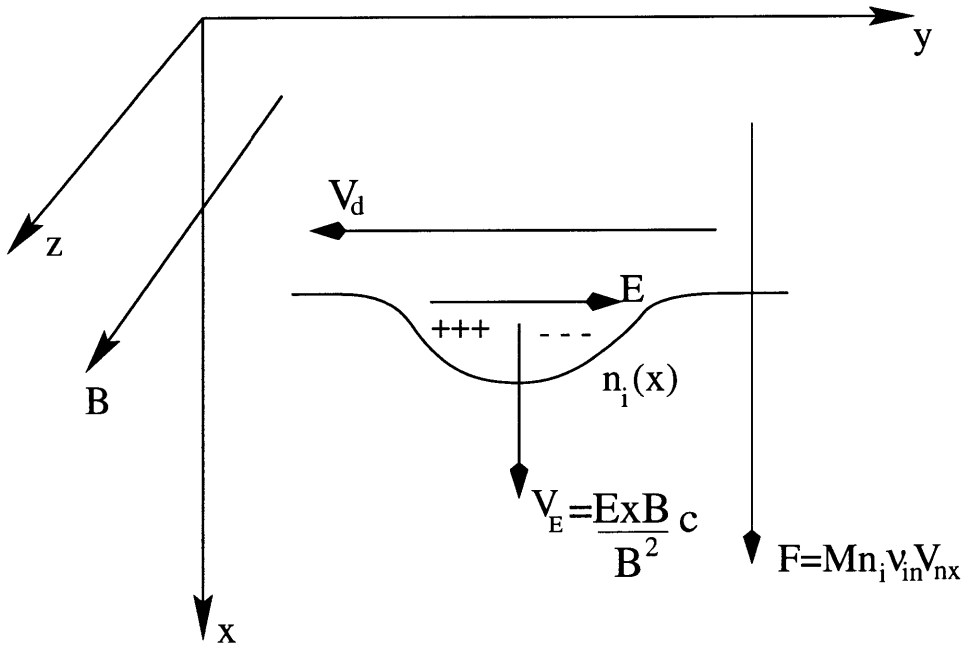

Figure 2-2: Basic mechanism of interchange instability driven by neutral pressure.

Since the effective gravity for this problem is $g = \nu_{in} V_{nx}$, the resulting growth rate is $\gamma_o = V_{nx}/L_i$. Inserting the expression for V_{nx} from Eq. (2.5) this becomes

$$\gamma_o = \frac{v_{th}^2}{2\nu_{ni} L_n L_i} , \tag{2.10}$$

which implies instability for all wavelengths when $L_n L_i > 0$.

This quick calculation assumes that the neutrals provide the effective gravity but are not perturbed by the instability. In Secs. 2.5 and 2.7, it is shown that under certain conditions this is a good approximation and Eq. (2.10) is the resulting growth rate. When the neutrals are perturbed significantly, the analogy with a gravitational interchange mode is no longer clear. Since the effective gravity in this problem is due to a neutral flow, perturbing the neutral population results in a perturbed effective gravity. Such a perturbation might result in dynamics very different than the standard gravitational interchange mode. Although a complete understanding of these regimes remains elusive, the results obtained in this analysis indicate that a primary effect of neutral perturbations is a significant reduction from the idealized growth rate in Eq.

(2.10). In the following section, a simple derivation is given to highlight the physics involved in this important new result.

2.4 Heuristic Derivation of Results

To have a better understanding of the effect of neutral perturbations, it is useful to derive the main result from the basic fluid equations including only the essential elements. In this section, perturbations in the neutral and ion pressures are neglected and we consider short wavelength perturbations $k_y L \gg 1$ of the form

$$\hat{n}_i = \tilde{n}_i exp(\gamma t + i k_y y) \; . \tag{2.11}$$

The dispersion relation may be obtained from the ion and neutral momentum equations along with neutral continuity. To emphasize one of the main physical effects, it is useful to consider the total momentum conservation equation for neutrals and ions

$$n_i \left(\gamma + k_y^2 \mathcal{D}_i\right) \hat{V}_{ix} + N \left(\gamma + k_y^2 \mathcal{D}_N\right) \hat{V}_{nx} \approx 0 \; , \tag{2.12}$$

where $\mathcal{D}_i$ and $\mathcal{D}_N$ are the ion and neutral viscous diffusion coefficients. The ratio of the perturbed neutral velocity to perturbed ion velocity is given by

$$\frac{\hat{V}_{nx}}{\hat{V}_{ix}} \approx -\frac{n_i}{N} \frac{\left(\gamma + k_y^2 \mathcal{D}_i\right)}{\left(\gamma + k_y^2 \mathcal{D}_N\right)} \; . \tag{2.13}$$

From Eq. (2.13), it becomes immediately apparent that that for large neutral densities $N \gg n_i$ the perturbations in the neutral velocity are small. This important conclusion is not as transparent when considering the ion and neutral momentum conservations equations separately

$$\gamma M n_i \hat{V}_{ix} \approx M n_i \nu_{in} \left(\hat{V}_{nx} - \hat{V}_{ix}\right) + M \hat{n}_i \nu_{in} V_{nx} - M n_i \mathcal{D}_i k_y^2 \hat{V}_{ix} \; , \tag{2.14}$$

$$\gamma M N \hat{V}_{nx} \approx M n_i \nu_{in} \left(\hat{V}_{ix} - \hat{V}_{nx}\right) - M \hat{n}_i \nu_{in} V_{nx} - M N \mathcal{D}_N k_y^2 \hat{V}_{nx} \; . \tag{2.15}$$

Next consider neutral momentum conservation. Grouping terms in Eq. (2.15) results in

$$\left(1+\frac{\gamma}{\nu_{ni}}+\lambda_{ni}^2 k_y^2\right)\hat{V}_{nx} \approx \hat{V}_{ix} - V_{nx}\frac{\hat{n}_i}{n_i}\,, \tag{2.16}$$

and in the limit $\gamma \ll \nu_{ni}$ and $\lambda_{ni}k_y \ll 1$ this simplifies to

$$\hat{V}_{nx} \approx \hat{V}_{ix} - V_{nx}\frac{\hat{n}_i}{n_i}\,. \tag{2.17}$$

The ion continuity equation gives

$$\gamma\hat{n}_i + \hat{V}_{ix}\frac{\partial n_i}{\partial x} \approx 0\,, \tag{2.18}$$

which simplifies Eq. (2.17)

$$\hat{V}_{nx} = \hat{V}_{ix}\left(1-\frac{V_{nx}}{\gamma L_i}\right)\,. \tag{2.19}$$

Combining Eq. (2.13) and Eq. (2.19) results in the dispersion relation

$$1-\frac{\gamma_o}{\gamma} \approx -\frac{n_i}{N}\frac{\left(\gamma+k_y^2\mathcal{D}_i\right)}{\left(\gamma+k_y^2\mathcal{D}_N\right)} \approx \frac{\hat{V}_{nx}}{\hat{V}_{ix}}\,, \tag{2.20}$$

where $\gamma_o \equiv V_{nx}/L_i$ is the idealized growth rate discussed in Sec. 2.3. For small wavelength modes $k_y L \gg 1$, the neutral viscosity dominates over inertia $\gamma \ll k_y^2\mathcal{D}_N$ and typically $\gamma \ll k_y^2\mathcal{D}_i$, thus the simplified growth rate is

$$\gamma \approx \gamma_o\frac{N\mathcal{D}_N}{N\mathcal{D}_N + n_i\mathcal{D}_i}\,. \tag{2.21}$$

Clearly in the limit $N\mathcal{D}_N \gg n_i\mathcal{D}_i$, perturbations in the neutral velocity are small and the result $\gamma \approx \gamma_o$ from Sec. 2.3 is recovered. Physically, this is because the neutral viscosity damps out perturbations in the neutral velocity on a time scale faster than mode tends to excite these perturbations.

In the limit of relatively long mean free path $\lambda_{ni}k_y \gtrsim 1$, the fluid neutral momentum conservation equation and the viscous operator are no longer valid. However, the

answer to the problem is already known in the limit $\lambda_{ni}k_y \ll 1$ from the above analysis and in the limit $\lambda_{ni}k_y \gg 1$ since all neutral perturbations must vanish. Thus, there must be some function $\mathcal{G}$ which describes the response for arbitrary $k_y\lambda_{ni}$ and reduces to the know results in the two asymptotic limits. The growth rate of Eq. (2.20) is generalized by replacing the neutral viscosity term with the neutral response function

$$\gamma \approx \gamma_o \frac{\nu_{in}\mathcal{G}}{\nu_{in}\mathcal{G} + k_y^2\mathcal{D}_i} , \tag{2.22}$$

where

$$\mathcal{G}(\nu) \approx \begin{cases} 1 & \text{for } \nu \ll 1 \\ \frac{1}{2\nu^2} = \frac{1}{2}\left(\frac{k_y v_{th}}{\nu_{ni}}\right)^2 & \text{for } \nu \gg 1 \end{cases} , \tag{2.23}$$

and $\nu = \nu_{ni}/(k_y v_{th})$. One possible choice for $\mathcal{G}$ is

$$\mathcal{G}(\nu) = 1 + \mathcal{F}(\nu) , \tag{2.24}$$

where

$$\mathcal{F}(\nu) = -\pi^{1/2}\nu \, exp(\nu^2)\left[1 - erf(\nu)\right] , \tag{2.25}$$

and $erf(\nu)$ is the well-know error function. Furthermore, this choice for $\mathcal{F}(\nu)$ reduces to the result obtained from the solution to the Boltzmann equation in the limit $|\omega| \ll \nu_{ni}$ where ω includes the real and imaginary part of the frequency (see page 39).

Apart from the Doppler shifts, the results in this section are identical to Eq. (2.108) which results from a much longer derivation. For the case $k_y\lambda_{ni} \gg 1$, the neutral velocity perturbations are negligible and the function $\mathcal{G} \to 1$. In this limit, the result is consistent with a previous analysis of gravitational interchange modes including ion-ion collisions [17].

This simple derivation also brings to light a prescription for adding in the effect of neutral velocity perturbations: One can simply replace $\nu_{in} \to \nu_{in}\mathcal{G}$. The resulting dispersion relation will include the correct neutral response for both short and long mean free path regimes. This simple prescription is rigorously justified in the analysis of Sec. 2.7.

2.5 Fluid Treatment

If the mean free path $\lambda_{ni} = v_{th}/\nu_{ni}$ is small in comparison to the wavelength of the perturbation, then fluid equations are a valid description for both the plasma and neutral dynamics. The transport coefficients and fluid equations for a partially ionized plasma which have been derived in several recent papers [18, 19] are used in this analysis. In addition, the ion and neutral densities are assumed to be of the same order in this section so that $\lambda_{ni} \sim \lambda_{in} = v_{th}/\nu_{in}$. In Sec. 2.7.1, this ordering is relaxed to allow for arbitrary plasma and neutral densities.

Consider electrostatic perturbations of the form

$$\hat{\phi} = \tilde{\phi}\, exp(-i\omega t + ik_y y) \;, \tag{2.26}$$

where $\hat{\mathbf{E}} = -\nabla\hat{\phi}$. The perturbed fluid variables are of the same form with a circumflex signifying a perturbed Fourier component and a tilde denoting the amplitude of the component. A dispersion relationship is obtained by combining the dynamics of the electrons, ions and neutrals together with the quasineutrality condition.

The electron response for $k_{||} = 0$ is determined from the perturbed electron continuity equation

$$\frac{\partial \hat{n}_e}{\partial t} + \nabla \cdot \left(n_e \hat{\mathbf{V}}_E\right) = 0 \;, \tag{2.27}$$

where $\hat{\mathbf{V}}_E = (\hat{\mathbf{E}} \times \mathbf{B})c/B^2$. The electron response from Eq. (2.27) is

$$\frac{\hat{n}_e}{n_e} = \frac{\omega_{*e}}{\omega}\frac{e\hat{\phi}}{T_e} \;, \tag{2.28}$$

where $\omega_{*e} = k_y c T_e/(eBL_i)$.

Since the ion and neutral dynamics are coupled through charge exchange, it is convenient to examine these together. It is less cumbersome to work with the full nonlinear equations while making some initial simplifications. For simplicity, it is assumed that charge exchange is the dominant collisional process and ionization and recombination are neglected. It is assumed that there is a single ion species along

with a neutral population of the same mass. Consider the ion and neutral momentum equations

$$Mn_i\frac{d\mathbf{V}_i}{dt} = -\nabla p_i + en_i\left(\mathbf{E} + \frac{\mathbf{V}_i \times \mathbf{B}}{c}\right) + MN\nu_{ni}(\mathbf{V}_n - \mathbf{V}_i) - \nabla\cdot\mathbf{\Pi}_i\ , \tag{2.29}$$

$$MN\frac{d\mathbf{V}_n}{dt} = -\nabla p_n + MN\nu_{ni}(\mathbf{V}_i - \mathbf{V}_n) - \nabla\cdot\mathbf{\Pi}_n, \tag{2.30}$$

where $\mathbf{\Pi}_i$ is the ion viscous stress tensor [20] and $\mathbf{\Pi}_n$ is a neutral viscous stress tensor due to charge exchange collisions [19]

$$\mathbf{\Pi}_n = -\frac{p_n}{\nu_{ni}}\left(\nabla\mathbf{V}_n + \nabla\mathbf{V}_n^T - \frac{2}{3}I\nabla\cdot\mathbf{V}_n\right)\ . \tag{2.31}$$

It is convenient to add (2.29) and (2.30) to eliminate the exchange term and work with the sum equation

$$M\left(n_i\frac{d\mathbf{V}_i}{dt} + N\frac{d\mathbf{V}_n}{dt}\right) = -\nabla\left(p_i + p_n\right) + en_i\left(\mathbf{E} + \frac{\mathbf{V}_i \times \mathbf{B}}{c}\right) - \nabla\cdot(\mathbf{\Pi}_n + \mathbf{\Pi}_i)\ . \tag{2.32}$$

Since to lowest order both the ions and the electrons drift with the $\mathbf{E}\times\mathbf{B}$ velocity, the charge separation for the instability comes from corrections to the $\mathbf{E}\times\mathbf{B}$ velocity of the ions. This correction is calculated by taking the cross product of (2.32) with $\mathbf{B}$ and solving for $\mathbf{V}_i$

$$n_i\mathbf{V}_i = n_ic\frac{\mathbf{E}\times\mathbf{B}}{B^2} - \frac{1}{\Omega_{ci}}\left[\left(n_i\frac{d\mathbf{V}_i}{dt} + N\frac{d\mathbf{V}_n}{dt}\right) + \frac{\nabla\left(p_i + p_n\right)}{M} + \frac{\nabla\cdot(\mathbf{\Pi}_n + \mathbf{\Pi}_i)}{M}\right]\times\mathbf{b}\ , \tag{2.33}$$

where $\mathbf{b} = \mathbf{B}/|B|$. Taking the divergence of this gives

$$\nabla\cdot(n_i\mathbf{V}_i) = \mathbf{V}_E\cdot\nabla n_i - \nabla\cdot\left[\frac{(\nabla\cdot(\mathbf{\Pi}_n + \mathbf{\Pi}_i))\times\mathbf{b}}{M\Omega_{ci}}\right] + \frac{1}{\Omega_{ci}}\nabla\cdot\left[\left(n_i\frac{d\mathbf{V}_i}{dt} + N\frac{d\mathbf{V}_n}{dt}\right)\times\mathbf{b}\right]\ , \tag{2.34}$$

which is still valid nonlinearly. Notice that Eq. (2.33) contains a diamagnetic type term involving both the ion and neutral pressures, but upon taking the divergence this term vanishes. Physically, this is because the diamagnetic drift is a fluid drift,

not a drift of the guiding centers, thus it can not give rise to a charge separation.

The dispersion relation is obtained from quasineutrality in the form $\partial\hat{n}_i/\partial t \approx \partial\hat{n}_e/\partial t$. Using this along with ion and electron continuity gives

$$\nabla\cdot\left(\hat{n}_i\mathbf{V}_i + n_i\hat{\mathbf{V}}_i\right) \approx \nabla\cdot\left(n_e\hat{\mathbf{V}}_E\right) \ . \tag{2.35}$$

Now perturbing Eq. (2.34) and substituting into Eq. (2.35) results in terms involving $\hat{\mathbf{V}}_E$ on both sides which cancel. This simplifies Eq. (2.35) to

$$0 \approx \nabla\cdot\left[\left(\nabla\cdot\left(\hat{\mathbf{\Pi}}_i + \hat{\mathbf{\Pi}}_n\right)\right)\times\mathbf{b}\right] + M\nabla\cdot\left[\left(n_i\frac{d\hat{\mathbf{V}}_i}{dt} + N\widehat{\frac{d\mathbf{V}_n}{dt}}\right)\times\mathbf{b}\right] \ , \tag{2.36}$$

where the large circumflex indicates that the entire term is perturbed.

Up to this point, no approximations have been made to the neutral or ion momentum equations except neglecting ionization and recombination. Now consider an ordering where

$$\begin{aligned} &\omega \ll \tfrac{v_{th}^2k_y^2}{\nu_{ni}} \ll \nu_{ni} \ll \Omega_{ci} \ , \qquad && \nu_{ii} \ll \Omega_{ci} \ , \\ &\rho_i \ll \lambda_{ni} \ll \tfrac{1}{k_y} \ll L \ , && L_n \sim L_i \sim L \ , \qquad N \sim n_i \ . \end{aligned} \tag{2.37}$$

Under this ordering it can be shown that neutral viscosity in Eq. (2.36) is the dominant term. Comparing neutral viscosity to ion viscosity yields

$$\frac{\left(\nabla\cdot\hat{\mathbf{\Pi}}_i\right)_\perp}{\left(\nabla\cdot\hat{\mathbf{\Pi}}_n\right)_\perp} \sim \frac{n_i}{N}\frac{\nu_{ii}\nu_{ni}}{\Omega_{ci}^2} \ll 1 \ . \tag{2.38}$$

Note that the ratio in Eq. (2.38) is proportional to n_i^3 and for high density plasmas this ordering is not always satisfied. In Sec. 2.7.1, this ordering is relaxed to allow contributions from this term. Comparing neutral viscosity to the neutral part of the inertial term in Eq. (2.36) gives terms of order

$$\frac{M\widehat{N\frac{d\mathbf{V}_n}{dt}}}{\left(\nabla\cdot\hat{\mathbf{\Pi}}_n\right)_\perp} \sim \frac{\omega\nu_{ni}}{k_y^2v_{th}^2} \ll 1 \ . \tag{2.39}$$

Now consider the neutral momentum equation (2.30) with the ordering of Eq. (2.37) and neglecting temperature perturbations. To lowest order in ω/ν_{ni} and $k_y\lambda_{ni}$, the perturbed neutral velocity is

$$\hat{\mathbf{V}}_n = \hat{\mathbf{V}}_i - \frac{v_{th}^2 \nabla \hat{N}}{2N\nu_{ni}} + \frac{v_{th}^2}{2N\nu_{ni}} \left[\frac{\hat{N}}{N} + \frac{\hat{n}_i}{n_i} \right] \nabla N \, . \tag{2.40}$$

Neglecting ionization and recombination the neutral continuity equation is

$$\frac{\partial \hat{N}}{\partial t} + \nabla \cdot \left(\hat{N}\mathbf{V}_n + N\hat{\mathbf{V}}_n \right) = 0 \, . \tag{2.41}$$

Substituting Eq. (2.40) into the neutral continuity equation and keeping the $\hat{\mathbf{E}} \times \mathbf{B}$ and diamagnetic drifts for the ions gives

$$\frac{\hat{N}}{N} \left[\omega - \omega_{di} \left(1 + \frac{N}{n_i} \right) + i \frac{k_y^2 v_{th}^2}{2\nu_{ni}} \right] + \frac{L_i}{L_n} \omega_{di} \frac{e\hat{\phi}}{T_i} + \frac{\hat{n}_i}{n_i} \left[\frac{L_i}{L_n} \omega_{di} \left(1 + \frac{N}{n_i} \right) - i \frac{v_{th}^2}{2\nu_{ni} L_n L_i} \right] = 0 \, , \tag{2.42}$$

where $\omega_{di} = -k_y cT/(eBL_i)$. In contrast with ion continuity, the terms originating from the diamagnetic drift do not vanish for neutral continuity. The dominant term in the neutral continuity equation is the diffusive term involving $k_y^2 v_{th}^2/\nu_{ni}$. Comparing it to the other terms in Eq. (2.42) it is clear the ratio of neutral density perturbation to ion density perturbation involves parameters which are small

$$\frac{\hat{N}/N}{\hat{n}_i/n_i} \sim \left[\frac{\omega\nu_{ni}}{k_y^2 v_{th}^2} \, , \; \frac{\nu_{ni}}{\Omega_{ci}} \frac{1}{k_y L} \, , \; \frac{1}{k_y^2 L^2} \right] \ll 1 \, . \tag{2.43}$$

Under the ordering considered in Eq. (2.37) it is difficult to perturb the neutral density to the same degree as the ion density since the ions are constrained in the perpendicular direction by the magnetic field while the neutrals are not. A perturbed neutral pressure across the field gives rise to a perturbed neutral velocity which tends to flatten the pressure perturbation on a time scale $\nu_{ni}/(k_y^2 v_{th}^2)$. Likewise neutral viscosity tends to flatten perturbations in the neutral velocity on this same time scale. If this time scale is small in comparison to the relevant time scale of the mode, then neutral perturbations will not play a significant role. Using Eq. (2.40) to compare the

ion inertial term to the neutral viscosity in Eq. (2.36), one can show that ion inertia is also small. Therefore, the leading order term of Eq. (2.36) is

$$0 \approx \nabla \cdot \left[\left(\nabla \cdot \hat{\mathbf{\Pi}}_n \right) \times \mathbf{b} \right] . \tag{2.44}$$

As shown in Eq. (2.31) the general expression for the viscous stress tensor $\mathbf{\Pi}_n$ is nontrivial, but for $k_y L \gg 1$ the leading order result is rather simple. Assuming $\partial/\partial x \sim 1/L$ and $k_y L \gg 1$, the divergence of the stress tensor simplifies to

$$\nabla \cdot \hat{\mathbf{\Pi}}_n \approx \frac{\rho_n v_{th}^2}{2\nu_{ni}} \left[\nabla^2 \hat{\mathbf{V}}_n + \frac{1}{3} \nabla \left(\nabla \cdot \hat{\mathbf{V}}_n \right) \right] \approx -\frac{\rho_n v_{th}^2}{2\nu_{ni}} \left[k_y^2 \hat{\mathbf{V}}_n + \frac{k_y^2}{3} \hat{V}_{ny} \mathbf{e}_y \right] . \tag{2.45}$$

Substituting Eq. (2.45) into Eq. (2.44) results in

$$\nabla \cdot \left[\left(\nabla \cdot \hat{\mathbf{\Pi}}_n \right) \times \mathbf{b} \right] \approx i k_y \left(\frac{\rho_n v_{th}^2}{2\nu_{ni}} k_y^2 \hat{V}_{nx} \right) - \frac{4}{3} \frac{\partial}{\partial x} \left(\frac{\rho_n v_{th}^2}{2\nu_{ni}} k_y^2 \hat{V}_{ny} \right) \approx 0 \tag{2.46}$$

It is clear from the lowest order solution to Eq. (2.33) that $\hat{V}_{ix}/\hat{V}_{iy} \sim k_y L$ and from Eq. (2.40) it follows that $\hat{V}_{nx}/\hat{V}_{ny} \sim k_y L$. Thus for $k_y L \gg 1$ the leading order term of Eq. (2.46) is

$$\hat{V}_{nx} \approx 0 . \tag{2.47}$$

Using Eq. (2.47) in Eq. (2.40) gives

$$\hat{V}_{ix} - \frac{v_{th}^2}{2\nu_{ni} L_n} \left[\frac{\hat{N}}{N} + \frac{\hat{n}_i}{n} \right] \approx 0 . \tag{2.48}$$

The lowest order result for $\hat{V}_{ix}$ is obtained by dropping the inertia terms in Eq. (2.33) which are small by a factor ω/Ω_{ci} and dropping the ion and neutral viscosity terms which are small by factors $(\rho_i k_y)^2 \nu_{ii}/\Omega_{ci}$ and $(\lambda_{ni} k_y)^2 \nu_{ni}/\Omega_{ci}$. Thus the lowest order solution for $\hat{V}_{ix}$ in Eq. (2.33) includes the $\hat{\mathbf{E}} \times \mathbf{B}$ drift and a diamagnetic type term

$$\hat{V}_{ix} = \frac{-i k_y c \hat{\phi}}{B} - i \frac{k_y v_{th}^2}{2\Omega_{ci}} \left(\frac{\hat{n}_i}{n_i} + \frac{\hat{N}}{n_i} \right) . \tag{2.49}$$

Combining Eq. (2.48) and (2.49) and neglecting the neutral density perturbations

gives the dispersion relation

$$\omega \approx \omega_{di} + i\frac{v_{th}^2}{2\nu_{ni}L_nL_i} , \tag{2.50}$$

in agreement with the physical picture in Sec. 2.3. All wavelengths are unstable as long as $L_nL_i > 0$. For the dispersion relation of Eq. (2.50), the neutrals enter only into the equilibrium by providing an effective gravity and are not perturbed significantly. As a consistency check for the ordering $\omega \ll k_y^2 v_{th}^2/\nu_{ni}$, the real and imaginary parts of Eq. (2.50) imply

$$\frac{\nu_{ni}}{\Omega_{ci}} \ll k_y L_n , \qquad L_nL_ik_y^2 \gg 1 . \tag{2.51}$$

Under the rigid ordering of Eq. (2.37) perturbations in the neutral population are weak. In Sec. 2.7.1, a relaxed ordering allowing $\nu_{ii} \sim \Omega_{ci}$ and arbitrary plasma and neutral densities is considered. The resulting dispersion relation in these regimes is considerably different with perturbations in the neutral velocity playing an important role. Even without the effect of ion viscosity, neutral perturbations play a crucial role when considering realistic $k_{||}$ and the coupling the shear Alfvén mode (see Sec. 2.9).

Long wavelength modes are of particular importance since they potentially have the greatest effect in altering the equilibrium. However, when the wavelength of the perturbation become comparable to the density length scale, the ordering breaks down and the simple dispersion relation (2.50) is not valid. A complete analytic treatment in the limit $k_yL \sim 1$ is not tractable because perturbations in the densities, velocities and temperatures of both the ions and neutrals as well as non-local effects must be retained. A normal mode analysis is presented in Sec. 2.8 resulting in the eigenfunctions for the very short wavelength modes.

2.6 Temperature Perturbations

In the fluid treatment of Sec. 2.5, temperature perturbations of the plasma and neutral population were neglected. In this section, this approximation is justified by carefully examining the various terms in the ion and neutral energy conservation equations. The ion thermal conductivity as calculated from collisional theory is usually small since the ion gyro-radius is assumed to be much less than the perpendicular wavelength. However, the mean free path for a neutral-ion collision may be much larger than a gyro-radius and the thermal conductivity for the neutrals may be considerable. The general ordering assumed in this analysis is that $\omega \ll k_y^2 v_{th}^2/\nu_{ni}$ which implies that the thermal conductivity of the neutrals can smooth out temperature perturbations faster than the growth time of the mode. Since the basic growth rate of the mode is $\gamma \approx v_{th}^2/(\nu_{ni} L_i L_n)$, this condition is well satisfied as long as $k_y L \gg 1$. In addition, the large ion-neutral collision frequency $\omega \ll \nu_{in}$ ensures that the ion and neutral temperature perturbations are nearly equal $\hat{T}_i \approx \hat{T}_n$. Thus even in situations where the ion thermal conductivity is weak, the neutral thermal conductivity can smooth out perturbations in both the ion and the neutral temperatures. It is important to note that perturbations in the neutral density are also smeared out on the same time scale as the temperature perturbations. While the energy equations have an exchange term $\nu_{in}(\hat{T}_n - \hat{T}_i)$ which tightly couples the perturbed ion and neutral temperatures, there is no such term in the continuity equations and the ion density may be perturbed rather independently of the neutral density.

In an effort to more carefully examine the above conclusions, consider the ion energy equation

$$\frac{3}{2} n_i \frac{dT_i}{dt} + p_i \nabla \cdot \mathbf{V}_i = -\nabla \cdot \mathbf{q}_i + \frac{3}{2} n_i \nu_{in} (T_n - T_i) \ , \tag{2.52}$$

along with the neutral energy equation

$$\frac{3}{2} N \frac{dT_n}{dt} + p_n \nabla \cdot \mathbf{V}_n = -\nabla \cdot \mathbf{q}_n + \frac{3}{2} N \nu_{ni} (T_i - T_n) \ , \tag{2.53}$$

where ionization, recombination and electron collisions are neglected. Adding these equations to eliminate the exchange term gives

$$\frac{3}{2}\left(n_i\frac{dT_i}{dt}+N\frac{dT_n}{dt}\right)+p_i\nabla\cdot\mathbf{V}_i+p_n\nabla\cdot\mathbf{V}_n=-\nabla\cdot(\mathbf{q}_i+\mathbf{q}_n)\ . \tag{2.54}$$

To estimate the importance of temperature perturbations take a simplified form for the diffusive heat fluxes

$$\nabla\cdot\hat{\mathbf{q}}_n\approx-N\frac{v_{th}^2}{\nu_{ni}}\nabla^2\hat{T}_n\ ,\qquad \nabla\cdot\hat{\mathbf{q}}_i\approx-n_i\rho_i^2\nu_{ii}\nabla^2\hat{T}_i\ . \tag{2.55}$$

Consider first the perturbed ion energy equation for the ordering in Eq. (2.37). Although the ion thermal conductivity is small for this ordering, it may become significant in high density regimes. Since the collision frequency ν_{in} is large, there is a tendency for the perturbed ion temperature to follow the perturbed neutral temperature. The perturbed ion energy equation is

$$\frac{3}{2}n_i\left(-i\omega+ik_yV_d\right)\hat{T}_i+p_i\nabla\cdot\hat{\mathbf{V}}_i\approx-n_i(\rho_ik_y)^2\nu_{ii}\hat{T}_i+\frac{3}{2}n_i\nu_{in}\left(\hat{T}_n-\hat{T}_i\right). \tag{2.56}$$

Taking the lowest order solution for $\hat{\mathbf{V}}_i$ from Eq. (2.33) to calculate the divergence of $\hat{V}_i$ gives terms of order $\nabla\cdot\hat{V}_i\sim\omega_{di}(\hat{n}_i/n_i)$. For the ordering $\omega\ll\nu_{in}$ with $\omega_{di}\ll\nu_{in}$ and $(\rho_ik_y)^2\nu_{ii}\ll\nu_{in}$, the ion energy equation implies $\hat{T}_i\approx\hat{T}_n$.

Next consider the sum energy equation for the ordering considered in Eq. (2.37). The dominant terms are the ion and neutral compression terms and the neutral thermal conductivity

$$p_i\nabla\cdot\hat{\mathbf{V}}_i+p_n\nabla\cdot\hat{\mathbf{V}}_n\approx N\frac{v_{th}^2}{\nu_{ni}}\nabla^2\hat{T}_n\ . \tag{2.57}$$

Using neutral momentum to evaluate $\hat{\mathbf{V}}_n$ in the limit of Eq. (2.37) gives

$$\hat{\mathbf{V}}_n=\hat{\mathbf{V}}_i-\frac{\nabla\hat{p}_n}{2MN\nu_{ni}}+\frac{v_{th}^2}{2N\nu_{ni}}\left[\frac{\hat{N}}{N}+\frac{\hat{n}_i}{n}-\frac{\hat{T}_n}{T}\right]\nabla N\ . \tag{2.58}$$

Simplifying Eq. (2.57) and dropping terms consistent with Eq. (2.37) gives

$$\frac{\hat{T}_n}{T} \approx -\frac{1}{2}\frac{\hat{N}}{N} + \frac{\hat{n}_i}{2n_i}\left[\frac{1}{k_y^2 L_n^2}\left(1+\frac{L_n}{L_i}\right) + \left(1+\frac{N}{n_i}\right)\frac{\nu_{ni}}{\Omega_{ci}}\frac{1}{k_y L_n}\right] . \tag{2.59}$$

Examining Eq. (2.59), it is clear that neutral temperature perturbations are of the same order as neutral density perturbations $\hat{T}_n/T \sim \hat{N}/N$. Using $\hat{T}_i \approx \hat{T}_n$ along with the previous result from neutral continuity (see Eq. (2.42)), it is easy to show that the ratio of ion temperature perturbations to ion density perturbations is small

$$\frac{\hat{T}_i/T}{\hat{n}_i/n_i} \sim \left[\frac{\nu_{ni}}{\Omega_{ci}}\frac{1}{k_y L} \;,\; \frac{1}{k_y^2 L^2}\right] \ll 1 . \tag{2.60}$$

Therefore, it is appropriate to neglect ion temperature perturbations in the analysis. On the other hand, perturbations in the neutral density and temperature are of equal importance. Neutral temperature perturbations enter through the pressure term in the neutral momentum equation and to a lesser extent in the neutral viscosity. Since neutral density perturbations were in the end neglected to derive the dispersion relation in Eq. (2.50), it is appropriate to neglect the neutral temperature perturbations as well. For long wavelength modes $k_y L \sim 1$, both neutral and ion temperature perturbations are important.

To summarize, ion and neutral temperature perturbations as well as neutral density perturbations are all negligible for $k_y L \gg 1$. For the analytic results obtained in this thesis, the effect of neutral velocity perturbations are of importance while perturbations in the neutral density and temperature are neglected.

2.7 Kinetic Treatment

When the mean free path is comparable to the wavelength of the perturbation, fluid equations are no longer valid to describe the neutral response. In this section, the response of the neutrals is calculated using the Boltzmann equation. Since λ_{ni} is assumed to be small in comparison to the unperturbed macroscopic length scales, a fluid description is still valid to describe the equilibrium.

The Boltzmann equation for the neutrals is

$$\frac{\partial g}{\partial t} + \mathbf{v} \cdot \nabla g = \int d^3\mathrm{v}' \sigma_x |\mathbf{v}' - \mathbf{v}| \left[f(\mathbf{v}) g(\mathbf{v}') - f(\mathbf{v}') g(\mathbf{v}) \right] , \tag{2.61}$$

where g is the distribution function for the neutrals, f is the distribution function for the ions and σ_x is the charge exchange cross section. The slow velocity space dependence of $\sigma_x|\mathbf{v}' - \mathbf{v}|$ in the Boltzmann collision operator is ignored by defining

$$\sigma_x |\mathbf{v}' - \mathbf{v}| = \frac{\nu_{ni}}{n_i} , \tag{2.62}$$

with the collision frequency ν_{ni} assumed independent of velocity. This is a good approximation in the energy range 0.1 - 10 eV and has been used by other researchers [18] in deriving transport coefficients in partially ionized plasmas. The collision operator then simplifies to an algebraic expression to give

$$\frac{\partial g}{\partial t} + \mathbf{v} \cdot \nabla g = \frac{\nu_{ni}}{n_i} \left(f N - n_i g \right) . \tag{2.63}$$

The perturbed form of (2.63) is

$$\frac{\partial \hat{g}}{\partial t} + \mathbf{v} \cdot \nabla \hat{g} + \hat{g} \nu_{ni} = \frac{\nu_{ni}}{n_i} \left(\hat{f} N + \hat{N} f - \hat{n}_i g \right) . \tag{2.64}$$

Equation (2.64) can be written in terms of a total derivative along the characteristics to obtain

$$\frac{d}{dt} \left(e^b \hat{g} \right) = e^b \hat{R} , \tag{2.65}$$

where

$$b(x) = \frac{1}{\mathrm{v}_x} \int \nu_{ni}(x) dx , \tag{2.66}$$

$$\hat{R} = \frac{\nu_{ni}}{n_i} \left(\hat{f} N + \hat{N} f - g \hat{n}_i \right) . \tag{2.67}$$

Equation (2.65) is then solved by integrating along a characteristic curve defined by

$$\frac{d\mathbf{v}}{dt} = 0 \qquad \frac{d\mathbf{x}}{dt} = \mathbf{v} ,$$

which gives

$$\begin{aligned} x' - x &= \mathrm{v}_x \tau, \\ y' - y &= \mathrm{v}_y \tau, \\ t' - t &= \tau. \end{aligned} \tag{2.68}$$

Integrating from the remote past, the initial condition may be neglected for $Im(\omega) > 0$ to find

$$e^{b(x)} \hat{g}(x, \mathbf{v}) = \int_{-\infty}^{t} e^{b(x'(t'))} \hat{R}(x'(t')) dt' \ . \tag{2.69}$$

Assuming perturbations of the form

$$\begin{aligned} \hat{R} &= \tilde{R}(x'(t')) exp(-i\omega t' + ik_y y') \ , \\ \hat{g} &= \tilde{g}(x) exp(-i\omega t + ik_y y) \ , \end{aligned} \tag{2.70}$$

Eq. (2.69) can be written as

$$\tilde{g} = \int_{-\infty}^{0} \tilde{R}(x'(\tau)) exp(-i\omega\tau + ik_y \mathrm{v}_y \tau + b(x'(\tau)) - b(x)) d\tau \ . \tag{2.71}$$

Equation (2.71) is the general non-local solution for the perturbed neutral response. Unfortunately, it is difficult to work with even if the functional form for the equilibrium is simple. However, a series approximation to this integral solution is easily obtained by repeatedly integrating by parts. Notice that from Eq. (2.66)

$$\frac{d}{d\tau} b(x'(\tau)) = \mathrm{v}_x \frac{d}{dx'} b(x'(\tau)) = \nu_{ni} \ , \tag{2.72}$$

so that integrating Eq. (2.71) by parts gives

$$\tilde{g} = \frac{i\tilde{R}}{\overline{\omega}} + \int_{-\infty}^{0} \mathrm{v}_x exp[-i\omega\tau + ik_y \mathrm{v}_y \tau + b(x'(\tau)) - b(x)] \frac{d}{dx} \left[\frac{\tilde{R}(x'(t'))}{i\overline{\omega}} \right] d\tau \ , \tag{2.73}$$

where $\overline{\omega} = \omega - k_y \mathrm{v}_y + i\nu_{ni}$. Likewise the second term in (2.73) is integrated by parts to obtain the next order term in the series. The end result of these integrations is

the asymptotic expansion

$$\tilde{g} = \left[1 - \mathcal{L} + \mathcal{L}^2 - \mathcal{L}^3 + ...\right] \frac{i\tilde{R}}{\overline{\omega}} = \sum_{j=0}^{\infty} (-1)^j \mathcal{L}^j \frac{i\tilde{R}}{\overline{\omega}} \ , \tag{2.74}$$

where

$$\mathcal{L} = \frac{i\mathrm{v}_x}{\overline{\omega}} \frac{d}{dx}.$$

Upon integrating Eq. (2.74) over velocity space it is easy to show that this is really an expansion in λ_{ni}/L where λ_{ni} is a mean free path and L is an equilibrium scale length. For fluid equations to be valid for the equilibrium, it must be assumed that λ_{ni}/L is a small parameter. Therefore, the series is valid regardless of whether the wavelength is short or long in comparison to a mean free path.

Truncating the series (2.74) to first order in $\mathcal{L}$ and integrating over velocity space gives the perturbed neutral density

$$\tilde{N} = \int d^3\mathrm{v}\tilde{g} \approx \int d^3\mathrm{v} \left(1 - \frac{i\mathrm{v}_x}{\overline{\omega}} \frac{d}{dx}\right) \frac{i\nu_{ni}}{n_i \overline{\omega}} \left(\tilde{f}N + \tilde{N}f - g\tilde{n}_i\right) \ . \tag{2.75}$$

To complete this calculation, it is assumed that the unperturbed distribution functions f and g are Maxwellians

$$f = \frac{n_i}{\pi^{3/2} v_{th}^3} exp\left[-\frac{\mathrm{v}_x^2 + (\mathrm{v}_y - \mathrm{V}_d)^2 + \mathrm{v}_z^2}{v_{th}^2}\right] \ , \tag{2.76}$$

$$g = \frac{N}{\pi^{3/2} v_{th}^3} exp\left[-\frac{(\mathrm{v}_x - V_{nx})^2 + (\mathrm{v}_y - \mathrm{V}_d)^2 + \mathrm{v}_z^2}{v_{th}^2}\right] \ , \tag{2.77}$$

where V_d and V_{nx} are given by the fluid equilibrium in Eq. (2.5). Assuming a collisional treatment remains valid for the ions, the perturbed ion distributions function $\tilde{f}$ may be taken to be a linearized Maxwellian

$$\tilde{f} = f\left\{\frac{\tilde{n}_i}{n_i} + \frac{2}{v_{th}^2}\left[\tilde{V}_{ix}\mathrm{v}_x + \tilde{V}_{iy}(\mathrm{v}_y - V_d)\right]\right\} \ . \tag{2.78}$$

Substituting the preceding into (2.75) and simplifying gives

$$\frac{\tilde{N}}{N}(1+Z_1) = -2\frac{\tilde{V}_{iy}}{v_{th}}W_1 - i\lambda_{ni}Z_2\left[\frac{1}{Nn_i}\frac{d}{dx}(Nn_i\frac{\tilde{V}_{ix}}{v_{th}}) - \frac{V_{nx}}{v_{th}}\frac{1}{n_i}\frac{d\tilde{n}_i}{dx}\right] + \frac{\lambda_{ni}}{L_i}Z_3\left[\frac{\tilde{V}_{ix}}{v_{th}} - \frac{V_{nx}}{v_{th}}\frac{\tilde{n}_i}{n_i}\right], \tag{2.79}$$

where

$$Z_m = i\frac{\nu^m}{\pi^{1/2}}\int_{-\infty}^{\infty}\frac{e^{-\xi^2}}{(\xi-\Lambda-i\nu)^m}d\xi\,, \tag{2.80}$$

$$W_m = i\frac{\nu^m}{\pi^{1/2}}\int_{-\infty}^{\infty}\frac{\xi e^{-\xi^2}}{(\xi-\Lambda-i\nu)^m}d\xi = \nu Z_{m-1} + (\Lambda+i\nu)Z_m\,, \tag{2.81}$$

$$\nu = \frac{\nu_{ni}}{k_y v_{th}} \qquad \Lambda = \frac{\omega - k_y V_d}{k_y v_{th}}\,. \tag{2.82}$$

Notice that for a purely imaginary argument, the Z_1 function reduces to

$$Z_1(i\zeta_i) = -\pi^{1/2}\zeta_i\, exp[\zeta_i^2]\,[1 - erf(\zeta_i)]\,, \tag{2.83}$$

where $\zeta_i = Im(\zeta)$, $\zeta = \Lambda + i\nu$ and $erf(\zeta)$ is the well-know error function. Although the real frequency of this instability may be comparable to the growth rate, we are usually interested in regimes where $|\Lambda| \ll \nu$ so that the argument is mostly imaginary $\zeta \approx \zeta_i \approx \nu$ and Eq. (2.83) is a good approximation to Z_1. In this limit, the Z_1 function reduces to the function $\mathcal{F}$ introduced in Sec. (2.4).

The first term on right hand side of Eq. (2.79) is from the lowest order term in Eq. (2.74) while the next two terms are from the first order term in the series. In this form, it is clear that the series solution represents an expansion in λ_{ni}/L.

The perturbed neutral velocity is calculated from the first moment of Eq. (2.74) and the **y** component is given by

$$\tilde{N}V_{ny} + N\tilde{V}_{ny} = \int \mathrm{v}_y\tilde{g}d^3\mathrm{v}\,. \tag{2.84}$$

Truncating Eq. (2.74) to first order in $\mathcal{L}$ gives

$$\tilde{V}_{ny} = -W_1\left[2\tilde{V}_{iy}(\Lambda + i\nu) + \frac{\tilde{N}}{N}v_{th}\right] - i\lambda_{ni}W_2\left[\frac{1}{Nn_i}\frac{d}{dx}\left(Nn_i\tilde{V}_{ix}\right) - V_{nx}\frac{1}{n_i}\frac{d\tilde{n}_i}{dx}\right] + \frac{\lambda_{ni}}{L_i}W_3\left[\tilde{V}_{ix} - \frac{\tilde{n}_i}{n_i}V_{nx}\right]. \quad (2.85)$$

Likewise, to first order in $\mathcal{L}$ the $\mathbf{x}$ component is given by

$$\tilde{V}_{nx} = -\frac{\tilde{N}}{N}V_{nx} - Z_1\left(\tilde{V}_{ix} - \frac{\tilde{n}_i}{n_i}V_{nx}\right) - i\lambda_{ni}\left[\frac{W_2}{Nn_i}\frac{d}{dx}\left(Nn_i\tilde{V}_{iy}\right)\right. \quad (2.86)$$
$$\left. + \frac{Z_2 v_{th}}{Nn_i}\frac{d}{dx}\left(\frac{\tilde{N}n_i}{2} - \tilde{n}_i N\frac{V_{nx}^2}{v_{th}^2}\right)\right] + \frac{\lambda_{ni}}{L_i}\left[W_3\tilde{V}_{iy} + Z_3 v_{th}\left(\frac{\tilde{N}}{2N} - \frac{\tilde{n}_i}{n_i}\frac{V_{nx}^2}{v_{th}^2}\right)\right].$$

The same method can be used to compute the perturbed neutral temperature. In this analysis, it is assumed that perturbations in temperature are small. Justification for this is provided in Sec. 2.6 for the fluid limit.

As a check on the kinetic calculation, it is useful to examine the collisional limit $\nu \gg 1$. It is easy to show that the kinetic result reduces to the expected fluid response for short mean free path. Neglecting an exponentially small piece, the expansion of Z_1 for large argument ($\zeta > 1$) is given by

$$Z_1(\zeta) = -\frac{i\nu}{\zeta}\left[1 + \frac{1}{2\zeta^2} + \frac{3}{4\zeta^4} + ...\right], \quad (2.87)$$

where $\zeta = \Lambda + i\nu$. In general, the expansion for large argument is given by

$$Z_m = i\frac{(-1)^m\nu^m}{\zeta^m}\left[1 + \frac{m(m+1)}{4\zeta^2} + \frac{m(m+1)(m+2)(m+3)}{32\zeta^4} + ...\right]. \quad (2.88)$$

Expanding Z_m and W_m in Eq. (2.79) to second order in this expansion gives

$$\frac{\tilde{N}}{N}\left(\overline{\overline{\omega}} + i\frac{k_y^2 v_{th}^2}{2\nu_{ni}}\right) = k_y\tilde{V}_{iy} - \frac{i}{N}\frac{d}{dx}\left(N\tilde{V}_{ix}\right) - i\frac{V_{nx}}{L_i}\frac{\tilde{n}_i}{n_i}, \quad (2.89)$$

where $\overline{\overline{\omega}} = \omega - k_y V_d$ and $\nu_{ni} \gg \overline{\overline{\omega}}$. Upon substituting the lowest order fluid solution for $\hat{\mathbf{V}}_i$, this result is in agreement with the response calculated from the collisional

fluid description in Eq. (2.42). Likewise considering the $\mathcal{L}^0$ terms in Eq. (2.85)-(2.86) and expanding the Z_m functions to lowest order in $1/\zeta$ yields

$$\tilde{V}_{ny} = \frac{i\nu_{ni}}{\overline{\overline{\omega}} + i\nu_{ni}} \tilde{V}_{iy} + \frac{k_y v_{th}^2}{2\left(\overline{\overline{\omega}} + i\nu_{ni}\right)} \frac{\tilde{N}}{N} , \tag{2.90}$$

$$\tilde{V}_{nx} = \frac{i\nu_{ni}}{\overline{\overline{\omega}} + i\nu_{ni}} \tilde{V}_{ix} - V_{nx} \left(\frac{i\nu_{ni}}{\overline{\overline{\omega}} + i\nu_{ni}} \frac{\tilde{n}_i}{n_i} + \frac{\tilde{N}}{N} \right) , \tag{2.91}$$

in agreement with the fluid result of Eq. (2.40) when $\overline{\overline{\omega}} \ll \nu_{ni}$. The next order terms in the Z_m expansions give terms in agreement with those arising from the neutral viscosity in the fluid description.

2.7.1 Local Dispersion Relationship

A local dispersion relationship valid for arbitrary $k_y \lambda_{ni}$ with $k_y L \gg 1$ is obtained by combining the fluid description for the ion perturbations with the lowest order Boltzmann response for the neutrals. It should be emphasized that the fluid description for the ions is valid regardless of whether $k_y \lambda_{ni}$ is large or small since we are considering interchange modes ($k_{||} = 0$) and small gyro-radius $\rho_i k_y \ll 1$. In this section, the ordering of Eq. (2.37) is relaxed to allow N and n_i to differ appreciably. In the case of divertors, the ratio N/n_i in the regions of interest may vary from 10 to 0.1 or smaller. It is also possible in high density divertors for $\nu_{ii} \sim \Omega_{ci}$. In these regimes, ion viscosity can play a significant role if $N/n_i < 1$ and is therefore included in this analysis. To summarize, the ordering assumed for this derivation is

$$\omega \ll \Omega_{ci} \qquad \nu_{in} \ll \Omega_{ci} \qquad \nu_{ii} \lesssim \Omega_{ci} \qquad k_y L \gg 1 \qquad L_n \sim L_i \sim L \ . \tag{2.92}$$

Consider first the ion momentum from Eq. (2.29). Taking the cross product with $\mathbf{B}$ yields

$$\mathbf{V}_i = \frac{\mathbf{E} \times \mathbf{B}}{B^2} c - \left[\frac{\nabla p_i}{\Omega_{ci} M n_i} + \frac{\nu_{in}}{\Omega_{ci}} \left(\mathbf{V}_n - \mathbf{V}_i \right) + \frac{\nabla \cdot \mathbf{\Pi}_i}{\Omega_{ci} n_i M} - \frac{1}{\Omega_{ci}} \frac{d\mathbf{V}_i}{dt} \right] \times \mathbf{b} \, . \tag{2.93}$$

where $\mathbf{\Pi}_i$ is the ion viscous stress tensor [20]. This stress tensor is composed of

collisional viscosity terms as well as *gyroviscosity* which represents a non-dissipative transport of momentum due to the finite ion gyro-radius. It is convenient to decompose the stress tensor into collisional and gyroviscosity terms $\mathbf{\Pi}_i = \mathbf{\Pi}_i^{coll} + \mathbf{\Pi}_i^{gyro}$ since there is a partial cancellation between the gyroviscous terms and a portion of dV_i/dt. This is sometimes referred to as "gyroviscous cancellation" and is discussed in detail by Hazeltine and Meiss [21]. A brief outline of this result is described here.

The gyroviscous cancellation involves terms from

$$\mathbf{H} \equiv Mn_i \frac{dV_i}{dt} + \nabla \cdot \mathbf{\Pi}_i^{gyro} \,. \tag{2.94}$$

In the absence of temperature gradients, the gyroviscous stress tensor is given by [21]

$$\mathbf{\Pi}_i^{gyro} = \mathbf{\Pi}_\perp + \mathbf{b}\mathbf{\Pi}_{||} + \mathbf{\Pi}_{||}\mathbf{b} \,, \tag{2.95}$$

where $\mathbf{\Pi}_\perp$ is the tensor

$$\mathbf{\Pi}_\perp = \frac{p_i}{2\Omega_{ci}} \left[(\mathbf{b} \times \nabla)\, \mathbf{V}_\perp + \nabla\, (\mathbf{b} \times \mathbf{V}_\perp) \right] \,, \tag{2.96}$$

$\mathbf{\Pi}_{||}$ is the vector

$$\mathbf{\Pi}_{||} = \frac{p_i}{\Omega_{ci}} \left[\mathbf{b} \times \nabla V_{||} + \mathbf{b} \cdot \nabla\, (\mathbf{b} \times \mathbf{V}_\perp) \right] \,, \tag{2.97}$$

and $\mathbf{V}_\perp$, $\mathbf{V}_{||}$ are the ion velocities parallel and perpendicular to the magnetic field. The lowest order terms in Eq. (2.93) are

$$\mathbf{V}_i \approx \frac{\mathbf{E} \times \mathbf{B}}{B^2} c - \frac{\nabla p_i \times \mathbf{b}}{\Omega_{ci} M n_i} = \mathbf{V}_E + \mathbf{V}_{pi} \,. \tag{2.98}$$

Substituting Eq. (2.98) into Eq. (2.94) and simplifying for the perpendicular component results in

$$\left[Mn_i \frac{dV_i}{dt} + \nabla \cdot \mathbf{\Pi}_i^{gyro} \right]_\perp = Mn_i \frac{d\mathbf{V}_E}{dt} - \nabla_\perp \left[\frac{p_i}{2\Omega_{ci}} \mathbf{b} \cdot \nabla \times (\mathbf{V}_E + \mathbf{V}_{pi}) \right] \,, \tag{2.99}$$

The terms involving $d\mathbf{V}_{pi}/dt$ cancel nearly exactly with $\nabla \cdot \mathbf{\Pi}_i^{gyro}$ leaving a piece left

over which is a gradient of a scalar. Furthermore, the piece left over cannot contribute to the instability because the contribution to $\mathbf{V}_i$ is of the form $(1/n_i)\nabla_\perp \times [\ ]$ and when calculating $\nabla \cdot (n_i \mathbf{V}_i)$ it will vanish. The dominant term in the collisional stress tensor is of the form

$$\nabla \cdot \mathbf{\Pi}_i \approx M n_i C_v \rho_i^2 \nu_{ii} \nabla^2 \mathbf{V}_i \ , \tag{2.100}$$

where $\rho_i = v_{th}/\Omega_{ci}$ is an ion gyro-radius and $C_v = 3/20$ is the coefficient resulting from a complete collisional transport calculation [20].

Taking into account the gyroviscous cancellation and the simplified form for the collisional viscosity Eq. (2.93) simplifies to

$$\mathbf{V}_i \approx \frac{\mathbf{E} \times \mathbf{B}}{B^2} c - \left[\frac{\nabla p_i}{\Omega_{ci} M n_i} + \frac{\nu_{in}}{\Omega_{ci}} (\mathbf{V}_n - \mathbf{V}_i) + C_v \frac{\nu_{ii}}{\Omega_{ci}} \rho_i^2 \nabla^2 \mathbf{V}_i - \frac{1}{\Omega_{ci}} \frac{d\mathbf{V}_E}{dt} \right] \times \mathbf{b} \ . \tag{2.101}$$

Using quasineutrality along with ion and electron continuity as done previously in Eq. (2.35) results in

$$\mathbf{b} \cdot \nabla \times \left[n_i \nu_{in} (\mathbf{V}_n - \mathbf{V}_i) + n_i C_v \nu_{ii} \rho_i^2 \nabla^2 \mathbf{V}_i - n_i \frac{d\mathbf{V}_E}{dt} \right] = 0 \tag{2.102}$$

which is similar to Eq. (2.36) in which neutral dynamics were already included. In the absence of temperature perturbations, the coupling to the neutral population is exclusively through the first term in Eq. (2.102). The procedure outlined here is to group the neutral perturbations arising from this term into a function and then to separately determine this function from the solution of the Boltzmann equation. Writing Eq. (2.102) explicitly in linearized form gives

$$\begin{aligned} ik_y \left[-n_i \frac{d\hat{V}_{Ex}}{dt} + n_i C_v \nu_{ii} \rho_i^2 \nabla^2 \hat{V}_{ix} + n_i \nu_{in} \left(\hat{V}_{nx} - \hat{V}_{ix} \right) + n_i \nu_{in} V_{nx} \left(\frac{\hat{n}_i}{n_i} + \frac{\hat{N}}{N} \right) \right] \\ - \frac{\partial}{\partial x} \left[-n_i \frac{d\hat{V}_{Ey}}{dt} + n_i C_v \nu_{ii} \rho_i^2 \nabla^2 \hat{V}_{iy} + n_i \nu_{in} \left(\hat{V}_{ny} - \hat{V}_{iy} \right) \right] = 0 \ . \end{aligned} \tag{2.103}$$

Assuming $\partial/\partial x \sim 1/L$ it is clear from Eq. (2.93) that $\hat{V}_{ix}/\hat{V}_{iy} \sim k_y L$. Likewise, using the solution to the Boltzmann equation to compare the perturbed neutral velocities

(See Eq. (2.85)-(2.86)) results in $\hat{V}_{nx}/\hat{V}_{ny} \sim k_y L$. Thus in Eq. (2.103) the terms in the first set of brackets are larger than the corresponding terms in the second set of brackets by $(k_y L)^2$. Dropping terms of order $1/(k_y L)^2$ Eq. (2.103) becomes

$$i\overline{\overline{\omega}}\hat{V}_{Ex} - C_v \nu_{ii} \left(\rho_i k_y\right)^2 \hat{V}_{ix} - \nu_{in}\left(\hat{V}_{ix} - V_{nx}\frac{\hat{n}_i}{n_i}\right) + \nu_{in}\left(\hat{V}_{nx} + \frac{\hat{N}}{N}V_{nx}\right) \approx 0\,, \quad (2.104)$$

where $\overline{\overline{\omega}} = \omega - k_y V_d$. Substituting the lowest order solution for $\hat{V}_{ix}$

$$\hat{V}_{ix} \approx \frac{-ik_y c\hat{\phi}}{B} - \frac{ik_y v_{th}^2}{2\Omega_{ci}}\frac{\hat{n}_i}{n_i}\,, \quad (2.105)$$

along with Eq. (2.28) for $\hat{n}_i$ gives

$$\left(\omega - \omega_{di}\right)\left[1 + C_v\left(k_y\rho_i\right)^2\frac{\nu_{ii}}{\nu_{in}}\right] - i\left[\gamma_o + \frac{\omega\overline{\overline{\omega}}}{\nu_{in}} + \frac{\omega B}{k_y c\hat{\phi}}\left(\hat{V}_{nx} + V_{nx}\frac{\hat{N}}{N}\right)\right] \approx 0\,, \quad (2.106)$$

where γ_o is the collisional growth rate in the absence of neutral perturbations (see Eq. (2.10)) The neutral response to the perturbation is included through the last two terms in Eq. (2.106) and is obtained by truncating the series solution for $\hat{V}_{nx}$ in Eq. (2.86) to zeroth order in λ_{ni}/L

$$\hat{V}_{nx} + \frac{\hat{N}}{N}V_{nx} \approx -Z_1\left(\hat{V}_{ix} - V_{nx}\frac{\hat{n}_i}{n_i}\right) = +iZ_1\left(1 - \frac{\omega_{di} + i\gamma_o}{\omega}\right)\frac{k_y c\hat{\phi}}{B}\,. \quad (2.107)$$

Substituting Eq. (2.107) into Eq. (2.106) results in the dispersion relation

$$\left[\omega - \left(\omega_{di} + i\gamma_o\right)\right]\left[1 + Z_1\right] + C_v\left(k_y\rho_i\right)^2\frac{\nu_{ii}}{\nu_{in}}\left(\omega - \omega_{di}\right) - i\frac{\omega\overline{\overline{\omega}}}{\nu_{in}} \approx 0\,, \quad (2.108)$$

valid for $k_y L \gg 1$. The Z_1 function describes the neutral response in both the collisional and collisionless limits, thus Eq. (2.108) is valid for for arbitrary $k_y\lambda_{ni}$.

2.7.2 Collisional Limit

In the collisional limit when the mean free path is small in comparison to the wavelength $\nu \gg 1$, it is easy to show that the kinetic result reduces to the previous fluid

result. Using the Z_1 expansion for large argument (see Eq. (2.87)) and expanding to second order in $1/\zeta$ gives

$$1 + Z_1 \approx -i\frac{\overline{\overline{\omega}}}{\nu_{ni}} + \frac{1}{2}k_y^2\lambda_{ni}^2 \,. \tag{2.109}$$

The general dispersion relation in Eq. (2.108) then simplifies to

$$[\omega - (\omega_{di} + i\gamma_o)]\left[-i\frac{\overline{\overline{\omega}}}{\nu_{ni}} + \frac{1}{2}k_y^2\lambda_{ni}^2\right] + C_v\left(k_y\rho_i\right)^2\frac{\nu_{ii}}{\nu_{in}}\left(\omega - \omega_{di}\right) - i\frac{\omega\overline{\overline{\omega}}}{\nu_{in}} \approx 0 \,, \tag{2.110}$$

in the collisional limit. The two terms involving $\overline{\overline{\omega}}$ originate from neutral and ion inertia. Notice that $\overline{\overline{\omega}}/\nu_{ni} \sim (\lambda_{ni}/L)^2$ is small in comparison to $(k_y\lambda_{ni})^2$ in the local approximation ($k_yL \gg 1$) so that neutral inertial is negligible. Likewise, the ion inertia term is also small provided $(k_yL)^2 \gg n_i/N$. The remaining terms in Eq. (2.110) are

$$[\omega - (\omega_{di} + i\gamma_o)] + 2C_v\left(\frac{\nu_{ni}}{\Omega_{ci}}\right)^2\frac{\nu_{ii}}{\nu_{in}}\left(\omega - \omega_{di}\right) \approx 0 \,. \tag{2.111}$$

The second term in Eq. (2.111) involves the ratio of ion viscosity to neutral viscosity (See Eq. (2.38)). For $N \approx n_i$ and $\nu_{ni}\nu_{ii}/\Omega_{ci}^2 \ll 1$ this term is small and the simplified dispersion relation of Eq. (2.50) is recovered $\omega \approx \omega_{di} + i\gamma_o$.

Notice that the viscous term in Eq. (2.111) can be significant even with $\nu_{ni} < \Omega_{ci}$ since it is possible for $\nu_{ii} \gg \nu_{in}$ in many plasmas of interest. For example in a hydrogen plasma at $T \approx 1$ eV, the ratio of the ion-ion to the ion-neutral collision frequency is $\nu_{ii}/\nu_{in} \approx 20(n_i/N)$. As discussed in Sec. 2-5, there are regions of importance in a divertor where $n_i/N \sim 10$ while ν_{ni}/Ω_{ci} may be as large as 0.1 which gives a significant contribution from this term. Solving Eq. (2.111) for ω

$$\omega \approx \omega_{di} + \frac{i\gamma_o}{1 + 2C_v\left(\frac{\nu_{ni}}{\Omega_{ci}}\right)^2\frac{\nu_{ii}}{\nu_{in}}} \,, \tag{2.112}$$

it is evident that this viscous contribution results in a smaller growth rate for the instability. This result is in agreement with the heuristic derivation of Sec. 2.4.

Equation (2.112) is similar to a previous result for gravitational interchange modes

derived by Coppi [17]. The relevant dispersion relation for a fully ionized plasma including ion-ion collisions (see Eq. (20) of reference [17]) is

$$(\omega - \omega_{di}) \left(\omega + i \frac{1}{8} \nu_{ii} (k_y \rho_i)^2 \right) = - \frac{g}{L_i} \ , \tag{2.113}$$

where the factor $\frac{1}{8}$ is due to the approximation used for the collision operator. The general dispersion relation derived in Eq. (2.108) may be put in a form that resembles Eq. (2.113). For the purpose of this heuristic explanation, it is convenient to take $\overline{\overline{\omega}} \approx \omega - \omega_{di}$ resulting in

$$(\omega - \omega_{di}) (\omega + i \nu_{eff}) = - \frac{g}{L_i} (1 + Z_1) \ , \tag{2.114}$$

where again $g = \nu_{in} V_{nx}$ and

$$\nu_{eff} = \nu_{in} (1 + Z_1) + C_v \nu_{ii} (k_y \rho_i)^2 \ . \tag{2.115}$$

Recall that the function Z_1 keeps track of the effect of neutral perturbations. In the collisionless limit $\lambda_{ni} k_y \gg 1$, the neutral "response" is negligible $Z_1 \to 0$ and the dispersion relation of Eq. (2.114) is consistent with the previous result of Coppi. In the collisional limit $\lambda_{ni} k_y \ll 1$, the expansion as given by Eq. (2.109) is $1 + Z_1 \approx (\lambda_{ni} k_y)^2 / 2$ resulting in an effective collision frequency

$$\nu_{eff} \approx \frac{\nu_{in}}{2} (\lambda_{ni} k_y)^2 + C_v \nu_{ii} (k_y \rho_i)^2 \ , \tag{2.116}$$

where first term represents the effect of neutral viscosity and the second term is due to the ion viscosity. Assuming $\omega \ll \nu_{eff}$, the relevant root of Eq. (2.114) is

$$\omega \approx \omega_{di} + i \frac{g}{\overline{\nu}_{eff} L_i} \ , \tag{2.117}$$

where

$$\overline{\nu}_{eff} = \nu_{in} \left[1 + \frac{n_i}{N} \frac{\mathcal{D}_i}{\mathcal{D}_N} \right] \ , \tag{2.118}$$

and $\mathcal{D}_i = C_v \nu_{ii} \rho_i^2$ is the ion viscous diffusion coefficient and $\mathcal{D}_N = v_{th}^2/(2\nu_{ni})$ is the neutral viscous diffusion coefficient. The first term in the effective collision frequency $\overline{\nu}_{eff}$ is the "normal" contribution from ν_{in} while the second term represents an enhancement due to perturbations in the neutral velocity. Intuitively, the magnitude of this term may be described as follows: The effect of ion-ion collisions gives rise to a perturbed ion drift velocity which tends to excite perturbations in the neutral velocity while the neutral viscosity $\mathcal{D}_N$ tends to damp out these perturbations. These results are in agreement with the heuristic derivation in Sec. 2.4.

2.7.3 Collisionless Limit

When the neutral-ion mean free path is much larger than the wavelength $\nu \ll 1$, the kinetic solution reduces to the simple picture described in Sec. 2.3. The expansion of Z_1 for small argument is given by

$$Z_1(\zeta) = i\nu \left[i\pi^{1/2} exp(-\zeta^2) - 2\zeta \left(1 - \frac{2}{3}\zeta^2 + \frac{4}{15}\zeta^4 - \frac{8}{105}\zeta^2 \right) \right] , \tag{2.119}$$

where $\zeta = \Lambda + i\nu$. Keeping the first two terms in this expansion, the dispersion relation of Eq. (2.108) simplifies to

$$[\omega - (\omega_{di} + i\gamma_o)] \left[1 + i\nu \left(i\pi^{1/2} exp(-\zeta^2) - 2\zeta \right) \right] + C_v \left(k_y \rho_i \right)^2 \frac{\nu_{ii}}{\nu_{in}} (\omega - \omega_{di}) - i\frac{\omega\overline{\overline{\omega}}}{\nu_{in}} \approx 0 . \tag{2.120}$$

Clearly, for $\nu \ll 1$ the contribution from neutral perturbations is negligible. Typically, this long neutral-ion mean free path regime occurs when the neutral density exceeds the ion density by a large margin. In this regime, $(\rho_i k_y)^2 \nu_{ii}/\nu_{in} \ll 1$ and the ion viscosity is also negligible. The remaining terms in Eq. (2.120) are

$$\omega \left(1 - i\frac{\overline{\overline{\omega}}}{\nu_{in}} \right) \approx \omega_{di} + i\gamma_o, \tag{2.121}$$

and for $\overline{\overline{\omega}} \ll \nu_{in}$ the ion inertia term is also small. In this limit, the simple dispersion relation $\omega \approx \omega_{di} + i\gamma_o$ is obtained. Notice this result for $\nu \ll 1$ and $N \gg n_i$ is identical

to Eq. (2.50) where $\nu \gg 1$, $N \sim n_i$ and ion viscosity was assumed to be negligible since $\nu_{ii}\nu_{ni} \ll \Omega_{ci}^2$. This is because in these two special limits perturbations in the neutral population are negligible leaving only the ion dynamics which are identical in each case.

In the limit of long neutral-ion mean free path, the perturbed neutral density from Eq. (2.79) and the perturbed neutral velocities (Eq. (2.85)-(2.86)) are both small. Intuitively this result seems correct, since the only way in which the neutrals can "feel" a perturbation in the plasma is through collisions with ions. When neutrals must travel a distance much longer than a wavelength before interacting with an ion, perturbations in the plasma are no longer "visible" to the neutrals. Since the mean free path is still small in comparison to the unperturbed scale lengths, the neutrals still enter into the equilibrium providing the effective gravity discussed in Sec. 2.3. This is the regime typically encountered in the ionosphere when dealing with the equatorial spread F. Here the scale size of the irregularities vary from 100 m to 10 km but the peak plasma densities are of the order $n_i \sim 10^6$ cm^{-3} resulting in $\lambda_{ni} \sim 500$ km.

2.7.4 Intermediate Case

In the intermediate regime where $k_y\lambda_{ni} \sim 1$, there is no expansion available for Z_1 and Eq. (2.108) must be solved numerically. It is convenient to re-write Eq. (2.108) in dimensionless form

$$\left[\hat{\omega} - \left(\frac{\rho_i}{L_i} + i\hat{\gamma}_o\right)\right][1 + Z_1] + C_v\,(k_y\rho_i)^2\,\frac{\nu_{ii}}{\nu_{in}}\left(\hat{\omega} - \frac{\rho_i}{L_i}\right) - i\frac{\hat{\omega}\Lambda}{\nu}\frac{n_i}{N} \approx 0\,, \qquad (2.122)$$

where $\hat{\omega} = \omega/(k_y v_{th})$, $\hat{\gamma}_o = \gamma_o/(k_y v_{th})$, $\Lambda = \hat{\omega} - V_d/v_{th}$ and $\nu = \nu_{ni}/(k_y v_{th})$. There are six independent dimensionless parameters characterizing the problem $\nu = 1/k_y\lambda_{ni}$, $\rho_i k_y$, $k_y L_i$, L_i/L_n, ν_{ii}/ν_{in} and N/n_i. The appropriate ion-ion collision frequency is given by [20]

$$\nu_{ii} = \frac{4\sqrt{\pi}\lambda_c e^4 Z^4 n_i}{3\sqrt{M}T_i^{3/2}} = \frac{1}{3\times 10^6}\left(\frac{\lambda_c}{10}\right)\left(\frac{2M_p}{M}\right)^{1/2}\frac{Z^4 n_i}{T_i^{3/2}}\,, \qquad (2.123)$$

where the Coulomb logarithm is $\lambda_c = 23.4 - 1.15log(n_i) + 3.45log(T)$ for $T < 50$ eV with T in units of eV and n_i in units of cm^{-3}. For the purpose of finding a numerical solution, we assume hydrogen with $n_i \sim 10^{14}$ cm^{-3} and $T \sim 1$ eV resulting in $\lambda_c \approx 7.3$ and $\nu_{ii} \approx 3.5 \times 10^{-7} n_i/T^{3/2}$ sec^{-1}. The appropriate ion-neutral collision frequency [19] is given by $\nu_{in} = 2.93\sigma_x(T/M)^{1/2}N$. The charge exchange cross section for hydrogen ($H + H^+ \rightarrow H^+ + H$) at 1 eV is $\sigma_x \approx 5 \times 10^{-15}$ cm^2 and slightly greater for deuterium $\sigma_x \approx 6 \times 10^{-15}$ cm^2 [22, 23]. Recent results indicate [22] that the cross section for elastic collisions between ions and neutrals is larger than previously thought so that the effective cross section for neutral-ion collisions is somewhat larger. For this analysis, it is assumed $\sigma_x \approx 6 \times 10^{-15}$ cm^2, resulting in the ratio

$$\frac{\nu_{ii}}{\nu_{in}} \approx 20 \frac{n_i}{N} \frac{1}{T^2} , \tag{2.124}$$

with T in unit of eV. For the numerical solution presented here, it is assumed $T \approx 1$ eV so that ν_{ii}/ν_{in} is determined by the density ratio.

Using standard numerical methods, a program was written to find the roots of Eq. (2.122). The imaginary part of the frequency is shown as a function of ν in Fig. 2-3 and the real part of the frequency is shown in Fig. 2-4. The real part is normalized to ω_{di} while the imaginary part is normalized to the idealized collisional growth rate γ_o from Eq. (2.10). Each curve corresponds to a different ratio of the neutral to plasma density N/n_i. As expected for $N \gg n_i$, the growth rate approaches the idealized case of Eq. (2.10) where neutral perturbations are negligible. For moderate ratios of N/n_i, deviations from this idealized case are significant. For $\nu \gg 1$, the growth rates in Fig. 2-3 are in agreement with the collisional result of Eq. (2.112). Typically, the maximum growth rates occur for $k_y\lambda_{ni} \sim 1$. Deviations from $\omega_r \approx \omega_{di}$ are small except in the region $\nu < 1$. For $N/n_i > 1$ and $\nu < 1$ the real frequency can significantly exceed ω_{di} since the diamagnetic drift includes contributions from both the plasma and neutral pressure.

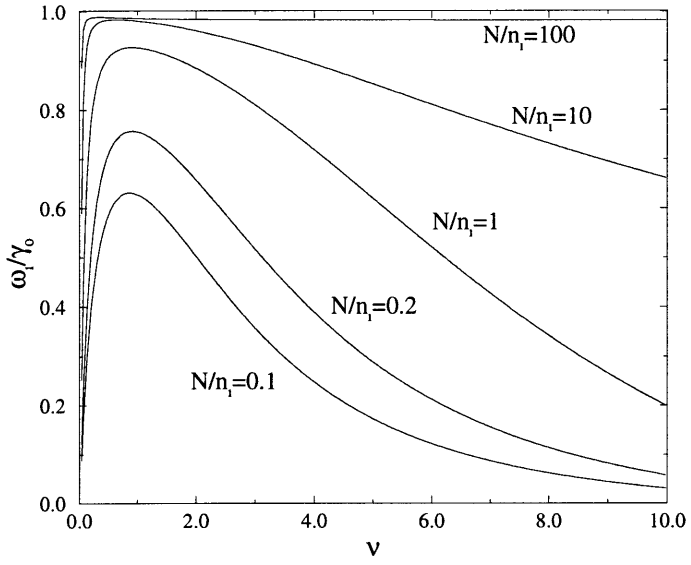

Figure 2-3: Imaginary part of the solution to Eq. (2.122) with $\rho_i k_y = 0.05$, $k_y L_i = 10$, $L_i/L_n = 1$

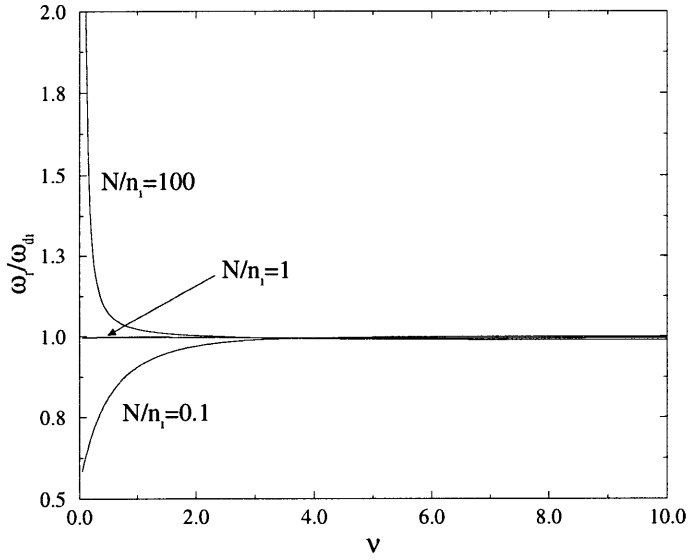

Figure 2-4: Real part of the solution to Eq. (2.122) with $\rho_i k_y = 0.05$, $k_y L_i = 10$, $L_i/L_n = 1$

2.8 Normal Mode Equation

In Sec. 2.5 and Sec. 2.7, algebraic forms for the dispersion relation were developed for very short wavelength modes $k_y L \gg 1$. In this section, a true normal mode analysis for short wavelength modes is performed to show that the lowest order corrections to the local growth growth rate are stabilizing. For simplicity, we fall back to the MHD description of the plasma

$$\rho \frac{d\mathbf{V}}{dt} = -\nabla p + \frac{\mathbf{J} \times \mathbf{B}}{c} + \rho \nu_{in} \left(\mathbf{V}_n - \mathbf{V} \right) \ , \tag{2.125}$$

where ρ is plasma mass density of the plasma and it is assumed

$$\mathbf{E} + \frac{\mathbf{V} \times \mathbf{B}}{c} = 0 \ . \tag{2.126}$$

The neutrals are again modeled with fluid equations

$$\rho_n \frac{d\mathbf{V}_n}{dt} = -\nabla p_n + \rho_n \nu_{ni} (\mathbf{V} - \mathbf{V}_n) - \nabla \cdot \mathbf{\Pi}_n \ , \tag{2.127}$$

where $\rho_n = NM$ is the mass density of neutrals. Assuming the neutral viscosity coefficient is a weak function of position, the viscous stress tensor from Eq. (2.31) can be simplified

$$\nabla \cdot \mathbf{\Pi}_n \approx \frac{\rho_n v_{th}^2}{2\nu_{ni}} \left(\nabla^2 \mathbf{V}_n + \frac{1}{3} \nabla (\nabla \cdot \mathbf{V}_n) \right) \ . \tag{2.128}$$

This assumption is valid if the neutral pressure and plasma density decrease roughly in the same manner so that $\rho_n v_{th}^2 / \nu_{ni}$ varies weakly across the mode. The MHD equilibrium equivalent to Sec. 2.2 is given by

$$V_x = V_y = V_{ny} = 0 \ , \tag{2.129}$$

$$V_{nx} = -\frac{1}{\rho \nu_{in}} \frac{\partial p_n}{\partial x} \ , \tag{2.130}$$

$$J_y = \frac{c}{B} \frac{\partial}{\partial x} (p + p_n) \qquad J_x = 0 \ .$$

Consider normal mode perturbations of the form

$$\hat{\mathbf{V}} = \tilde{\mathbf{V}}(x)\, exp(-i\omega t + ik_y y)\ , \tag{2.131}$$

where $k_{||} = 0$. Adding ion and neutral momentum to eliminate the exchange term and perturbing gives

$$\rho\frac{\partial\hat{\mathbf{V}}}{\partial t} + \rho_n\frac{d\hat{\mathbf{V}}_n}{dt} = -\nabla\left[\hat{p} + \hat{p}_n + \frac{1}{4\pi}\mathbf{B}\cdot\hat{\mathbf{B}}\right] + \frac{\rho_n v_{th}^2}{2\nu_{ni}}\left[\nabla^2\hat{\mathbf{V}}_n + \frac{1}{3}\nabla\left(\nabla\cdot\hat{\mathbf{V}}_n\right)\right]\ , \tag{2.132}$$

where Ampere's law has been used to eliminate $\mathbf{J}$ and it is assumed $k_{||} = 0$. Notice that a number of the terms are a simple gradient of a scalar quantity. This includes the second part of the viscous term, assuming the viscous coefficient varies weakly across the mode. These terms are eliminated by taking $\mathbf{b}\cdot\nabla\times$ of Eq. (2.132) resulting in

$$\begin{aligned} -i\omega\left[\frac{\partial}{\partial x}\left(\rho\hat{V}_y\right) - ik_y\rho\hat{V}_x\right] \;=\; & \frac{\partial}{\partial x}\left[\left(\rho_n\frac{v_{th}^2}{2\nu_{ni}}\nabla_\perp^2 + i\rho_n\omega - \rho_n V_{nx}\frac{\partial}{\partial x}\right)\hat{V}_{ny}\right] \\ & -ik_y\rho_n\left(\frac{v_{th}^2}{2\nu_{ni}}\nabla_\perp^2 + i\omega - \frac{\partial V_{nx}}{\partial x} - V_{nx}\frac{\partial}{\partial x}\right)\hat{V}_{nx}\ , \end{aligned} \tag{2.133}$$

where

$$\nabla_\perp^2 \equiv \frac{\partial^2}{\partial x^2} - k_y^2\ .$$

Since the mass flux $\rho_n V_{nx}$ is constant and we are neglecting the weak variation in $\rho_n v_{th}^2/\nu_{ni}$, Eq. (2.133) simplifies to

$$\begin{aligned} -i\omega\left[\frac{\partial}{\partial x}\left(\rho\hat{V}_y\right) - ik_y\rho\hat{V}_x\right] = \rho_n\left[\frac{v_{th}^2}{2\nu_{ni}}\nabla_\perp^2 + i\omega - V_{nx}\frac{\partial}{\partial x}\right]\left(\frac{\partial\hat{V}_{ny}}{\partial x} - ik_y\hat{V}_{nx}\right) \\ +i\omega\frac{\partial\rho_n}{\partial x}\hat{V}_{ny} + ik_y\rho_n\frac{\partial V_{nx}}{\partial x}\hat{V}_{nx}\ . \end{aligned} \tag{2.134}$$

For electrostatic perturbations $\nabla\cdot\hat{\mathbf{V}} \approx 0$ allowing $\hat{V}_y$ to be written as

$$\hat{V}_y = \frac{i}{k_y}\frac{\partial\hat{V}_x}{\partial x}\ . \tag{2.135}$$

In addition, the mass continuity equation for the plasma with $\nabla \cdot \hat{\mathbf{V}} \approx 0$ gives

$$\hat{\rho} = \frac{\hat{V}_x}{i\omega}\frac{\partial \rho}{\partial x} \,. \tag{2.136}$$

Now recall that to lowest order in $\omega/\nu_{ni} \ll 1$ and $\lambda_{ni}k_y \ll 1$ the perturbed neutral and plasma velocities are related by Eq. (2.40) restated here for clarity

$$\hat{\mathbf{V}}_n = \hat{\mathbf{V}} - \frac{v_{th}^2 \nabla \hat{\rho}_n}{2\rho_n \nu_{ni}} + \frac{v_{th}^2}{2\rho_n \nu_{ni}}\left[\frac{\hat{\rho}_n}{\rho_n} + \frac{\hat{\rho}}{\rho}\right]\nabla \rho_n \,. \tag{2.137}$$

Taking $\mathbf{b} \cdot \nabla \times$ of Eq. (2.137) gives

$$\left(\frac{\partial \hat{V}_{ny}}{\partial x} - ik_y \hat{V}_{nx}\right) = \left(\frac{\partial \hat{V}_y}{\partial x} - ik_y \hat{V}_x\right) + i\frac{k_y v_{th}^2}{2\nu_{ni}}\left(\frac{1}{L_n}\frac{\hat{\rho}}{\rho} - \frac{1}{L_i}\frac{\hat{\rho}_n}{\rho_n}\right) \,, \tag{2.138}$$

where

$$\frac{1}{L_n} \equiv -\frac{1}{\rho_n}\frac{d\rho_n}{dx} \qquad \frac{1}{L_i} \equiv -\frac{1}{\rho}\frac{d\rho}{dx} \,. \tag{2.139}$$

Combining Eqns. (2.135) - (2.136) and Eq. (2.138) with Eq. (2.134) and simplifying gives

$$\begin{aligned} i\omega\left[\frac{\partial}{\partial x}\left(\rho\frac{\partial \hat{V}_x}{\partial x}\right) - k_y^2 \rho \hat{V}_x + \frac{\partial \rho_n}{\partial x}\left(\frac{\partial \hat{V}_x}{\partial x} - \frac{k_y^2 v_{th}^2}{2\nu_{ni}}\frac{\hat{\rho}_n}{\rho_n}\right)\right] \\ -k_y^2 V_{nx}\frac{\partial \rho_n}{\partial x}\left[\hat{V}_{ix}\left(1 - \frac{i\gamma_o}{\omega}\right) - \frac{v_{th}^2}{2\nu_{ni}}\frac{\partial}{\partial x}\left(\frac{\hat{\rho}_n}{\rho_n}\right)\right] \\ +\rho_n\left(\frac{v_{th}^2}{2\nu_{ni}}\nabla_\perp^2 + i\omega - V_{nx}\frac{\partial}{\partial x}\right)\left[\left(\nabla_\perp^2 + ik_y^2\frac{\gamma_o}{\omega}\right)\hat{V}_x - \frac{k_y^2 v_{th}^2}{2\nu_{ni}L_i}\frac{\hat{\rho}_n}{\rho_n}\right] = 0 \,, \end{aligned} \tag{2.140}$$

where $\gamma_o = V_{nx}/L_i$. The last equation to consider is neutral continuity shown in Eq. (2.41). Inserting Eq. (2.137) into Eq. (2.41) and simplifying results in

$$\left[i\omega + \frac{v_{th}^2}{2\nu_{ni}}\nabla_\perp^2 + \frac{v_{th}^2}{2\nu_{ni}L_i}\frac{\partial}{\partial x}\right]\hat{\rho}_n = \hat{V}_x\frac{\partial \rho_n}{\partial x} + \rho_n V_{nx}\frac{\partial}{\partial x}\left(\frac{\hat{V}_x}{i\omega L_i}\right) \,, \tag{2.141}$$

which is a diffusion equation for $\hat{\rho}_n$ with source terms arising from perturbations in the plasma velocity $\hat{V}_x$. The normal modes of the system are described by the two coupled differential equations (2.140)-(2.141). Simplifying these to a single differential

equation appears difficult. Thus far the main assumptions are neglecting neutral temperature perturbations and assuming the neutral viscous coefficient varies weakly across the mode. To make progress analytically, one must make assumptions about the relative magnitudes of the various terms.

Consider an ordering similar to Eq. (2.37) with short but finite wavelengths. The procedure outlined is to keep terms of order $1/(k_y L)$ while discarding all terms of higher order in this parameter. In making comparisons, it is assumed

$$\frac{\partial}{\partial x} \sim \left(\frac{k_y}{L}\right)^{1/2} \qquad \frac{\omega \nu_{ni}}{k_y^2 v_{th}^2} \sim \frac{1}{k_y^2 L^2} , \tag{2.142}$$

which is justified a posteriori by Eq. (2.149) and Eq. (2.151). The leading order terms in this expansion arise from the neutral viscosity $(\rho_n v_{th}^2/\nu_{ni})\,\nabla_\perp^2$. Terms in Eq. (2.140) corresponding to neutral and ion inertia are all second order and higher in this expansion and can be neglected. This simplifies Eq. (2.140) to

$$\left(\frac{\partial^2}{\partial x^2} - k_y^2\right)\left[\frac{\partial^2 \hat{V}_x}{\partial x^2} - k_y^2\left(1 - \frac{i\gamma_o}{\omega}\right)\hat{V}_x - \frac{k_y^2 v_{th}^2}{2\nu_{ni}}\frac{\hat{\rho}_n}{\rho_n}\frac{1}{L_i}\right] \approx 0 , \tag{2.143}$$

which corresponds to $\mathbf{b}\cdot\nabla\times\left(\nabla\cdot\hat{\mathbf{\Pi}}_n\right) \approx 0$. From Eq. (2.141), the leading order expression for neutral density perturbations is

$$\frac{k_y^2 v_{th}^2}{2\nu_{ni}}\frac{\hat{\rho}_n}{\rho_n} \approx -\frac{\hat{V}_x}{L_n} + V_{nx}\frac{\partial}{\partial x}\left(\frac{\hat{V}_x}{i\omega L_i}\right) , \tag{2.144}$$

which simplifies Eq. (2.143) to

$$\left(\frac{\partial^2}{\partial x^2} - k_y^2\right)\left[\frac{\partial^2 \hat{V}_x}{\partial x^2} - k_y^2\left(1 - \frac{i\gamma_o}{\omega}\right)\hat{V}_x + \hat{V}_x\frac{1}{L_n L_i} + \frac{i\gamma_o}{\omega}\frac{\partial}{\partial x}\left(\frac{\hat{V}_x}{L_i}\right)\right] \approx 0 . \tag{2.145}$$

Clearly the terms entering from the neutral density perturbation are of higher order and can be dropped. Examining Eq. (2.145) it is evident that to order $1/(k_y L)$ the only surviving terms are

$$\left(\frac{\partial^2}{\partial x^2} - k_y^2\right)\hat{V}_x + ik_y^2\frac{\gamma_o}{\omega}\hat{V}_x \approx 0 . \tag{2.146}$$

This equation for the mode profile is of the same form other researchers have found for the $\mathbf{E} \times \mathbf{B}$ [7] and Raleigh-Taylor instabilities [24]. It can be solved by assuming there is a maximum growth rate at some point x_o and expanding about it

$$\gamma_o = \frac{V_{nx}}{L_i} = \gamma_o \left(1 - \frac{(x - x_o)^2}{L^2}\right) , \tag{2.147}$$

where γ_o is the maximum growth rate. This expansion is justified a posteriori by Equation (2.149) which shows the eigenfunction has a spatial extent of $|x - x_o| \sim (L/k_y)^{1/2}$.

With this final simplification, Eq. (2.146) reduces to the harmonic oscillator equation from quantum mechanics,

$$\frac{\partial^2 \tilde{V}_x}{\partial x^2} - k_y^2 \left[1 - i\frac{\gamma_o}{\omega}\left(1 - \frac{(x - x_o)^2}{L^2}\right)\right] \tilde{V}_x \approx 0 . \tag{2.148}$$

The eigenfunction of the fundamental mode is then

$$\tilde{V}_x = \tilde{V}_{xo}\, exp\left[-\frac{(x - x_o)^2}{2\delta^2}\right] , \tag{2.149}$$

where

$$\delta^2 = \left|\frac{L}{k_y}\right| \sqrt{\frac{\omega}{i\gamma_o}} , \tag{2.150}$$

and $\tilde{V}_{xo}$ is the mode amplitude. The corresponding eigenvalue is

$$\omega \approx i\gamma_o \left[1 - \frac{1}{|k_y L|} + \mathcal{O}\left(\frac{1}{k_y L}\right)^2\right] . \tag{2.151}$$

This result is valid for $k_y L \gg 1$. It was obtained by neglecting neutral density perturbations while retaining perturbations in the neutral velocity

$$\tilde{V}_{nx} \approx \tilde{V}_x \left(\frac{(x - x_o)^2}{L^2} - \frac{1}{|k_y L|}\right) , \tag{2.152}$$

since $\tilde{V}_{nx}/\tilde{V}_x \sim 1/(k_y L)$ while terms entering from $\hat{\rho}_n$ are of higher order.

2.9 Realistic Conditions for Existence

The realistic conditions for this type of mode to exist may be quite different than implied by a simple flute-mode analysis. By assuming $k_{||} = 0$ in the flute-mode calculations, the electromagnetic contribution was arbitrarily neglected. In many cases, this assumption is completely unjustified. In reality, it make little sense to assume that a quantity is zero without making appropriate comparisons in the relevant equations that describe the physics. In the case of this instability, the relevant comparison involves a term with $k_{||}V_A$ where $V_A = B/(4\pi\rho)^{1/2}$ is the Alfvén velocity. Even though $k_{||}$ may be small, in many cases V_A may be quite large, resulting in a drastically different dispersion relation for realistic wavelengths along the field.

In this section, the realistic conditions for the existence of the instability are examined. It is shown that for realistic $k_{||}$ a coupling exist between the unstable interchange mode and a stabilizing shear Alfvén mode. As pointed out by Basu and Coppi [24] in connection with the ionosphere, this effect can be large in certain regimes causing modes which are unstable for a pure flute mode analysis to be damped or marginally stable for realistic $k_{||}$. If the frozen-in condition ($E_{||} = 0$) is assumed to hold, the modes that exist are ideal MHD electromagnetic rather than electrostatic. However, for the strongly collisional plasmas which occur in a divertor, the frozen-in condition is violated and the plasma can slip across the field lines. In this regime, the growth rate of the unstable interchange mode is reduced considerably by the coupling to the shear Alfvén mode.

To examine the stabilizing influence of the shear Alfvén mode, consider an MHD description for the plasma and for simplicity neglect perturbations in the neutral population $\hat{\mathbf{V}}_n = \hat{\rho}_n = 0$. As discussed in Sec. 2.3, the equilibrium neutral flow can be thought of as an effective gravity $g = \nu_{in}V_{nx}$. With this analogy, the problem is identical to the previous analysis of Basu and Coppi [24]. Using Ampere's Law to eliminate the current density, the perturbed momentum equation becomes

$$\rho\frac{\partial\hat{\mathbf{V}}}{\partial t} = -\nabla\left[\hat{p} + \frac{1}{4\pi}\mathbf{B}\cdot\hat{\mathbf{B}}\right] + \frac{1}{4\pi}\mathbf{B}\cdot\nabla\hat{\mathbf{B}} + \hat{\rho}\mathbf{g} - \rho\nu_{in}\hat{\mathbf{V}}\,. \tag{2.153}$$

The other equations relevant to the analysis are

$$\nabla \times \mathbf{E} = -\frac{1}{c}\frac{\partial \mathbf{B}}{\partial t} , \tag{2.154}$$

$$\nabla \times \mathbf{B} = \frac{4\pi}{c}\mathbf{J} , \tag{2.155}$$

$$\mathbf{E} + \frac{1}{c}\mathbf{V} \times \mathbf{B} = \eta_{\|}\mathbf{J}_{\|} + \eta_{\perp}\mathbf{J}_{\perp} , \tag{2.156}$$

where $\eta_{\|}$ and $\eta_{\perp}$ are resistivities parallel and perpendicular to the magnetic field arising from electron-ion collisions. It is straightforward to combine the previous three equations into a diffusion equation for the magnetic field

$$\frac{\partial \mathbf{B}}{\partial t} = \mathcal{D}_M \nabla^2 \mathbf{B} + \nabla \times (\mathbf{V} \times \mathbf{B}) , \tag{2.157}$$

where $\mathcal{D}_M = c^2\eta_{\|}/4\pi = c^2\nu_{ei}/\omega_{pe}^2$ is the magnetic diffusion coefficient. For this analysis, we consider incompressible perturbations $\nabla \cdot \hat{\mathbf{V}} \approx 0$ of the form

$$\hat{V} = \tilde{V}(x)\, exp[-i\omega + ik_y y + ik_{\|} z]. \tag{2.158}$$

The diffusion equation for the magnetic field simplifies to

$$-i\omega\hat{\mathbf{B}} = ik_{\|}B\hat{\mathbf{V}} + \mathcal{D}_M \left[\frac{\partial^2}{\partial x^2} - k_y^2\right]\hat{\mathbf{B}} . \tag{2.159}$$

To obtain an algebraic dispersion relation for the very short wavelength modes we replace $\partial/\partial x$ with ik_x. Combining $\mathbf{b} \cdot \nabla\times$ of Eq. (2.153) with Eq. (2.159) results in

$$i\omega\left[\nu_{in} - i\omega + \frac{\left(k_{\|}V_A\right)^2}{\mathcal{D}_M k_{\perp}^2 - i\omega}\right] = -\frac{k_y^2}{k_{\perp}^2}\frac{g}{L_i} , \tag{2.160}$$

where $k_{\perp}^2 = k_x^2 + k_y^2$.

In the limit where $\mathcal{D}_M k_{\perp}^2 \ll \omega$, the magnetic diffusion time is large in comparison to the growth time of the mode. Thus the frozen-in law is valid and the plasma and the magnetic field are constrained to move together. The dispersion relation in this

limit is

$$i\omega\left(\nu_{in}-i\omega\right)=\left(k_{\|}V_A\right)^2-\frac{k_y^2}{k_\perp^2}\frac{g}{L_i}\,, \tag{2.161}$$

and the instability condition is given by

$$\left(k_{\|}V_A\right)^2<\frac{k_y^2}{k_\perp^2}\frac{g}{L_i}\,. \tag{2.162}$$

Coppi and Basu point out that for parameters appropriate to the the F-region of the ionosphere, the stabilizing influence of the shear Alfvén mode is sufficient to damp the ideal MHD modes. To explain the plasma depletion process associated with the Equatorial Spread F, it is essential to consider spatially localized modes that allow the plasma to move independently of the magnetic field. Coppi and Basu propose gravity-driven dissipative modes [24] which topologically resemble ballooning modes [25, 26] and are excited when gravity is directed against the density gradient.

The limit appropriate to the collisional plasmas which occur in the divertor region is $\mathcal{D}_M k_\perp^2 \gg \omega$. In this case, the frozen-in-law is broken and the plasma can slip across the magnetic field. In addition $\nu_{in} \gg \omega$ in this region, so that the relevant root of the dispersion relation is

$$\omega\approx i\frac{g}{\nu_{in}L_i}\frac{k_y^2}{k_\perp^2}\left[1+\frac{\left(k_{\|}V_A\right)^2}{k_\perp^2\mathcal{D}_M\nu_{in}}\right]^{-1}\,. \tag{2.163}$$

The collisional growth rate obtained previously is reduced by a coupling parameter related to the shear Alfvén mode. For parameters appropriate to the divertor region, the coupling parameter in Eq. (2.163) may be of order unity. In the interest of simplicity, the neutral perturbations have been neglected in the above analysis. As discussed previously, these terms are significant and should be retained.

Recalling the prescription on page 26, it is rather easy to modify the above analysis to include the effect of neutral perturbations. This is accomplished by making the

substitution $\nu_{in} \rightarrow \nu_{in}\mathcal{G}$ in Eq. (2.160) resulting in

$$i\omega \left[\nu_{in}\mathcal{G} - i\omega + \frac{\left(k_{\|}V_A\right)^2}{\mathcal{D}_M k_\perp^2 - i\omega} \right] = -\frac{k_y^2}{k_\perp^2}\frac{g}{L_i}\mathcal{G} \ . \tag{2.164}$$

In the limit appropriate to a divertor plasma $\omega \ll \mathcal{D}_M k_\perp^2$ with $\omega \ll \nu_{in}\mathcal{G}$, the relevant root is

$$\omega \approx i\frac{g}{\nu_{in}L_i}\frac{k_y^2}{k_\perp^2}\left[1 + \frac{\left(k_{\|}V_A\right)^2}{k_\perp^2 \mathcal{D}_M \nu_{in}\mathcal{G}} \right]^{-1} \ . \tag{2.165}$$

The parameters appropriate to a divertor are $B_T \approx 5$ T, $T_e \approx T_i \approx 1$ eV, $n_i \sim 10^{14}$ cm^{-3}, $N \sim 10^{14}$ cm^{-3}, $k_{\|}/k_\perp = L_\perp/L_{\|}$, $L_{\|} \sim 3$ m and $L_\perp \sim 1$ cm. These values give $V_A \approx 1 \times 10^9$ cm/sec, $\mathcal{D}_M \approx 6 \times 10^6$ cm^2/sec, $\nu_{in} \approx 2 \times 10^6$ sec^{-1}, $\lambda_{ni}k_\perp \approx 3$, $\mathcal{G} \approx 0.6$ and $k_{\|}/k_\perp \approx 0.003$ which results in the following estimate for the coupling parameter

$$\frac{\left(k_{\|}V_A\right)^2}{k_\perp^2 \mathcal{D}_M \nu_{in}\mathcal{G}} \approx 1.3 \ .$$

The plasma density in certain regions of the divertor may be as large as $n_i \sim 10^{15}$ cm^{-3} resulting in $V_A \approx 3.4 \times 10^8$ cm/sec, $\lambda_{ni}k_\perp \approx 0.3$, $\mathcal{G} \approx 0.04$ and a value for the coupling parameter

$$\frac{\left(k_{\|}V_A\right)^2}{k_\perp^2 \mathcal{D}_M \nu_{in}\mathcal{G}} \approx 2.2 \ .$$

Since the plasma is not rigidly tied to the magnetic field, the coupling to the shear Alfvén mode is substantially diminished from the ideal MHD case. As this coupling parameter becomes small, the modes found are nearly electrostatic in nature. In a divertor plasma, the coupling parameter is comparable to the terms arising from the original flute mode analysis. This term results in a considerable reduction of the growth rate, thus dropping the electromagnetic contribution is clearly unjustified in the flute-mode analysis.

2.10 Equilibrium E × B Drifts

Since equilibrium electric fields may occur in conjunction with a neutral pressure gradient, it is important to consider the modifications to the theory due to the presence of equilibrium $\mathbf{E} \times \mathbf{B}$ drifts. In this section, a brief description of the $\mathbf{E} \times \mathbf{B}$ instability is given followed by a discussion of the effect of uniform electric fields on the neutral pressure gradient instability. Finally, the more realistic case of nonuniform electric fields is discussed.

2.10.1 The E × B Instability

The flute-type $\mathbf{E} \times \mathbf{B}$ instability may occur in a partially ionized plasma in which a uniform electric field is perpendicular to both the magnetic field and the density gradient [4, 5, 6, 7, 8]. It is important to emphasize, that when considering this instability all previous researchers have examined the regime where the neutral density greatly exceeds the ion density so that the mean free path for a neutral-ion collision is much larger than either the wavelength or the macroscopic length scale. In this limit, it is appropriate to consider the neutrals as an immobile background uneffected by perturbations in the plasma. In plane geometry, the simplest equilibrium to consider is a uniform electric field in the **y** direction, a uniform magnetic field in the **z** direction and a density variation in the **x** direction. Due to the electric field E_y, the plasma has an $\mathbf{E} \times \mathbf{B}$ drift in the **x** direction while the neutrals remain immobile. The relative velocity between the plasma and neutral background gives rise to an effective gravity $g = -\nu_{in} V_{ix}$ due to ion-neutral collisions. For collisional regimes $\gamma \ll \nu_{in}$, the growth rate of a gravitational interchange mode is $\gamma = g/(\nu_{in} L_i)$. Thus the growth rate of the $\mathbf{E} \times \mathbf{B}$ instability is $\gamma = -V_{ix}/L_i$ where $V_{ix} = E_y c/B$. This is very similar to the neutral pressure gradient instability in the limit $N \gg n_i$ where neutral perturbations are negligible and $\gamma = V_{nx}/L_i$. Recall that in the limit $N \gg n_i$, the neutral perturbations are small when $k_y \lambda_{ni} \gg 1$ since the neutrals no longer "see" perturbations in the plasma and when $k_y \lambda_{ni} \ll 1$ (also with $N \gg n_i$) the neutral viscosity dissipates perturbations on a time scale faster than the growth time of the

mode.

In conjunction with a real gravity g, the $\mathbf{E} \times \mathbf{B}$ instability is sometimes referred to as the the generalized Rayleigh-Taylor instability. This case has been widely studied in connection with the ionosphere [11, 24, 27]. As mentioned previously, in the F-layer of the ionosphere the neutral density greatly exceeds the plasma density $N \gg n_i$. The equatorial spread F occurs after sunset in the presence of a large eastward electric field which causes the ionospheric plasma layer to move vertically upward to higher altitudes. In addition to the real gravity, the neutrals also exert a collisional force on the plasma due to the upward $\mathbf{E} \times \mathbf{B}$ drift. Thus, the growth rate of the generalized Rayleigh-Taylor instability in the collisional limit $\gamma \ll \nu_{in}$ is

$$\gamma = \frac{g}{\nu_{in} L_i} - \frac{V_{ix}}{L_i} \,. \tag{2.166}$$

Depending on the sign of E_y, the equilibrium electric field may either enhance or weaken the instability. For sufficiently large $E_y \geq Bg/(\nu_{in} c)$, the mode may be stabilized by the uniform equilibrium E_y electric field. It should be emphasized that the above results are for the regime $N \gg n_i$. In the following section, it is pointed out that for the regime of interest in this analysis $\lambda_{ni} \ll L$ the $\mathbf{E} \times \mathbf{B}$ instability is greatly diminished and a uniform E_y does not alter the growth rate of the neutral pressure gradient instability. However, in reality electric fields are typically nonuniform and the resulting sheared $\mathbf{E} \times \mathbf{B}$ velocity may drastically alter the topology and growth rate of the mode.

2.10.2 Uniform Electric Field in Regime $\lambda_{ni} \ll L$

In the relevant regime for the $\mathbf{E} \times \mathbf{B}$ instability, the neutrals are decoupled from the motion of the plasma since $N \gg n_i$. In contrast, the regime of interest for this thesis is $\lambda_{ni} \ll L$ so that the ion and neutral velocities are coupled and the equilibrium is properly described by fluid equations for the neutrals and ions. In the presence of a uniform E_y field, the equilibrium momentum balance for the plasma and neutrals

results in

$$
\begin{aligned}
V_{ix} &= \frac{E_y c}{B}\,, \\
V_{iy} &= V_{ny} = \frac{c}{e n_i B}\left[\frac{d}{dx}\left(p_i + p_n\right)\right] \\
V_{nx} &= \frac{E_y c}{B} - \frac{1}{M N \nu_{ni}}\frac{dp_n}{dx}\,,
\end{aligned}
\tag{2.167}
$$

where terms of order $(\lambda_{ni}/L)^2$ have been neglected. The velocity difference between the neutrals and ions is due entirely to the neutral pressure gradient and the E_y field gives a uniform drift to both neutrals and ions. Using a reference frame moving with $V_{ix} = E_y c/B$, the equilibrium in Eq. (2.167) is identical to the original equilibrium considered in this analysis and dispersion relation of Eq. (2.108) remains unchanged.

Next consider the case of a uniform electric field in the **x** direction. The equilibrium momentum balance results in

$$
\begin{aligned}
V_{ix} &= 0\,, \\
V_{iy} &= V_{ny} = -\frac{E_x c}{B} + \frac{c}{e n_i B}\left[\frac{d}{dx}\left(p_i + p_n\right)\right]\,, \\
V_{nx} &= -\frac{1}{M N \nu_{ni}}\frac{dp_n}{dx}\,.
\end{aligned}
\tag{2.168}
$$

In comparison to the original equilibrium considered in this analysis (see Eq. (2.5)), the only modification is a new uniform drift $E_x c/B$ in the **y** direction. Therefore, the new dispersion relationship is obtained by substituting $\omega \to \omega + k_y E_x c/B$ in the previous result from Eq. (2.108). It is clear that the primary effect is a Doppler shift to the real part of the frequency while the growth rate remains unchanged. In the more realistic case of nonuniform $E_x(x)$, the Doppler shifted frequency is a function of x and modifications to the theory are substantial.

2.10.3 Nonuniform Electric Field

In order to maintain an equilibrium with divergence-free currents, it is often necessary to consider nonuniform electric fields. The analysis of these regimes with sheared

$\mathbf{E} \times \mathbf{B}$ velocity is considerably more complicated [28, 29]. The case of a shear in the $\mathbf{y}$ component of the $\mathbf{E} \times \mathbf{B}$ drift resulting from a nonuniform $E_x(x)$ has been considered by several researchers [7, 24]. The resulting nonuniform $\mathbf{E} \times \mathbf{B}$ velocity introduces an x-dependent Doppler shift $k_y V_{ey}(x) = k_y E_x(x) c/B \equiv \omega_E(x)$ and a new term $\hat{V}_{ix} dV_{ey}/dx$ in the y-component of the momentum equation. For short wavelength modes $k_y L \gg 1$, the dominant influence is contained in the x-dependent Doppler shifted frequency $\varpi(x) = \omega + \omega_E(x) - k_y V_d$. The amount of velocity shear necessary to significantly alter the instability for short wavelength modes may be estimated by expanding about the point of maximum gradient x_o

$$\varpi \approx \varpi(x_o) + \left.\frac{d\omega_E}{dx}\right|_{x=x_o} (x - x_o) \tag{2.169}$$

Roughly speaking, the effect of sheared $\mathbf{E} \times \mathbf{B}$ velocity becomes important when

$$\left.\frac{d\omega_E}{dx}\right|_{x=x_o} (x - x_o) \sim \gamma \tag{2.170}$$

where γ is the growth rate of the mode.

This simple estimate is consistent with the analysis of Perkins and Doles who consider the flute-type $\mathbf{E} \times \mathbf{B}$ instability (see Sec. 2.10) and show the main effect of $\varpi(x)$ is to stabilize the short wavelength modes preferentially [7]. Recently, Basu and Coppi have solved the problem of the modes that are found in the presence of gravity, $\mathbf{E} \times \mathbf{B}$ drifts and neutral wind velocity taking into account that the modes are localized along a field line [30]. Recall that the $\mathbf{E} \times \mathbf{B}$ instability is similar to the neutral pressure gradient driven instability, with the relative velocity due to an electric field in the $\mathbf{y}$ direction. The regime considered in both of these analyses is $N \gg n_i$. In the presence of a gravity $\mathbf{g}$ and electric field $\mathbf{E} = E_o(x)\mathbf{e}_x$, the equilibrium drift velocities are

$$\mathbf{V}_e \approx \frac{c\,(\mathbf{E} \times \mathbf{B})}{B^2}\,, \tag{2.171}$$

$$\mathbf{V}_i \approx \frac{c\,(\mathbf{E} \times \mathbf{B})}{B^2} + \frac{1}{\Omega_{ci}} \left(\mathbf{g} - \nu_{in} \frac{c\,(\mathbf{E} \times \mathbf{B})}{B^2} \right) \times \mathbf{b}\,, \tag{2.172}$$

To maintain an equilibrium with divergence-free currents, one must require

$$\frac{d}{dx}\left(n_i E_o\right) = 0, \tag{2.173}$$

where the variations in B and ν_{in} are neglected. Equation (2.173) implies that the spatial variation of the electric field is related directly to the density variation $n_i(x)$.

The normal mode analysis is performed by considering short wavelength modes localized about the point x_o where $d\ln n_i/dx$ is maximum

$$\frac{d\ln n_i}{dx} \approx \frac{1}{L_{io}}\left[1 - \frac{(x-x_o)^2}{L_i^2}\right] . \tag{2.174}$$

For a uniform E_y field, the analysis of Perkins and Doles indicates that the $\mathbf{E}\times\mathbf{B}$ instability is stabilized (see Eq. (22) in Ref. [7]) when

$$\frac{E_x(x_o)}{E_y} > \frac{2}{|k_y L_i|} , \tag{2.175}$$

where L_i is scale length for the variation of density and electric field. Notice that this is consistent with the simple estimate of Eq. (2.170). The local growth rate for the $\mathbf{E}\times\mathbf{B}$ instability is $\gamma = (cE_y/B)(d\ln n_i/dx)$ and $d\omega_E(x)/dx = -\omega_E(d\ln n_i/dx)$ so that the estimate of Eq. (2.170) implies that the sheared electric field is significant when $E_x(x_o)k_y(x-x_o) \sim E_y$ and taking $(x-x_o) \sim L_i$ results in the comparison $E_x \sim E_y/(k_y L)$.

Heuristically, the result of Perkins and Doles and the simple estimate of Eq. (2.170) may be extended to the neutral pressure gradient instability by neglecting the effect of neutral perturbations $\hat{\mathbf{V}}_n = \hat{N} = 0$ and assuming that the variation in $E_o(x)$ is simply related to the variation of $n_i(x)$ by Eq. (2.173). In this case, the growth rate of the instability is $\gamma = V_{nx}/L_i$ and the stability condition analogous to Eq. (2.175) is

$$E_x(x_o) > \frac{B|V_{nx}|}{c}\frac{2}{|k_y L_i|} . \tag{2.176}$$

In reality, neutral perturbations do play a significant role for the regimes consid-

ered in this analysis. A proper treatment should include these effects along with the sheared $\mathbf{E} \times \mathbf{B}$ velocity. The existence condition and topology of the neutral pressure gradient driven instability may be modified substantially by the presence of sheared $\mathbf{E} \times \mathbf{B}$ velocities. Unfortunately, even without the additional complications of sheared flows, the non-local analysis of this problem is quite difficult.

2.11 Gravity Driven Modes

Although the neutral pressure gradient driven instability is similar to a gravitational interchange mode, there are important differences. The effective gravity acting on the ions from the neutral flow is an internal force and does not appear in the total momentum conservation equation. In contrast, real gravity does appear in the total momentum conservation equation. Due to this important difference, the effect of the neutral perturbations on an instability with real gravity is quite different. To illustrate this point, consider the same equilibrium with the addition of a real gravity g in the $\mathbf{x}$ direction

$$\begin{aligned} V_{ix} &= 0\,, \\ V_{nx} &= \frac{g}{\nu_{ni}} - \frac{1}{MN\nu_{ni}}\frac{dp_n}{dx}\,, \\ V_{ny} &= V_{iy} = \frac{c}{en_iB}\left[\frac{d}{dx}\left(p_i + p_n\right)\right] - \left(1 + \frac{N}{n_i}\right)\frac{g}{\Omega_{ci}}\,. \end{aligned} \tag{2.177}$$

If the neutral pressure gradient balances with gravity, the neutrals are in a situation similar to a hydrostatic equilibrium with $V_{nx} = 0$. Otherwise, the neutrals flow across the field as before and the effective gravity includes both the real gravity and the collisional force the neutrals exert on the plasma.

Now consider perturbations about this equilibrium and examine the total momentum conservation equation

$$n_i\left(\gamma + k_y^2\mathcal{D}_i\right)\hat{V}_{ix} + N\left(\gamma + k_y^2\mathcal{D}_N\right)\hat{V}_{nx} + \hat{n}_i g \approx 0\,. \tag{2.178}$$

The neutral momentum conservation from Eq. (2.19) is unchanged

$$\hat{V}_{nx} = \hat{V}_{ix}\left(1 - \frac{V_{nx}}{\gamma L_i}\right) . \tag{2.179}$$

Combining Eq. (2.178) and Eq. (2.179) gives

$$\frac{\hat{V}_{nx}}{\hat{V}_{ix}} \approx 1 - \frac{V_{nx}}{\gamma L_i} \approx -\frac{n_i}{N}\frac{\left(\gamma + k_y^2 \mathcal{D}_i\right)}{\left(\gamma + k_y^2 \mathcal{D}_N\right)} + \frac{n_i}{N}\frac{g}{L_i\left(\gamma + k_y^2 \mathcal{D}_N\right)} . \tag{2.180}$$

Replacing the neutral viscosity terms with generalized neutral response function $\mathcal{G}$ (see page 26) and taking the limit $\gamma \ll k_y^2 \mathcal{D}_i$ and $\gamma \ll k_y^2 \mathcal{D}_i$ results in the dispersion relation

$$\gamma \approx \frac{V_{nx}}{L_i}\left[\frac{\nu_{in}\mathcal{G}}{\nu_{in}\mathcal{G} + k_y^2 \mathcal{D}_i}\right] + \frac{g}{L_i}\left[\frac{1}{\nu_{in}\mathcal{G} + k_y^2 \mathcal{D}_i}\right] . \tag{2.181}$$

The first term is the contribution to the growth rate from a neutral flow and is identical to the previous result of Eq. (2.22). In this term, it is clear that the effect of neutral perturbations is to reduce the growth rate relative to the case $\lambda_{ni} k_y \gg 1$ where the neutral response is small and $\mathcal{G} \to 1$. The second term in Eq. (2.181) is the contribution to the growth rate from a real gravity. In this term, the effect of the neutral response is to increase the growth rate relative to the case $\lambda_{ni} k_y \gg 1$.

2.12 Relevance to Divertor

In this analysis, it was assumed that temperatures were uniform with $T_i = T_n$. In the presence of neutral temperature gradients, the growth rate is still of the form $\gamma_o = V_{nx}/L_i$ where L_i is the plasma density scale length. However, the neutral flow velocity is driven by a neutral pressure gradient, so the appropriate modification to Eq. (2.9) is

$$\gamma_o \approx \frac{V_{th}^2}{\nu_{ni} L_i L_p} , \tag{2.182}$$

where $1/L_p = -(d \ln p_n / dx)$ is the neutral pressure scale length. The instability will occur when there is a flow of neutrals in the direction of decreasing plasma density

$L_p L_i > 0$.

An example of current interest where an instability of this nature might have relevance is the divertor region of a tokamak. Typically in the divertor at some distance from divertor target, the neutral pressure falls off as the plasma density increases resulting in $L_p L_i < 0$. However, it is possible that $L_p L_i$ may be positive in the so-called detached divertor regime characterized by a low plasma temperature ($T \leq 1$ eV) and strong plasma recombination [31]. In this regime, a plasma/neutral re-circulation pattern can occur and the neutral pressure profile can be reversed. Schematically, such a pattern is shown in Fig. 2-5. Plasma entering a low temperature region from upstream recombines increasing the neutral density in this region. The increased neutral pressure drives a flow of neutrals across the magnetic field lines toward the side wall and then upstream towards high temperature region where their ionization results in the plasma flux (along the magnetic field lines) back to the recombination region. In addition, the plasma density near the side walls is usually smaller than in the central zone. Thus the neutral flow from the recombination region is in the opposite direction as the plasma density gradient. As a result, $L_p L_i$ can be positive in the recombination region for detached operation of a tokamak divertor and an instability of the type discussed in this paper can be triggered. This instability may significantly alter plasma parameters and affect plasma recombination which is a crucial element of detached divertor regimes [32].

Characteristic parameters in the detached divertor regime are of the order $n_e \sim 10^{15}$ cm^{-3} and $N \sim 1 \times 10^{14}$ cm^{-3} and $T_i \approx T_n \approx 1$ eV. For these parameters, the mean free path for neutral ion collisions $\lambda_{ni} \sim 0.5$ mm is small in comparison to the macroscopic scale lengths $L \sim 2$ cm. Therefore, a collisional fluid description of the instability in this region is appropriate. Considering short wavelength modes with $k_y L \approx 10$ gives $k_y \approx 5$ cm^{-1} and $\nu = 1/(k_y \lambda_{ni}) \approx 4$. For a typical toroidal field of $B_T \approx 5$ T, the gyro-radius for a deuterium ion is $\rho_i \approx 0.03$ mm giving $k_y \rho_i \approx 0.015$. The growth rate of the instability determined by Eq. (2.122) for these parameters is $\omega_i/\gamma_o \approx 0.7$ where γ_o is the ideal growth rate from Eq. (2.10). When realistic $k_{||} = 2\pi/L_{||}$ is included as discussed in Sec. 2.9, the coupling to the shear Alfvén

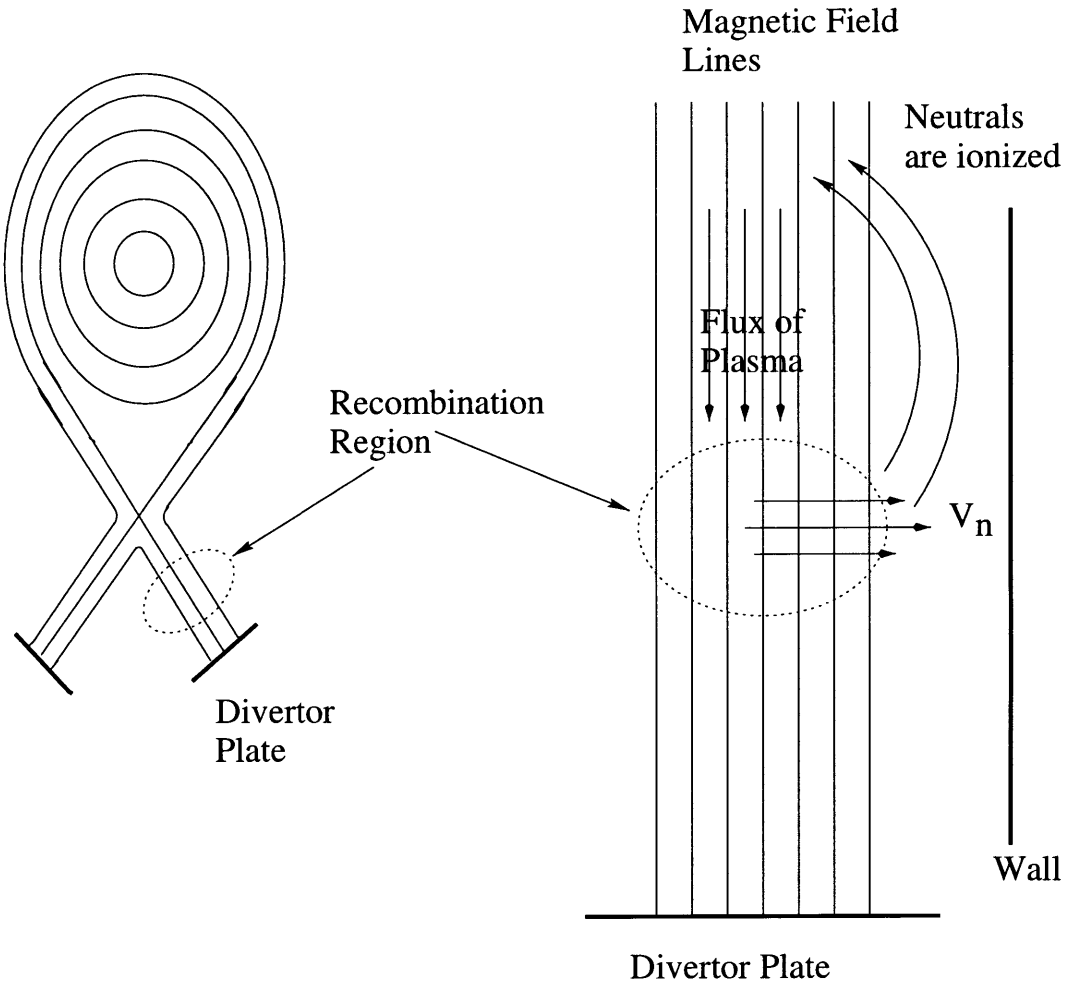

Figure 2-5: Schematic of re-circulation pattern in detached divertor regime

mode reduces the growth rate to $\omega_i/\gamma_o \approx 0.3$ assuming $L_{||} \approx 3$ m. One would expect the long wavelength modes $k_y L \sim 1$ to have the greatest effect on the equilibrium, but as mentioned previously this limit is difficult to treat analytically.

2.13 Summary

An interchange instability driven by a neutral pressure gradient was derived in both fluid and kinetic regimes. It is unusual in that the driving factor for the instability comes from an inhomogeneity in a neutral population. The instability can occur over a wide range of parameters. The results obtained in the various regimes considered

are summarized in Table 2.1.

Using the local approximation $k_y L \gg 1$, simple analytic results for the dispersion relation are obtained in the limits $k_y \lambda_{ni} \ll 1$ and $k_y \lambda_{ni} \gg 1$. Neutral perturbations are weak in the limit $k_y \lambda_{ni} \gg 1$ because plasma perturbations are no longer "felt" by the neutrals when the mean free path is long enough that they average over many wavelengths. In this regime, the growth rate is identical in form to that obtained in previous research for the $\mathbf{E} \times \mathbf{B}$ instability. As discussed in Sec. 2.10, the $\mathbf{E} \times \mathbf{B}$ instability may occur in regimes where $N \gg n_i$ when an equilibrium electric field is perpendicular to both the magnetic field and the plasma density gradient. The equilibrium electric field gives rise to a plasma drift $\mathbf{V}_i \approx c\left(\mathbf{E} \times \mathbf{B}\right)/B^2$. For the $\mathbf{E} \times \mathbf{B}$ instability, the neutrals are assumed to be an immobile background medium so that the relative velocity is due to the $\mathbf{E} \times \mathbf{B}$ drift of the plasma. The effective gravity $g = -\nu_{in}\mathbf{V}_i$ for the $\mathbf{E} \times \mathbf{B}$ instability is of the same form as the effective gravity $g = \nu_{in}\mathbf{V}_n$ for the neutral pressure gradient instability. Therefore, when perturbations in the neutral population are negligible, the form of the growth rate for the two instabilities is identical. For the regime considered in this analysis $\lambda_{ni} \ll L$, an appropriate fluid equilibrium must be considered for the neutral fluid as well as the plasma. In this case, the relative velocity between the ions and the neutrals must be driven by a neutral pressure gradient and the $\mathbf{E} \times \mathbf{B}$ instability is greatly diminished.

In the collisional limit $k_y \lambda_{ni} \ll 1$, perturbations in the neutral velocity are significant while perturbations in the neutral density and temperature are small. The main effect of the neutral velocity perturbations is to reduce the growth rate. The regime $k_y \lambda_{ni} \sim 1$ is solved numerically for a range of parameters. For values of N/n_i appropriate to a tokamak divertor, the maximum growth rates occur for $k_y \lambda_{ni} \sim 1$.

The realistic conditions under which an instability of this nature may exist are more restrictive than implied by the simple flute-mode analysis. This analysis indicates the instability will occur when the neutral pressure gradient is in the same direction as the plasma density gradient $L_p L_i > 0$. For realistic longitudinal wavelengths, an important coupling to the shear Alfvén mode occurs. In plasmas where the frozen-in law is valid $\mathcal{D}_M k_\perp^2 \ll \omega$, this coupling is quite strong since the magnetic

field and plasma are constrained to move together. The resulting instability condition in this limit is very restrictive $(k_{||}V_A)^2 < g/L_i$ for typical values of the effective gravity $g = \nu_{in}V_{nx}$. For the collisional plasmas $\mathcal{D}_M k_\perp^2 \gg \omega$ present in the divertor region, the coupling is substantially reduced. However, it is important to note that the contribution arising from finite $k_{||}$ is comparable in magnitude to the terms arising from the original flute-mode analysis. In assessing whether the neutral pressure gradient mode may occur in real situations, it is important to consider the effects of equilibrium $\mathbf{E} \times \mathbf{B}$ drifts. Sheared $\mathbf{E} \times \mathbf{B}$ flows are known to substantially modify the topology and existence condition for a number of instabilities. The complexities of the general problem including neutral pressure gradients and sheared $\mathbf{E} \times \mathbf{B}$ flows may require a numerical treatment. The following is a summary of the realistic conditions under which the pressure gradient driven instability may exist.

1. $L_p L_i > 0$ The neutral flow must be in right direction across the field to create an unstable equilibrium for gravitational interchange. This type of equilibrium probably does not occur in the normal operation of a divertor. However, it is possible that the necessary equilibrium may occur in the so-called detached divertor regime discussed in Sec. 2.12.

2. $\mathcal{D}_M k_\perp^2 \gg \omega$ Practically speaking, the frozen-in law must be broken to allow the plasma to slip across the field and avoid the extremely rigid requirements on $k_{||}$ obtained in the ideal MHD limit. Substituting the basic form for the growth rate this condition reduces to $(k_\perp L)^2 \gg (v_{th}^2/\nu_{ni})/\mathcal{D}_M$.

3. Nonuniform radial electric fields and the subsequent sheared $\mathbf{E} \times \mathbf{B}$ may substantially alter the topology or cause a transition to a non-normal mode. This is a complicated problem that deserves further study.

As mentioned previously, this instability may have relevance to the divertor region in toroidally confined laboratory plasmas. The low plasma temperatures required for a significant neutral population are present in the detached divertor regime and it is plausible that the instability condition $L_p L_i > 0$ is satisfied in areas of strong plasma

recombination. These areas of strong plasma recombination have been shown in recent years to be an essential element of detached divertor regimes. Thus understanding the coupling to the neutral population and the potential instabilities in this region is an important area of research.

Although a complete non-local treatment of the mode is analytically difficult, the shortest wavelength modes obey a harmonic oscillator equation which is identical in form to other interchange instabilities. The longer wavelength modes $k_y L \sim 1$ are described by a fourth order differential equation for $\hat{V}_x$ coupled to a second order differential equation for the neutral density. Numerical treatment in this regime seems essential.

As mentioned in the introduction, there are a numerous examples in space where instabilities of this general type are relevant. For the ionosphere, the neutral density greatly exceeds the plasma density at altitudes of importance and the effect of neutral density perturbations is quite negligible. On the other hand, in the local interstellar medium near the heliosphere there exist a partially ionized plasma with a plasma density in the range 0.05-0.4 cm^{-3} and a neutral density in the range 0.05-0.25 cm^{-3} [33, 34, 35]. The expanding solar wind plasma meets the interstellar medium at some as yet undetermined position beyond the planets and beyond the position of Voyager 1 and 2, presently at 61 and 47 AU respectively. For the solar wind, the plasma density is typically 5 cm^{-3} at 1 AU and falls off roughly as $1/r^2$ so that at 50 AU the plasma density is approximately 0.002 cm^{-3}. The neutral density at 50 AU is typically in the range 0.1 cm^{-3} , a factor of 50 larger than solar wind plasma but comparable to the neutral density in the interstellar medium. At the heliopause, where the solar wind stagnates against the interstellar medium, the plasma density is expected to increase sharply. The ratio of plasma to neutral density varies by almost two orders of magnitude from $N/n_i \sim 50$ at 50 AU to $N/n_i \sim 1$ outside the heliosphere in the local interstellar medium. The flow of neutrals from the interstellar medium is directed opposite to the density gradient and the effective gravity due to charge exchange collisions may cause a Rayleigh-Taylor-like instability to develop. As pointed out in the introduction, numerical treatment of this problem has been

attempted recently [9]. Unfortunately, it is not appropriate to apply the results of this analysis to the case of the heliopause because the magnetic fields are weak and the ions are essentially unmagnetized. Since the growth rates resulting from simulation [9] differ significantly from theoretical calculations which ignore the neutrals, this calculation might be a good direction for future work on this subject.

Table 2.1: Summary of results

Local Analysis with $k_{||} = 0$, $k_y L_i \gg 1$ and $k_y L_n \gg 1$

General Dispersion Relationship from Eq. (2.108)

$$[\omega - (\omega_{di} + i\gamma_o)]\,[1 + Z_1] + C_v\,(k_y \rho_i)^2\,\frac{\nu_{ii}}{\nu_{in}}\,(\omega - \omega_{di}) - i\frac{\omega\overline{\overline{\omega}}}{\nu_{in}} \approx 0$$

Collisional $k_y \lambda_{ni} \ll 1$	**Intermediate** $k_y \lambda_{ni} \sim 1$	**Collisionless** $k_y \lambda_{ni} \gg 1$
See Eq. (2.112)	Figures (2-3) - (2-4)	See Eq. (2.121)
$\omega \approx \omega_{di} + \frac{i\gamma_o}{1+2C_v\left(\frac{\nu_{ni}}{\Omega_{ci}}\right)^2 \frac{\nu_{ii}}{\nu_{in}}}$		$\omega\left(1 - i\frac{\overline{\overline{\omega}}}{\nu_{in}}\right) \approx \omega_{di} + i\gamma_o$

Local Analysis for Realistic $k_{||}$ for $k_y L_i \gg 1$, $k_y L_n \gg 1$

See Eq. (2.164)

$$i\omega\left[\nu_{in}\mathcal{G} - i\omega + \frac{\left(k_{||} V_A\right)^2}{\mathcal{D}_M k_\perp^2 - i\omega}\right] = -\frac{k_y^2}{k_\perp^2}\frac{g}{L_i}\mathcal{G}$$

Normal Mode Analysis for $k_y L_i \gg 1$, $k_y L_n \gg 1$ and $k_y \lambda_{ni} \ll 1$

See Eq. (2.149) - Eq. (2.151)

$$\tilde{V}_x = \tilde{V}_{xo}\, exp\left[-\frac{(x-x_o)^2}{2\delta^2}\right] \qquad \delta \approx \left|\frac{L}{k_y}\right|^{1/2}$$

$$\omega \approx i\gamma_o\left[1 - \frac{1}{|k_y L|}\right]$$

Chapter 3

The Ubiquitous Modes

3.1 Introduction

The transport of thermal energy in magnetically confined plasmas with temperatures in the multi-keV range is one the most important unresolved issues in plasmas physics. The observed thermal confinement in a broad range of experiments has consistently shown that the transport is much larger than can be understood based on collisional transport theory [36]. Thus, the primary focus for explaining the observed transport has turned to the effects of micro-instabilities.

Numerous instabilities have been proposed as candidates for explaining the outward transport of thermal energy. Among the most compelling of these instabilities are the so-called "ubiquitous" modes [37, 38, 39]. There are a number of theoretical reasons for considering these modes as a plausible factor in energy transport. The modes are driven by the combined effects of the plasma pressure gradient and of the local magnetic curvature drift of the trapped electrons and of circulating and trapped ions. These instabilities can be active over a significant portion of the plasma column and can involve a range of perpendicular wavelengths extending well beyond the ion gyro-radius, thus allowing transport over macroscopic scale lengths. Calculations indicate that for realistic parameters the thermal energy flux from these modes is generally much larger than the corresponding particle flux [39, 40], a feature that is consistent with the experimental observation that the particle confinement time is

significantly longer than the energy confinement time. In addition to these considerations, the spectra of fluctuations observed in toroidal magnetically confined plasmas is consistent with the characteristics of the ubiquitous modes. In experiments carried out on the PLT and PDX machines [41, 42], the spectra are peaked around $k_\perp \rho_s \approx 0.5$ and in experiments performed in the Text machine [43] at $k_\perp \rho_s \approx 0.1 \rightarrow 0.2$. These observations appear to involve phase velocities in both the electron and ion diamagnetic velocities.

In this chapter, a description of the basic elements of the ubiquitous modes is given following closely the original work of Coppi and Rewoldt [37]. The ubiquitous modes are of the standing type along a magnetic field line. Among the possible standing modes, one must distinguish between *even* and *odd* modes depending on whether the profile of the associated electric potential along a given field line is symmetric or antisymmetric about the point of minimum magnetic field. An important distinction to note is that the even parity modes are influenced by the trapped electron population while the odd parity modes are not since the average over a trapped particle orbit of the mode potential is zero. The original paper on the ubiquitous modes [37] considered the case of even parity while subsequent work considered both parities in detail [38, 44].

3.2 Heuristic Model

In this section, a simplified description of the processes involved in the excitation of the ubiquitous modes is given in a one-dimensional plane geometry. Although this greatly simplifies the calculation, it should be emphasized that the essential ingredients in the mode arise from the features of a two-dimensional equilibrium : the curvature drift and trapped electrons. These effects are included in this heuristic model by simulating the trapped electrons as a separate population and by introducing an effective gravity to account for the curvature drifts. The heuristic model presented in this section is backed up by several rigorous calculations in toroidal geometry [37, 38, 44].

All equilibrium quantities are assumed to depend only on x and the confining

magnetic field B is taken in the z direction. The limit $8\pi n(T_i + T_e)/B^2 \ll 1$ is considered. The relevant modes are electrostatic with the fluctuating electric field given by $\hat{\mathbf{E}} = -\nabla\hat{\phi}$. The perturbed electrostatic potential is of the form

$$\hat{\phi} = \tilde{\phi}(x)\, exp(-i\omega t + ik_y y + ik_{||} z) \;, \tag{3.1}$$

where $k_{||} \geq 2\pi/L$ and L is the relevant length of the system along a field line. Modes localized around $x = x_o$ are considered with $d\ln\tilde{\phi}/dx \ll k_y$ so that $\tilde{\phi}(x) \approx \tilde{\phi}(x_o)$. The phase velocity is assumed to be intermediate between the electron and ion thermal velocities $v_{thi} < \omega/k_{||} < v_{the}$ and the appropriate range of frequencies to consider is

$$\langle\omega_{ti}\rangle < \omega < \langle\omega_{be}\rangle < \langle\omega_{te}\rangle \;, \tag{3.2}$$

where $\langle\omega_{ti}\rangle$ is the mean ion transit frequency and $\langle\omega_{be}\rangle$ and $\langle\omega_{te}\rangle$ are the mean electron bounce and transit frequencies. Assuming the magnetic field is periodically modulated by ΔB over a distance L, the average bounce frequency $\langle\omega_b\rangle$ is of order $(2\pi v_{th}/L)(\Delta B/B)$ while the average transit frequency $\langle\omega_t\rangle$ is of order $2\pi v_{th}/L$.

Since the frequency of the mode is large in comparison to the mean ion transit frequency $\omega > \langle\omega_{ti}\rangle$, the ion response can be described as a single population regardless of whether a fraction of the ion population has magnetically trapped orbits. Neglecting ion temperature gradients and assuming $|\omega_{Di}| \ll |\omega_{*i}|$, the perturbed ion density is

$$\frac{\hat{n}_i}{n} = -\frac{e\hat{\phi}}{T_i}\left[1 - \left(1 - \frac{\omega_{*i}}{\omega}\right) I_o(b_i) exp(-b_i)\left(1 + \frac{\omega_{Di}}{\omega}\right)\right] \;, \tag{3.3}$$

where $\omega_{*i} = (k_y c T_i/eB)(d\,\ln n/dx)$, I_o is a modified Bessel function of the first kind, $b_i = \frac{1}{2}k_y^2\rho_i^2$ and $\omega_{Di} = k_y g_i/\Omega_{ci}$ where $g_i \approx v_{thi}^2/R_o$ is an effective gravitational field acting on the ions which is introduced to account for the curvature drift and R_o is the radius of magnetic curvature. The magnetic curvature is taken to be in the opposite direction of the density gradient.

In this case, the trapped electrons can be modeled as a separate cold population [45] with $v_{the||} < \omega/k_{||} < v_{the}$ where $v_{the||}$ is the effective parallel thermal velocity

of the trapped electrons and v_{the} is the thermal velocity of the circulating electrons. The perturbed density of the trapped electron population $\hat{n}_{eT}$ is given by the mass continuity equation

$$\frac{\partial \hat{n}_{eT}}{\partial t} + \nabla \cdot \left(\mathbf{V}_{eT} \hat{n}_{eT} + \hat{\mathbf{V}}_{eT} n_{eT} \right) = 0 \,, \tag{3.4}$$

where $\mathbf{V}_{eT} = -g_{eT}/\Omega_{ce}\mathbf{e}_y$ is the drift velocity produced by the effective gravity g_{eT} and $\hat{\mathbf{V}}_{eT} = -ik_y c\hat{\phi}/B\,\mathbf{e}_x$ is the $\hat{\mathbf{E}} \times \mathbf{B}$ drift. In the heuristic model, the prescription $dn_{eT}/dx = (n_{eT}/n)dn/dx$ is followed and the trapped electron density fluctuation is given by

$$\frac{\hat{n}_{eT}}{n_{eT}} = \frac{\omega_{*e}}{\omega - \omega_{De}} \frac{e\hat{\phi}}{T_e} \,, \tag{3.5}$$

where $\omega_{De} = -(T_e/T_i)\omega_{Di} \sim k_y c T_e/(eBR_o)$ is the curvature drift for the trapped electrons and $\omega_{*e} = (-k_y c T_e/eB)(d\ln n/dx)$. While the trapped electrons are described by a "longitudinally cold" anisotropic distribution, the circulating electrons can be described by an isotropic distribution with density $n_C = n - n_T$ and temperature T_e such that $\omega < v_{the} k_{\|}$. Examining the longitudinal momentum conservation equation for the circulating electrons results in the "adiabatic" response

$$\frac{\hat{n}_{eC}}{n_{eC}} = \frac{e\hat{\phi}}{T_e} \,. \tag{3.6}$$

The dispersion relation is obtained from the quasineutrality condition $\hat{n}_i \approx \hat{n}_{eC} + \hat{n}_{eT}$ resulting in

$$\left(1 - \Gamma_o + \frac{n_{eC}}{n}\frac{T_i}{T_e}\right) - \frac{\omega_{*i}}{\omega}\left(\frac{n_{eT}}{n} - \Gamma_o\right) - \frac{\omega_{*i}}{\omega^2}\left(\omega_{De}\frac{n_{eT}}{n} - \omega_{Di}\Gamma_o\right) = 0 \,, \tag{3.7}$$

where $\Gamma_o \equiv I_o(b_i)exp(-b_i)$. There are a number of important limits of Eq. (3.7) to consider.

1. The limit $\Gamma_o \ll n_{eT}/n$ corresponding to $b_i > (n/n_{eT})^2/(2\pi)$ results in a mode

in the direction of the ion diamagnetic velocity

$$\omega \approx \omega_{*i} \frac{n_{eT}}{n} \frac{T_e}{T_e + T_i} , \tag{3.8}$$

with a frequency proportional to the concentration of trapped electrons.

2. When the contribution from trapped electrons n_{eT}/n can be neglected, the phase velocity of the mode is in the electron diamagnetic direction. For small values of n_{eT}/n, this mode can extend to rather large values of b_i with frequency $\omega \approx \omega_{*e}/(2\pi b_i)^{1/2}$. In the limit $b_i \ll 1$ corresponding to $\Gamma_o \approx 1$, the ordinary electron drift wave $\omega \approx \omega_{*e}$ is recovered. Wave-particle resonance contributions which were omitted in this simple derivation give rise to an instability when included. It is important to note that this resonant instability is stabilized by the influence of significant electron temperature gradients $\eta_e \equiv (d \ln T_e/dx)/(d \ln n/dx)$. The electron drift mode can also become unstable, in the presence of substantial electron collisionality [46]. This is commonly referred to as the "collisional" trapped electron instability. This mode is not a good candidate to explain anomalous energy transport for experiments in the multi-keV range, since the collisionality in these regimes is insufficient to allow the instability to occur.

3. The most interesting case is the transitional regime where $b_i \gtrsim 1$. In this case, a cancellation can occur in the middle term of Eq. (3.7) when $n_{eT}/n \approx \Gamma_o$ resulting in

$$\omega^2 \approx -\omega_{*i}\omega_{Di} \frac{n_{eT}}{n} \frac{1 + \frac{T_e}{T_i}}{1 + \frac{T_i}{T_e}} . \tag{3.9}$$

This gives a purely growing fluid-like instability with growth rate of order $\gamma \approx (\omega_{*i}\omega_{Di} n_{eT}/n)^{1/2}$. The mode is characterized as fluid-like since it does not depend on resonances with small regions of velocity space. The instability is driven by the magnetic curvature drift of the ions and trapped electrons in the region of unfavorable magnetic curvature and exists even in the absence of temperature gradients. The basic mechanism is similar to a gravitational interchange mode with the the effective gravity coming from the unfavorable

curvature of the magnetic field in the outer region of the torus.

For cases 1 and 2, the imaginary part of the frequency is determined by wave-particle resonance contributions which were omitted in this simple derivation. As pointed out in case 2, the collisional trapped electron mode depends on significant collisionality for the instability to occur and the resonant mode is stabilized by significant electron temperature gradients. The fluid-like regime in case 3 does not depend on a wave-particle resonance or collisional effects to occur and the growth rate in this regime is generally larger than when the instability depends on a resonance. In addition, the resonant instabilities are generally not as robust since they may saturate quickly by scattering the relatively few resonant particles. In contrast, fluid-like instabilities involve all the particles and a small adjustment to a portion of the distribution cannot stabilize the mode. Thus, the onset of the fluid-like instability is expected to be the most relevant in effecting the particle and energy transport processes across the magnetic flux surfaces.

Various other effects including collisions, electron temperature gradients, and higher order bounce resonances were examined in the original paper on the ubiquitous mode [37]. An extremely detailed development of the various results obtained for the collisional, resonant and fluid-like regimes is given in a subsequent publication [44] . It is important to note that the growth rate of the fluid-like instability is not sharply suppressed by the weak collisionality present in multi-keV plasmas.

The heuristic model outlined in this chapter is backed up by detailed calculations in toroidal geometry [44] including the effects of magnetic shear. The calculation is performed in the limit of large aspect ratio $1/\epsilon_o \equiv R_o/r \gg 1$ and the magnetic field is approximated by

$$\mathbf{B} = \frac{B_o \mathbf{e}_\zeta + B_\theta(r)\mathbf{e}_\theta}{1 + \frac{r}{R_o} cos(\theta)} , \tag{3.10}$$

where ζ and θ are the toroidal and poloidal angular coordinates. For large aspect ratio, the length along a field line is given by $L \approx 2\pi R_o q$ where $q \approx r B_\zeta / R_o B_\theta$. The modulation of $\mathbf{B}$ along a field line is related to $\Delta B/B \approx 2\epsilon_o$. The modes are localized around a rational surface $r = r_o$ such that $q_o \equiv q(r_o) = m^o/n^o$ where m^o and n^o are

integers. The appropriate eigenfunction is of the form

$$\tilde{\phi} = \tilde{\varphi}_m(\theta)\, \psi(r - r_o)\, exp\left\{-i\omega t + in^o\left[\zeta - q(r)\theta\right] + iS(r)F(\theta)\right\}\ , \tag{3.11}$$

where $\tilde{\varphi}_m(\theta)$ is periodic in θ with period 2π, $\psi(r-r_o)$ describes the radial localization, $S(r) \equiv n^o[q(r) - q_o]$ and the function $F(\theta)$ is monotonic in θ such that

$$F(\theta) = \int_0^\theta G(\theta')d\theta'\ , \tag{3.12}$$

where $G(\theta)$ is periodic and even around $\theta = 0$. In this calculation, the function $G(\theta)$ was taken to be $G(\theta) \approx 2\pi\delta(\theta \pm \pi)$ resulting in a step function for $F(\theta)$ with the step at $\theta = \pm\pi$. This form for $G(\theta)$ and $F(\theta)$ is valid for eigenfunctions which rapidly goto zero at $\theta = \pm\pi$. The function $\tilde{\varphi}_m$ gives the modulation of the mode amplitude along a field line and and can be of either even or odd parity about $\theta = 0$. The even parity mode was considered in the original analysis [37] with maximum $\tilde{\varphi}_m$ at $\theta = 0$. The radial localization of mode is described by $\psi(r - r_o)$. The modes are localized over a distance $\Delta r < r_o$ which is related to the scale lengths in the density and temperature. The case of odd $\tilde{\varphi}_m$ was considered in later papers by Coppi and Pegoraro [47, 38].

3.3 Ion Temperature Gradients

In this section, ion temperature gradient terms are included in the analysis and it is shown that for realistic gradients the even parity mode is unstable for a broader range of transverse wavelengths. In addition, it is pointed out that for the odd parity modes a similar cancellation can give rise to a fluid-like instability when the ion-temperature gradient exceeds a critical value.

In the presence of temperature gradients, the ion density perturbation is given by [38]

$$\frac{\hat{n}_i}{n} = -\frac{e\hat{\phi}}{T_i}\left\{1 - \Gamma_o + \frac{\omega_{*i}}{\omega}\Gamma_o\left[1 - \eta_i b_i\left(1 - \frac{I_1}{I_o}\right)\right] + \frac{\omega_{*i}\omega_{Di}}{\omega^2}\Gamma_o N(\eta_i, b_i)\right\}\ , \tag{3.13}$$

where

$$\eta_i \equiv \frac{1}{T_i}\frac{dT_i}{dx} \Big/ \frac{1}{n}\frac{dn}{dx} \,, \tag{3.14}$$

and $N(\eta_i, b_i)$ is a function of η_i, b_i and the geometry employed. Combining Eq. (3.13) with the quasineutrality condition $\hat{n}_{eC} + \hat{n}_{eT} = \hat{n}_i$ and Eqns. (3.5)-(3.6) results in the dispersion relation

$$\begin{aligned} \omega^2 \left[\frac{n_{ec}}{n} + \frac{T_e}{T_i}(1-\Gamma_o)\right] + \omega\omega_{*e}\left[\frac{n_{eT}}{n} - \Gamma_o\left(1-\eta_i b_i\left(1-\frac{I_1}{I_o}\right)\right)\right] \\ + \omega_{De}\omega_{*e}\left[\frac{n_{eT}}{n} + \frac{T_i}{T_e}\Gamma_o N(\eta_i, b_i)\right] = 0 \,. \end{aligned} \tag{3.15}$$

For the even parity modes, the cancellation of the middle term in Eq. (3.15) involves both trapped electrons and the ion temperature gradient. Thus when $\eta_i > 1$, the fluid-like instability can exist for longer transverse wavelengths $b_i < 1$. In the case of odd mode amplitude, the average over a trapped particle orbit of the mode potential is zero so that the trapped electrons do not contribute to the instability. Even without the effects of trapped electrons, the same type of cancellation can occur for the odd modes when $\eta_i b_i (1 - I_1/I_o) \approx 1$ resulting in a fluid-like instability. This corresponds to a critical value of $\eta_i \approx 1.7$. This regime is often referred to as the the toroidal ion-temperature gradient instability but is really just the odd parity ubiquitous mode. The curvature drift of the ions in the region of unfavorable magnetic curvature plays a central role in driving the instability.

3.4 Transport

As mentioned previously, the fluid-like instabilities are the most relevant for the diffusion of particles and energy across the magnetic field since the growth rates are larger than those obtained by considering wave-particle resonance contributions and the fluid-like instabilities involve all the particles so that a small adjustment to a portion of the distribution cannot stabilize the mode. A mixing length type argument

for the anomalous diffusion coefficient gives

$$D \approx \frac{\gamma}{k_\perp^2} , \tag{3.16}$$

where D is the relevant diffusion coefficient and $k_\perp$ is the transverse wavelength. Assuming a growth rate from the fluid-like instability of $\gamma \sim (\omega_{*i}\omega_{Di})^{1/2}$ with transverse wavelengths such that $b_i \sim 1$ gives a diffusion coefficient of order

$$D \sim D_B \frac{\rho_i}{(R_o a)^{1/2}} , \tag{3.17}$$

where $D_B = cT/eB$ is a Bohm diffusion coefficient and R_o and a are the major and minor radius. This general form for D is sometimes referred to as gyro-Bohm and is roughly consistent with the order of magnitude of the transport observed in many experiments. However, the ubiquitous modes are localized in the region of maximum pressure gradient, thus the resulting diffusion coefficient would be maximum in this region. This is inconsistent with the diffusion coefficient inferred from the experimental profiles, which is a monotonically increasing function. In addition, the results in this thesis indicate that the energy confinement time scales in a different manner with the plasma parameters than implied by Eq. (3.17) (see page 99 in Chapter 3). Thus, it appears difficult to explain the energy transport out of the plasma based only on the collective modes in the core of the plasma column. One obvious way around this dilemma is to hypothesize an additional set of collective modes localized in the edge region which can account for the observed transport [48]. Modes driven by a gradient in an impurity population [49, 50] are one possible example. It is not hard to imagine that the modes localized at the edge might be coupled to the modes occurring in the core region of the plasma column. This general viewpoint along with the observation that the normalized temperature profiles seem to vary weakly has led to the suggestion that a type of self-organization process might be at work [51]. This observation of "profile consistency" [51] is a key element of the diffusion coefficient developed in Chapter 4. It is important to note that while the principle of "profile-consistency" seems to hold up rather well in a wide range of experiments, a detailed proof starting

from the basic equations does not yet exist. Thus, the approach taken in Chapter 4 is to accept the principle as a starting assumption. Although the resulting coefficient is inspired by properties of the ubiquitous modes, the actual processes responsible for the transport are considerably more complicated than any single instability.

As mentioned previously, quasilinear calculations indicate that the electron thermal energy flux is up to an order of magnitude larger than the the corresponding particle flux for realistic values of η_i [39, 40], a feature that is consistent with experimental observations that the particle confinement time is significantly longer than the energy confinement time.

Chapter 4

Thermal Transport in Well Confined High Temperature Plasmas

4.1 Introduction

A fundamental issue in high temperature plasma physics is understanding transport phenomena. It has been known for many years that transport of energy, momentum and particles across magnetic flux surfaces in laboratory plasma is anomalously large in comparison to classical theoretical predictions based on binary collisions. Neoclassical theory, which includes the effects of magnetic geometry in the collisional theory [36], is also far to small to explain the observed confinement. Theoretical efforts to explain the anomalously large transport has focused primarily on turbulence generated by small scale instabilities in the plasma. Indeed, a substantial fraction of research in plasma physics is devoted to better understanding the multitude of plasma instabilities.

Although conclusive experimental evidence remains elusive, in recent years a consensus has formed that the most promising candidate to explain the anomalous transport in the core region of tokamak plasmas are modes driven by gradients in the ion

and electron temperature gradients [37, 38]. These modes are not appropriate in the edge region of a tokamak and additional edge instabilities must be considered to account for the observed confinement. Instabilities driven by a density gradient in an impurity population [49, 50] are among the possible candidates to account for the turbulence in this region. Thus energy transport in a tokamak is very complex involving collective modes in the core of the plasma column coupled to a different set of instabilities in the edge region. The physics in the core, where the mean free path for collisions is large in comparison to macroscopic length scale, is drastically different than the physics in the edge region where the mean free path can be small and where atomic processes, impurities and coupling of the plasma to a neutral population can further complicate the problem. A true "first principles" approach to transport must include the essential physics in both these regions. In recent years, initial steps toward a "first principles" approach have been undertaken based on extensive numerical simulations of ion temperature gradient driven turbulence [52, 53]. A model derived solely from these simulations without any free parameters is reported to successfully reproduce temperature profiles in a number of discharges from TFTR [53]. A weakness in this model is that the edge region is completely neglected by setting a boundary condition for the temperature at $r/a \approx 0.8$. Recent attempts to simulate the temperature profiles in Alcator C-Mod with this model have failed [54]. Realistically, predictive simulations of turbulent phenomena remains an elusive goal even for ordinary fluids and high temperature plasmas are arguably more complicated, thus the goal of a true "first principles" calculation is probably many years away.

A relatively simple model for tokamak confinement is highly desirable both as a predictive tool and for better understanding the plasma behavior. One important observation in constructing such a model is the idea of "profile consistency" [51]. There is no commonly agreed precise definition of profile consistency but in general it means that the normalized temperature profiles are approximately the same for various operating conditions and in particular when the auxiliary heating power is increased. The concept of profile consistency was originally inferred from analyses of ohmicly heated plasmas [51] where the profiles of the current, electron temperature

and ohmic heating are coupled through Ohm's law. It is somewhat remarkable that the principle seems to hold up rather well for auxiliary heated plasmas. Although the heating profile can vary drastically in a tokamak, the temperature profile is usually of a well defined canonical form. This principle has been observed in a number of machines where the response of the temperature to the heating deposition profile is examined. Rather dramatic evidence for this idea comes from observations in the DIII-D tokamak [55, 56] where electron cyclotron heating provides a means of accurately controlling the power deposition profile. A series of experiments were conducted where up to 80% of the total input power was deposited significantly off axis ($r/a > 0.5$). Even in these extreme cases, the temperature profile remains strongly peaked on axis and monotonically decreasing. Similar results with strong off axis electron cyclotron heating were also observed in the T-10 tokamak [57].

In certain experiments, the observed profile consistency calls into question a basic assumption of local transport analysis. Normally in the presence of turbulence it is assumed that the time evolution of the temperature of each species in the plasma is governed by a diffusion equation of the form

$$\frac{3}{2}\frac{\partial}{\partial t}(nT) + \nabla \cdot \vec{q} = Q \,, \tag{4.1}$$

where $\vec{q}$ is the heat flux and Q contains heat sources and sinks. The heat flux is normally assumed to be proportional to the temperature gradient $\vec{q} = -nD^{th}\nabla T$ where nD^{th} is the thermal conductivity. In the presence of turbulence, the thermal conductivity is not a material property of the plasma but instead is a convenient way of modeling the effect of small scale instabilities on the transport of thermal energy. Thus D^{th} may be related to T, ∇T or other quantities of importance to the underlying instability. The assumption that energy transport can be described by a diffusive model for the heat flux is called into question by a number of experiments with strong off axis heating. The heat flux can be inferred in a plasma by carefully measuring the temperature, heating, and radiation profiles. As mentioned previously, for experiments with the DIII-D and T-10 machines [55, 56, 57], even with strong off

axis heating the temperature profiles remain strongly peaked. The inferred heat flux for these plasmas is inward for the central portion of the plasma column. Thus it appears that in certain experiments heat actually flows up the temperature gradient which is clearly inconsistent with a simple diffusive model for the heat flux.

For most machines, such extreme off axis heating has not been examined. Nevertheless, there is evidence from a number of experiments that a simple diffusive heat flux is not the best model to describe the observations. Callen and Cordey have proposed that plasmas produced by the JET machine are better described by a heat flux of the form

$$\vec{q} = -nD^{th}\nabla T - \vec{q}_p \,, \tag{4.2}$$

where $\vec{q}_p$ is a constant heat pinch [58, 59]. A series of ohmic as well as neutral beam and ICRF heated discharges where considered. The overall heat flux is always outward, since the proposed heat pinch term is smaller than the outward diffusive heat flow. Ohmic and neutral beam heated discharges in JT60, have also been analyzed on the basis of the heat pinch model proposed by Callen and Cordey [60] and a heat pinch term proportional to $n_e B_p$ was found to be consistent with the experiment.

It is important to note the heat pinch term does not necessarily correspond to a net inward flow of particles. It may also be a way to characterize a process which results in a reduction of the outward transport of energy in some region of the plasma. Assuming the concept of a heat pinch is applicable over some range of parameters, there are several possible origins. It is interesting to note that neoclassical transport theory [36] predicts both particle and heat pinches, but in comparison to experiment they are too small by a factor of 100. The more likely explanation lies in one of the following:

1. *Side effect of a collective mode* - Inhomogeneities in temperature, density, and velocity are potential driving factors for small scale instabilities. The primary effect of many of these small scale instabilities is to produce an anomalous flux in the direction which tends to flatten the profile of the quantity driving the instability. This is the motivation for modeling the anomalous transport with a

diffusion equation. However, complete calculations of the total heat or particle fluxes often yield additional terms that produce a non-diffusive flow of particles or energy. This type of explanation is often invoked to explain the observed density profiles in tokamak plasmas [61, 62, 63] and might also have relevance to energy transport [64]. Details of this are discussed in Sec. 4.2.

2. *Part of a self organization process* - The principle of profile consistency is generally excepted to have validity in a large range of experiments, yet a detailed theoretical argument for its origin remains elusive. It has been suggested that a self organization process is at work which manages to produce the appropriate heat flux to maintain the actual profile close to some canonical profile. An idea closely related to this was proposed for plasmas in which the diffusion of longitudinal current and electron thermal energy are coupled through a diffusion matrix [65]. By considering the symmetry properties of this matrix, it is shown that inward fluxes of energy may arise. The details of this analysis are presented in Sec. 4.2

3. *Critical Gradient Model* - A number of proposed anomalous transport models are based on the degree to which the temperature (or some other quantity) exceeds a critical gradient [66, 52]. In these models, the heat flux is assumed to be of the form

$$\vec{q} = -nD^{th} \left(\nabla T - \nabla T_c\right) H \left(\nabla T - \nabla T_c\right) \ , \tag{4.3}$$

where ∇T_c is a critical or threshold temperature gradient. This critical gradient is a function of the other equilibrium parameters. The drive for the underlying instability is $\nabla T - \nabla T_c$, thus $H\left(\nabla T - \nabla T_c\right)$ is a unit step function and below the critical gradient the anomalous transport is zero. It is clear that for $\nabla T > \nabla T_c$ this is identical to a heat pinch model with $\vec{q}_p = +nD^{th}\nabla T_c$.

In any given experiment, distinguishing between the above processes is difficult. Indeed, it is entirely possible that some combination of these processes is at work. A common idea extending between them is that energy transport in a tokamak is

the result of multiple phenomena : a predominant diffusive process which produces the outward transport of energy and a competing process which tends to reduce the outward transport. Assuming such a description is valid, one might expect that these distinct processes scale in different ways with the various equilibrium parameters. Therefore, one could also expect the global scalings for confinement parameters such as the stored energy to reflect this underlying picture.

In this analysis, evidence is presented that energy confinement in tokamak plasmas is the result of two competing processes. A primary piece of evidence, comes from examining the scalings for confinement parameters such as β_p or stored energy. Motivation for this analysis originated from observations of ohmic and ICRF heated discharges in Alcator C-Mod [67]. Here it is shown that the experimental results from a wide range of parameters and in a number of different experiments are well described by a functional form involving the sum of two terms, one which is related to the standard diffusive outflow while the other is related to a process which tends to reduce this outflow. We term the scaling resulting from this analysis as a "composite" scaling and show that it is considerably better at describing the experiment than standard power law regressions. Several other researchers have considered scalings of this general type for the stored energy [58, 68, 69], but only for individual experiments and without regard to proper dimensionless parameters.

Another important result of this analysis is a thermal transport coefficient which is closely related to the composite scaling. The transport coefficient is consistent with the principle of profile consistency and is inspired by the properties of the modes thought to be responsible for the underlying transport. The resulting transport coefficient also involves the difference of two terms. One term represents the normal outward diffusion of thermal energy while the other term corresponds to a process which reduces the outward flux. Further evidence for the validity of this model comes from a series of transport simulations in which it is shown that the diffusion coefficient developed in this analysis can reproduce the observed temperature profiles for a range of plasmas produced by the Alcator C-Mod machine.

The theoretical background and possible origins of a composite scaling are dis-

cussed in Sec. 4.2. The analysis which led to the initial composite scaling for Alcator C-Mod and the subsequent extension to other machines is presented in Sec. 4.3, A detailed comparison between the scaling developed in this analysis and the experimental database assembled for the ITER project is given in Sec. 4.3 and in Appendix C. Comparisons between a well-known power law regression and the composite scaling developed in this analysis are made in Sec. 4.4. A transport coefficient consistent with the composite scaling is developed for generalized geometry in Sec. 4.5. This coefficient was implemented in a transport code and used to examine a series of ohmic and ICRF discharges produced by the Alcator C-Mod machine. The simulations are discussed in Sec. 4.6 and detailed comparisons between the simulated and experimentally measured temperature profiles are given in Appendix A for ohmic discharges and Appendix B for ICRF discharges. The sensitivity of this model to the boundary condition at the edge is examined in Sec. 4.6.4. Based on the composite scaling developed in this analysis, an extrapolation is made in Sec. 4.7 for the expected confinement of two proposed ignition experiments. An alternative diffusion coefficient along with a non-diffusive heat pinch term is discussed in Sec. 4.8. A possible extension of this model to H-mode discharges is given in Sec. 4.9 and a comparison of this extension with several machines is presented in Appendix D. Finally in Sec. 4.10, a summary of the important results is given along with conclusions concerning the relevance of this analysis.

4.2 Theoretical Considerations

In a weakly collisional magnetically confined plasma, it is possible for certain processes to transport energy or particles in the direction of the gradient, contrary to the "normal" diffusion process. The inward flux may be convective (i.e. a true "inflow") or may be due to an off-diagonal term in a more general transport matrix.

An example of a convective "inflow" is the well-know particle pinch [61, 62] introduced to described particle transport in well confined plasmas. In this example, the

particle flux is written as

$$\Gamma_p = -D_p \frac{dn}{dr} - V_{in}^p n \frac{r}{a} \tag{4.4}$$

where D_p is the particle diffusion coefficient and V_{in}^p is the inflow velocity. The explanation given [61] for the inflow is the excitation of ion-mixing modes at the edge of the plasma column. A primary effect of these modes is an outward transport of the ion thermal energy but an important side effect is an inward transport of particles.

It was recently proposed that the observation of a transport barrier for the ion thermal energy [70] might be attributed to an off-diagonal term in a transport matrix which gives rise to an inward flux of thermal energy [64] and is attributed to the excitation of a mode driven by the shear in the toroidal plasma flow velocity. While the primary effect of this mode is an outward transport of angular momentum, it is shown that a secondary effect is an inflow of thermal energy. According to this explanation, the thermal inflow is driven by a gradient in the velocity.

In contrast to both of these examples where a specific well localized mode gives rise to an inward transport process, it has been proposed that a self organization process might also produce an inward flux of thermal energy. Coppi and Pegoraro consider the regimes in which the anomalous transport of the electron thermal energy and the longitudinal current density are coupled [65] and can be described by a diffusion matrix

$$-\nabla \cdot \left[\mathbf{D} \cdot \nabla \begin{vmatrix} T_e \\ J_{||} \end{vmatrix} \right] = \begin{vmatrix} S_1 \\ S_2 \end{vmatrix} , \tag{4.5}$$

where S_1 is the effective entropy production rate ($S_1 > 0$), $S_2 = E_{||} - \eta J_{||}$ is the difference between the electric field and the "resistive field" and $\mathbf{D}$ is a transport matrix

$$\mathbf{D} = \begin{vmatrix} D_{11} & D_{12} \\ D_{21} & D_{22} \end{vmatrix} . \tag{4.6}$$

The transport matrix $\mathbf{D}$ is assumed to be positive definite and symmetric (Onsager-type symmetry)

$$D_{21} = D_{12} \qquad D_{11} > 0 \qquad D_{22} > 0 \qquad D_{11}D_{22} - D_{12}^2 > 0 \, . \tag{4.7}$$

Underlying this proposed diffusion matrix is the assumption that collective modes involving the combined gradients of electron temperature and longitudinal current density are responsible for the diffusion of current and thermal energy. These might take the form of non-normal modes and be difficult to identify experimentally.

By considering the symmetry of the proposed diffusion matrix, Coppi and Pegoraro derive an expression for the current density

$$J_{\|} = \sigma_{\|} \left\{ E_{\|} + \nabla \cdot \left[\mathcal{L}_e \left(\nabla_r J_{\|} - c_o \frac{J_{\|}}{T_e} \nabla_r T_e \right) \right] \right\} , \tag{4.8}$$

and for the heat flux

$$q_r^e = - \left[\kappa_e + c_o(c_o - 1) \mathcal{L}_e \frac{J_{\|}^2}{T_e} \right] \nabla_r T_e + \left[\mathcal{L}_e (c_o - 1) J_{\|} \right] \nabla_r J_{\|} . \tag{4.9}$$

The effective thermal conductivity is given by

$$\kappa_e \equiv T_e D_{11} - c_o^2 \frac{J_{\|}^2}{T_e} \mathcal{L}_e > 0 , \tag{4.10}$$

where $\mathcal{L}_e \equiv D_{22}$ is the thermal viscous coefficient and

$$c_o = \left(\frac{1}{J_{\|}} \frac{dJ_{\|}}{dr} \Big/ \frac{1}{T_e} \frac{dT_e}{dr} \right) . \tag{4.11}$$

Since the observed gradient in the current is normally steeper than the the temperature gradient, it is clear that $c_o > 1$. The effective electron thermal conductivity in Eq. (4.10) is the difference of two terms with the second term involving $\mathcal{L}_e$ reducing the outward transport. This general idea is consistent with the electron thermal diffusion coefficient developed in Sec. (4.5) which also involves the difference of two terms and for which the second term is also related to a process which reduces the outward flux of energy.

It is interesting to note an analogy between Equations (4.8)-(4.9) and the classical

thermoelectric equations for an isotropic conducting solid [71],

$$\vec{J} = \sigma\left(\vec{E} - S\nabla T\right) , \tag{4.12}$$

$$\vec{q} = \sigma T S\vec{E} - \kappa\nabla T , \tag{4.13}$$

where S is the Seebeck Coefficient (average entropy/charge carrier $\times$ electron charge), σ is the electrical conductivity and κ is the thermal conductivity. Combining to eliminate $\vec{E}$

$$\vec{q} = \left(\sigma T S^2 - \kappa\right)\nabla T + TS\vec{J} , \tag{4.14}$$

gives an inward heat flux term related to the Seebeck Coefficient S.

4.3 New L-Mode Scaling

Typically when looking for transport scalings, researchers assume the functional form is well represented by a power law. Other functional forms for the transport scaling are also possible. If energy confinement is the result of multiple processes, one might expect that these processes scale in different ways with the various plasma parameters. While it is not claimed that the scaling presented here is unique, the theoretical arguments in Sec. 4.2 are supportive of an energy transport description composed of both the "normal" diffusive outflow as well as other processes which tend to reduce the outward flux of thermal energy.

In looking for new transport scalings, several guiding principles where followed. The first of these is that any scaling should relate relevant dimensionless quantities such as β_p in terms of other dimensionless quantities characterizing the experiment. Dimensional scalings for the stored energy or confinement time can be derived later from the dimensionless scaling. A second guiding principle is that relevant discharges should be carefully selected. A "universal" transport scaling covering all modes of operation and all parameter regimes almost certainly does not exist. It clearly does not make sense to look for scalings in the confinement characteristics for a group of

discharges when the underlying processes responsible for the transport are drastically different.

4.3.1 L-Mode Scaling for Alcator C-Mod

The proposed scaling was originally developed from observations of ohmic and ICRF heated discharges in Alcator C-Mod [67]. For ohmic discharges, it was observed that $\beta_p/q_E^{2/3}$ is roughly constant where $q_E = 2\pi a^2 \kappa B_T/(\mu_o I_p R)$. Drawing inspiration from this observation, a more general dimensionless relationship for auxiliary heated plasmas was developed in terms of the relevant dimensionless parameters. Since one expects β_p to increase with the heating power, a natural dimensionless parameter to consider is the ratio of the total heating power P_H to some characteristic power scale. An obvious choice for this is the product of the plasma current I_p and a characteristic voltage scale $\mathcal{V}_o$. For ohmic plasmas, the loop voltage is a reasonable choice for this scale since the ohmic loop voltage does not vary greatly between different discharges and between different machines. For auxiliary heated plasmas, the loop voltage can vary significantly and one must look for another appropriate voltage scale. One possible choice for this scale is in terms of a dimensionless parameter introduced originally in connection with the CMG diffusion coefficient for ohmic plasmas [72]

$$\mathcal{V}_o = \alpha_v \frac{T_e}{e} \left(\omega_{pi} \frac{c^2}{\omega_{pe}^2} \frac{\nu_e}{v_{the}^2} \right)^{2/5} , \tag{4.15}$$

where $\alpha_v \approx 0.18$ is a dimensionless constant chosen such that $\mathcal{V}_o \approx 1$ Volt for typical tokamak parameters. Notice that $\mathcal{V}_o \propto n^{1/5}$ is a weakly increasing function of density.

Examining data from Alcator C-Mod, it was found that the relationship between $\beta_p/q_E^{2/3}$ and $P_H/I_p\mathcal{V}_o$ is well represented by a linear function with an off-set

$$\frac{\beta_p}{q_E^{2/3}} \approx \gamma_1 \frac{P_H}{I_p \mathcal{V}_o} + \gamma_2 , \tag{4.16}$$

where γ_1 and γ_2 are numerical constants. The off-set portion of the scaling was rather

unexpected[1]. For ohmic plasmas, the two contributions to β_p are roughly equal.

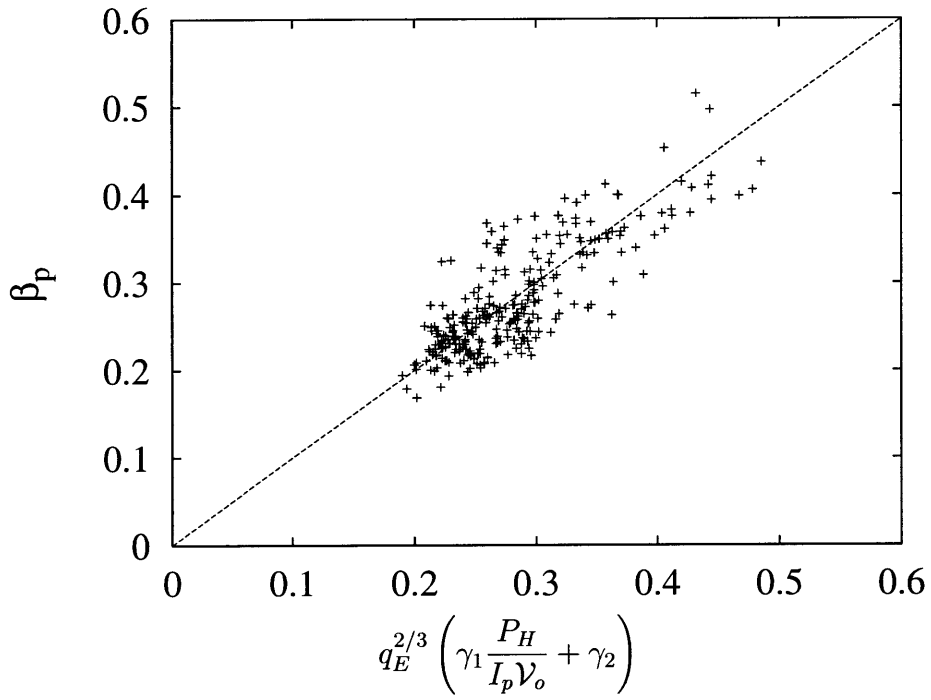

Figure 4-1: Dimensionless scaling for ohmic and ICRF heated discharges from Alcator C-Mod where $\mathcal{V}_o \approx 1$, $\gamma_1 \approx 0.054$, $\gamma_2 \approx 0.036$

4.3.2 Extension to Other Experiments

To extend this idea to other machines, a more general form was proposed [73]

$$\frac{\beta_p}{q_E^{2/3}} \approx f_1 \frac{P_H}{I_p \mathcal{V}_o^o} + f_2 \,, \tag{4.17}$$

where f_1 and f_2 are functions of other dimensionless parameters involving geometry and weaker dependences on other plasma parameters. For any particular machine, the functions f_1 and f_2 vary weakly. Thus, it is only possible to determine f_1 and f_2 from examining data from a range of machines.

[1]The off-set was pointed out by Steve Wolfe from the MIT Plasma Fusion Center after reviewing some of our initial scalings

Using the database assembled for the ITER project [74], possible forms for the functions f_1 and f_2 were identified. A primary purpose of transport scalings is to extrapolate the confinement characteristics of machines envisioned to operate at or near ignition conditions. Thus, relatively clean thermal plasmas close to equilibrium are the most relevant. Discharges from DIII-D, JET, JT60, PDX, TFTR, FTU, and Alcator C-mod were selected based on the following criteria

1. Ohmic or L-mode regimes
2. $Z_{eff} < 2.0$
3. $0.7 < W_i/W_e < 1.3$ where W_i is the ion stored energy and W_e is the electron stored energy (i.e. discharges where T_i and T_e are not drastically different)
4. $W_{th}/W_{Tot} > 0.70$ where W_{th} is the thermal stored energy and W_{Tot} includes the thermal and non-thermal contributions to the stored energy.
5. Close to equilibrium: $[dW/dt]/P_H < 0.1$

In performing the analysis, a weak density dependence was found which is convenient to group with the density dependence already present in Eq. (4.15) by defining a modified voltage scale

$$\mathcal{V}_o^o \approx \mathcal{V}_o \left[\frac{\nu_*}{1+\nu_*} + \left(\frac{n_o^o}{n} \right)^{1/3} \right] , \tag{4.18}$$

where $\nu_* = \nu_e q_E R/v_{the}(R/a)^{3/2}$ is the collisionality of the trapped electron population and n_o^o is a reference density. The ratio n_o^o/n should be related to a dimensionless function involving relevant plasma parameters. One possible choice is

$$\left(\frac{n_o^o}{n} \right)^{1/3} \equiv C_1 \left(\frac{\omega_{pi}}{\nu_e} \right)^{2/3} \left(\frac{c}{4\pi v_{the}} \right)^2 \frac{m_e}{m_p} , \tag{4.19}$$

with $C_1 \approx 0.24$ corresponding to $n_o^o \approx 0.7 \times 10^{20}$ m^{-3}. The characteristic voltage scale $\mathcal{V}_o^o$ decreases weakly with density when $\nu_* \ll 1$.

A power law scaling for f_1 and f_2 was identified in terms of dimensionless parameters involving geometry and other weakly varying quantities. As shown in Fig. 4-2, the selected discharges are well described by Eq. (4.17) using f_1 and f_2 of the form

$$\begin{aligned} f_1 &\approx 0.11 \left(\frac{d_i}{a}\right)^{1/2} A_i^{1/4} \left(\frac{\omega_{pe}}{\Omega_{ce}}\right)^{1/3} , \\ f_2 &\approx 0.15 \frac{R}{10a} A_i^{1/2} \left(\frac{\omega_{pe}}{\Omega_{ce}}\right)^{1/3} , \end{aligned} \tag{4.20}$$

where A_i is the average mass number and both $d_i \equiv c/\omega_{pi}$ and ω_{pe} are evaluated with the line average density.

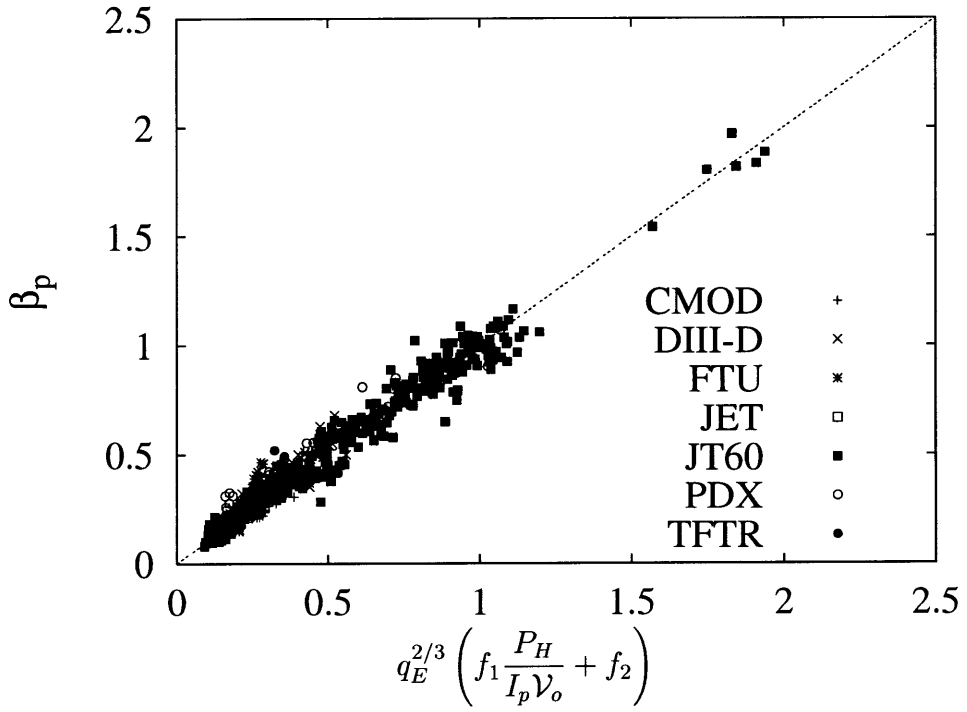

Figure 4-2: Comparison of β_p scaling in Eq. (4.17) with selected discharges from the ITER L-mode database

An important result of this work is that the confinement scaling for the stored energy is the sum of two terms. The scaling in Eq. (4.17) can be re-written in terms

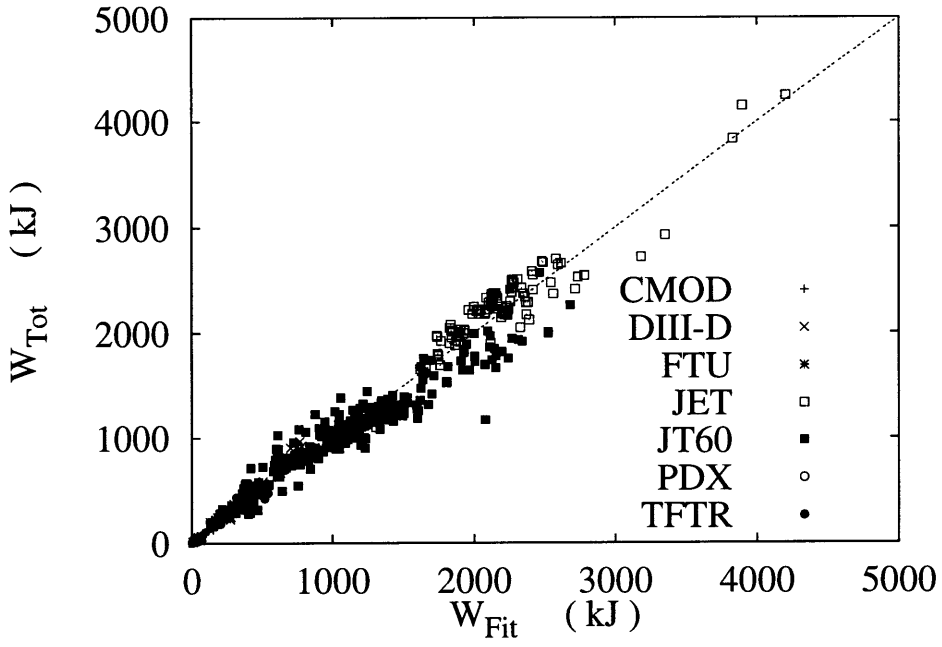

Figure 4-3: Comparison of W scaling in Eq. (4.22) with selected discharges from the ITER L-mode database

of the stored energy using the definitions

$$W = \frac{3}{2}\overline{p}V_a \qquad \beta_p = \frac{2\mu_o\overline{p}}{\langle B_p^2\rangle}\,, \tag{4.21}$$

where $p = n_eT_e + n_iT_i$, $\overline{p}$ is the volume average and V_a is the plasma volume. Approximating the surface averaged poloidal field by $\langle B_p\rangle \approx \mu_o I_p/\mathcal{L}$ where $\mathcal{L}$ is the poloidal length around the outermost flux surface, the scaling for the stored energy is

$$\begin{aligned} W &\approx 0.11\frac{3V_a\mu_o}{4\mathcal{L}^2\mathcal{V}_o}I_pq_E^{2/3}P_H\left(1+f_3\frac{I_p\mathcal{V}_o}{P_H}\right)\left(\frac{d_i}{a}\right)^{1/2}\left(\frac{\omega_{pe}}{\Omega_{ce}}\right)^{1/3}A_i^{1/4}\,, \\ f_3 &\approx 1.4\left(\frac{R}{5a}\right)^{1/2}\left(\frac{R}{20d_i}\right)^{1/2}A_i^{1/4}\,. \end{aligned} \tag{4.22}$$

A comparison between Eq. (4.22) and the selected discharges is shown in Fig. 4-3. Detailed comparisons for each of the machines considered in this analysis are given in Appendix C. The comparisons are generally quite favorable.

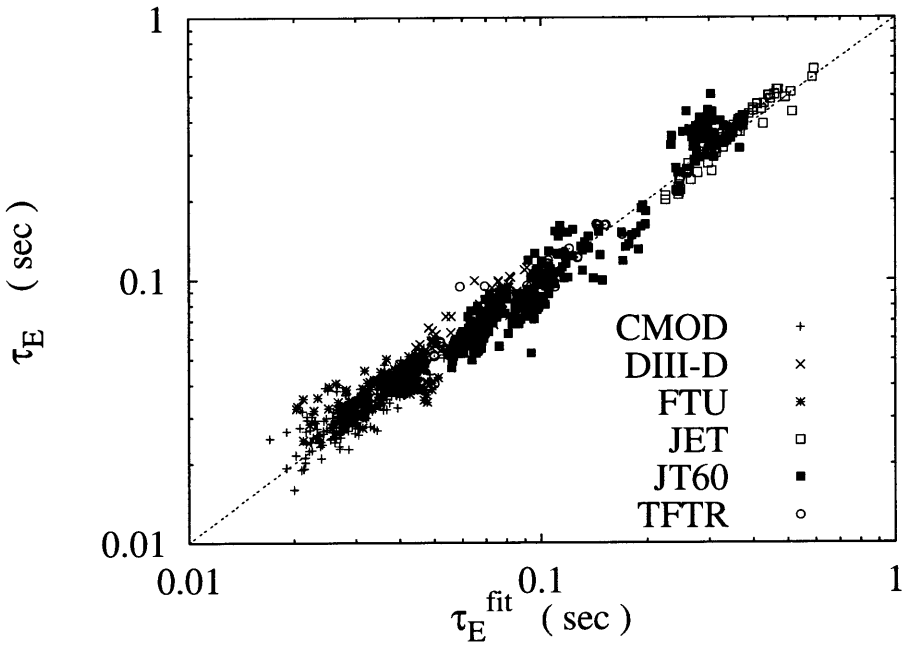

Figure 4-4: Comparison of τ_E scaling with selected discharges from the ITER L-mode database

Another confinement parameter of interest is the energy confinement time $\tau_E \equiv W/P_H$. Assuming the volume is approximately $V_a \approx 2\pi^2 a^2 R\kappa$ and $\mathcal{L} \approx 2\pi a\kappa^{1/2}$, a simplified scaling for the energy confinement time results

$$\tau_E \approx 0.031 R q_E^{2/3} I_p \left(1 + f_3 \frac{I_p \mathcal{V}_o}{P_H}\right) \left(\frac{d_i}{a}\right)^{1/2} \left(\frac{\omega_{pe}}{\Omega_{ce}}\right)^{1/3} A_i^{1/4} , \tag{4.23}$$

with R in meters, I_p in MA, P_H in MW and τ_E in seconds. Since corrections to V_a and $\mathcal{L}$ for a strongly shaped cross section can be significant, the actual τ_E scaling used in this analysis is given by Eq. (4.22) divided by P_H. This scaling for τ_E is compared with the selected discharges from the experimental database in Figure 4-4.

In Sec. 4.5, it is shown that for the thermal diffusion coefficient consistent with this scaling, the second term in Eq. (4.17) is related to a process which reduces the flux of energy. The degradation in confinement observed with increased heating power is attributed to the decreased importance of this term. In contrast with a typical L-mode power law scaling, this analysis indicates that the confinement time

will saturate for large heating power.

4.4 Comparison of Composite Scaling with Power Law Regressions

A common practice in the analysis of tokamak confinement is to perform a power law regression for the stored energy or energy confinement time in terms of the various independent variables which are thought to be of importance (I_p, P_H, $\overline{n}_e$, geometry, etc). For L-Mode discharges, the energy confinement time is typically found to increase with plasma current, decrease with total heating power and increase very weakly with plasma density. Since variations in major and minor radius are quite small for any single machine, the dependence on geometry must be determined by examining data from a range of machines. One of the most recent and widely cited L-mode scalings, know as the ITER89-P [75], was developed from the database assembled for the ITER project and is given by

$$\tau_E^{89} \approx 0.038 I_p^{0.85} R^{1.2} a^{0.3} \kappa^{0.5} \overline{n}_e^{0.1} B_T^{0.2} A_i^{0.5} P_H^{-0.5} \,, \tag{4.24}$$

with τ_E in seconds, I_p in MA, R and a in m, $\overline{n}_e$ in units of 10^{19} m^{-3}, B_T in T, and P_H in MW. A recent update to this scaling based on the same database used in this analysis is given by [74]

$$\tau_E^{96} \approx 0.037 I_p^{0.74} R^{1.69} (a/R)^{0.3} \kappa^{0.67} \overline{n}_e^{0.24} B_T^{0.2} A_i^{0.26} P_H^{-0.57} \,, \tag{4.25}$$

with the same system of units. This power law scaling resulted from an analysis [74] which considered all 14 machines in the transport database while our analysis was limited to 7 of these machines. For the analysis performed in this work, care was taken to select only clean thermal discharges close to equilibrium (see page 96 for selection criteria), thus only a subset of the discharges used to obtain the power law scaling in Eq. (4.25) were considered. However, a power law regression on this subset

Table 4.1: Comparison of RMS error for composite transport scaling of Eq. (4.22) with L-mode power law scaling Eq. (4.25)

Machine	Number of Discharges	RMS Error for Composite Scaling Eq. (4.23)	RMS Error for L-Mode Power Law Eq. (4.25)
Alcator C-Mod	348	11.6 %	28.1 %
DIII-D	72	15.4 %	26.1 %
FTU	138	15.7 %	31.3 %
JET	104	7.9 %	8.3 %
JT60	349	14.5 %	17.9 %
PDX	32	24.4 %	16.8 %
TFTR	45	11.4 %	20.4 %
All Machines	1088	**13.1 %**	**23.6 %**

gives a scaling which is only marginally different than Eq. (4.25). The machines not considered in our analysis had very few (if any) discharges that satisfied the selection criteria.

A comparison between these power law scalings and the composite scaling developed in this analysis was made in terms of the root mean square error (RMS). To be explicit, the RMS error used in the comparison is defined by

$$\text{RMS Error} = \left[\frac{1}{N_d} \sum_{1}^{N_d} \frac{(W_{scale} - W_{exp})^2}{W_{exp}^2} \right]^{1/2} , \tag{4.26}$$

where N_d is the number of discharges, W_{scale} is the stored energy predicted by a scaling and W_{exp} is the stored energy measured by experiment.

As shown in Table 4.1, the composite scaling developed in this analysis has an RMS error of 13% which is almost half the RMS error of the best available power law regression. For the comparison in Table 4.1, the recent update to the ITER89-P scaling in Eq. (4.25) is used since it has a lower RMS error for the selected discharges than the older more widely cited scaling in Eq. (4.24). Considered individually, the composite scaling has a lower RMS error for every machine with the exception of PDX. The stored energy for this machine is higher than the value predicted by the composite scaling. As show in Fig. C-12, this difference appears to be a uniform offset

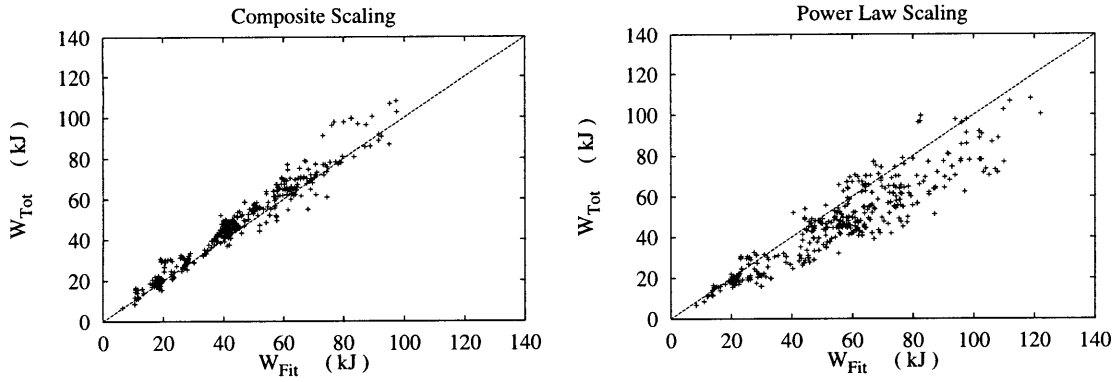

Figure 4-5: Comparison of composite and power law scalings for the stored energy of Alcator C-Mod discharges

suggesting that the composite form of Eq. (4.17) is correct but that the power series representation for f_1 and f_2 is not adequately determined.

The power law regression has the largest RMS error for Alcator C-Mod and FTU (approximately 30%) which are compact high field machines and substantially different in parameters than the other experiments. This comparison is quite striking in Fig. 4-5 where the power law regression and composite scaling for the stored energy are compared for discharges from the Alcator C-Mod machine.

4.5 Associated Diffusion Coefficient

In this section, a derivation is given in generalized geometry for a thermal diffusion coefficient [67] consistent with the transport scaling presented in Sec. 4.3.

Consider a toroidal geometry where ξ is the square root of the normalized toroidal flux and ϕ, θ are the toroidal and poloidal angles. We assume that the electron thermal conductivity is the main form of power loss and write the surface averaged electron energy equation as

$$\langle \nabla \cdot \vec{q}_e \rangle = \langle S_H \rangle, \tag{4.27}$$

where $\vec{q}_e$ is the heat flux and S_H is the heating power per unit volume. The surface

average is defined by

$$\langle A \rangle = \frac{1}{V'} \int A \sqrt{g} d\theta d\phi = \frac{d}{dV} \int_{vol} A \, dV, \tag{4.28}$$

where V is the volume within the flux surface labeled by ξ, $g \equiv |\nabla\xi \times \nabla\phi \cdot \nabla\theta|^{-1}$ is the Jacobian and

$$V' = \frac{\partial V}{\partial \xi} = \int \sqrt{g} d\theta d\phi. \tag{4.29}$$

The divergence theorem is used to write

$$\langle \nabla \cdot \vec{q}_e \rangle = \frac{d}{dV} \int_{vol} \nabla \cdot \vec{q}_e \, dV = \frac{d}{dV} \int \vec{q}_e \cdot \nabla\xi \sqrt{g} d\theta d\phi \, , \tag{4.30}$$

which simplifies Eq. (4.27) to

$$\frac{1}{V'} \frac{\partial}{\partial \xi} \left(V' \langle \vec{q}_e \cdot \nabla\xi \rangle \right) = \langle S_H \rangle. \tag{4.31}$$

Assuming that the electron thermal transport coefficient D_e^{th} is a function of the flux surface variable, the heat flux can be written as

$$\langle \vec{q}_e \cdot \nabla\xi \rangle = -n D_e^{th} \frac{\partial T_e}{\partial \xi} \langle |\nabla\xi|^2 \rangle. \tag{4.32}$$

Integrating from the magnetic axis to a given flux surface and solving for D_e^{th} gives,

$$D_e^{th} = -\frac{\mathcal{P}_H}{n \frac{\partial T_e}{\partial \xi} V' \langle |\nabla\xi|^2 \rangle} \, , \tag{4.33}$$

where

$$\mathcal{P}_H = \int_0^{\xi} V' \langle S_H \rangle d\xi, \tag{4.34}$$

is the heating power within a flux surface ξ. Although the heating profile can vary dramatically in a tokamak plasma, the resulting temperature profile is usually of a well defined canonical form. Thus it is assumed the temperature profile is represented

by

$$T_e = T_{e_0}\, exp\left(\frac{-\alpha(\xi)V(\xi)}{V_a}\right) \quad , \tag{4.35}$$

where T_{e_0} is a constant, V_a is the total plasma volume and α is a weak function of ξ to allow greater flexibility in the canonical form. Using Eq. (4.35) to calculate the temperature gradient, Eq. (4.33) becomes

$$D_e^{th} = \frac{1}{nT_e}\frac{V_a}{\langle|\nabla V|^2\rangle}\frac{\mathcal{P}_H}{\alpha} \, . \tag{4.36}$$

In order to derive a transport coefficient which is dependent only on the plasma parameters, it is desirable to relate the heating power to the local and global plasma parameters. Referring to the the dimensionless scaling in Eq. (4.17) we assume $\mathcal{P}_H/\alpha \propto I(\xi)$ where $I(\xi)$ is the plasma current within flux surface ξ and write

$$\frac{\mathcal{P}_H}{\alpha} \approx I(\xi)\mathcal{V}_o^o\frac{1}{f_1}\left(\frac{\beta_p}{q_E^{2/3}} - f_2\right) \, . \tag{4.37}$$

Substituting Eq. (4.37) into Eq. (4.36) gives a diffusion coefficient of the form

$$D_e^{th}(\xi) \approx \mathcal{V}_o^o\frac{I(\xi)}{n(\xi)T_e(\xi)}\frac{V_a}{\langle|\nabla V|^2\rangle}\left[\frac{\beta_p}{q_E^{2/3}} - f_2\right]\frac{1}{f_1} \, . \tag{4.38}$$

Motivated by the properties of the ubiquitous modes [37, 38] it is assumed that the underlying collective modes responsible for the energy transport are driven by the electron pressure gradient. Therefore, the β_p in Eq. (4.38) is replaced with the the parameter

$$\beta_{p*} = \frac{8\pi p_{e*}}{\langle B_\theta^2\rangle} \, , \qquad p_{e*} = \left|\frac{dp_e}{d\xi}\langle|\nabla\xi|\rangle\right|_{max} a, \tag{4.39}$$

where a is the half width of the flux surface with maximum $dp_e/d\xi$. The final form for the diffusion coefficient is

$$D_e^{th}(\xi) \approx \mathcal{V}_o^o\frac{I(\xi)}{n(\xi)T_e(\xi)}\frac{V_a}{\langle|\nabla V|^2\rangle}\mathcal{F}_D\frac{1}{A_i^{1/4}} \, , \tag{4.40}$$

where

$$\mathcal{F}_D \approx \begin{cases} C_2 \left(\frac{a}{d_i}\right)^{1/2} \left[C_3 \frac{10\beta_{p*}}{q_E^{2/3}} \left(\frac{\Omega_{ce}}{\omega_{pe}}\right)^{1/3} - \frac{R}{4a} A_i^{1/2}\right] & \text{if } C_3 \frac{10\beta_{p*}}{q_E^{2/3}} \left(\frac{\Omega_{ce}}{\omega_{pe}}\right)^{1/3} - \frac{R}{4a} A_i^{1/2} \gtrsim 0.25 \\ 0.25 C_2 \left(\frac{a}{d_i}\right)^{1/2} & \text{otherwise .} \end{cases} \tag{4.41}$$

Here $\mathcal{V}_o^o$ is given by Eq. (4.18) and $C_3 \approx 1.7$, $C_2\alpha_v \approx 0.015$ are dimensionless numerical coefficients. Note that in practice, there are only *two* numerical coefficients to be fitted since for nearly all discharges considered $\nu_* \ll 1$.

The function $\mathcal{F}_D$ contains two terms. The first corresponds to the standard diffusive outflow of thermal energy while the second represents a process which reduces this outward flux. For discharges with β_{p*} below the minimum criteria stated in Eq. (4.41), we take an alternate form for $\mathcal{F}_D$. The minimum criteria was obtained by selecting out ohmic discharges from a number of machines and assuming that the minimum transport corresponds to the typical level of ohmic confinement observed. For typical tokamak parameters, the minimum β_{p*} for this criteria is in the range $\beta_{p*} \sim 0.1 - 0.15$.

4.6 Transport Simulation

A series of numerical simulations for plasmas from Alcator C-Mod were carried out to test the diffusion coefficient presented in Sec. 4.5. The simulations were performed with the 1 $\frac{1}{2}$D transport code BALDUR [76]. As described below, this code computes the magnetic flux surfaces from a two-dimensional axi-symmetric MHD equilibrium and then solves one-dimensional diffusions equations across these flux surfaces.

4.6.1 Description of BALDUR Code

In order to describe the basic elements of the BALDUR code, consider the cylindrical coordinate system (R, ϕ, Z) shown in Fig. 4-6. The assumption of axisymmetry implies $\partial S/\partial\phi = 0$ for any scalar S.

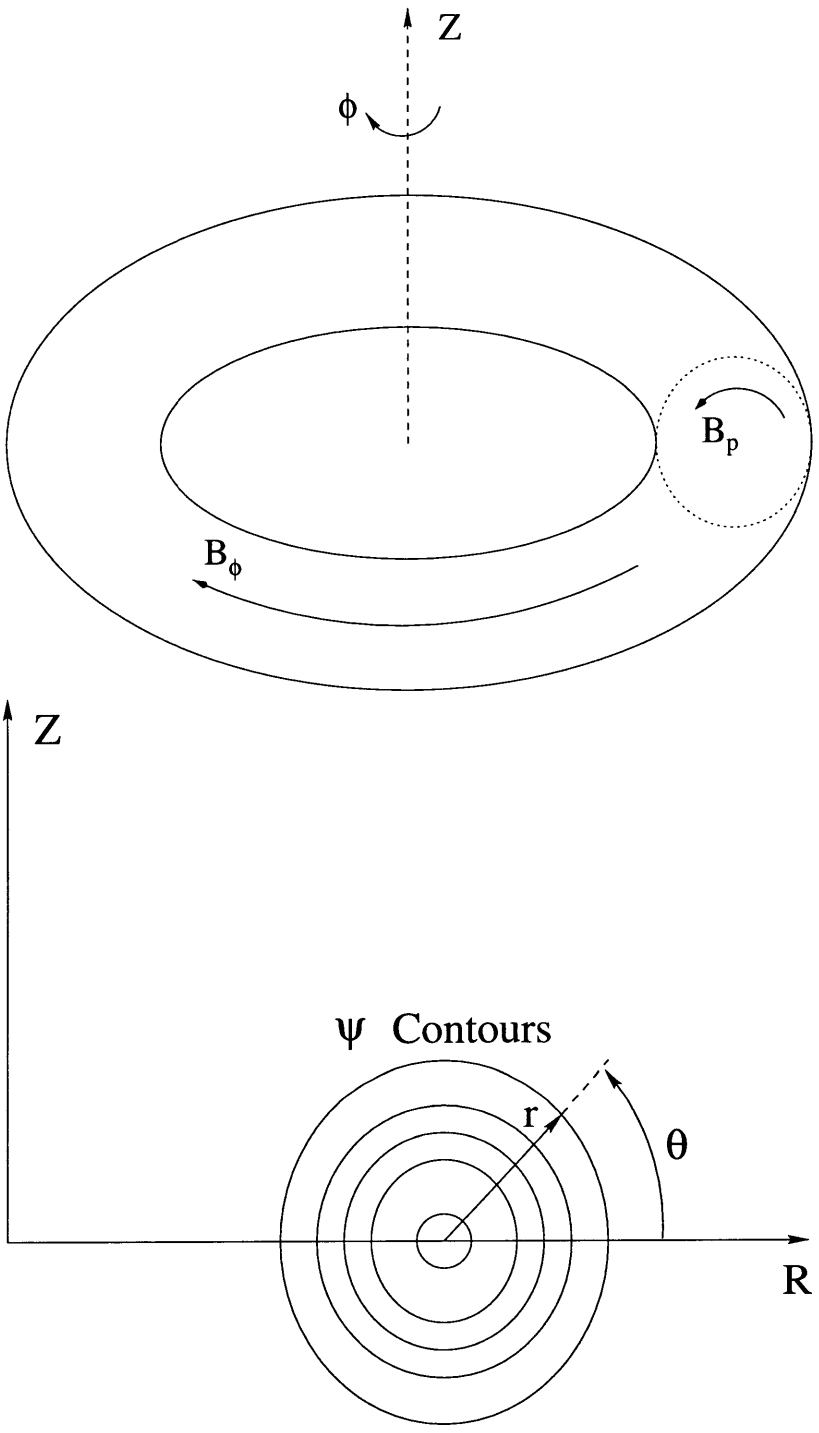

Figure 4-6: Geometry under consideration for BALDUR code

The ideal MHD equilibrium is given by the force balance

$$\nabla p = \mathbf{J} \times \mathbf{B} \,, \tag{4.42}$$

combined with Ampere's Law

$$\nabla \times \mathbf{B} = \mu_o \mathbf{J} \,. \tag{4.43}$$

It is convenient to express the magnetic field in toroidal and poloidal components $\mathbf{B} = B_\phi R\hat{\phi} + \mathbf{B}_p$ where

$$\mathbf{B}_p = \nabla\psi \times \hat{\phi} \,, \tag{4.44}$$

ψ is a stream function for the poloidal magnetic field and $\hat{\phi} = \nabla\phi = \mathbf{e}_\phi / R$. Combining Eq. (4.42) and (4.43) gives the Grad-Shafranov equation

$$R\frac{\partial}{\partial R}\left(\frac{1}{R}\frac{\partial\psi}{\partial R}\right) + \frac{\partial^2\psi}{\partial z^2} = -\mu_o R^2 \frac{dp}{d\psi} - F\frac{dF}{d\psi} \,, \tag{4.45}$$

where $F = RB_\phi$. Equation (4.45) describes the axisymmetric toroidal equilibria subject to the choice of two free functions $p(\psi)$ and $F(\psi)$. The function F is related to the poloidal current in the plasma and toroidal field coils. The equilibrium problem can be revised in terms of other variables but there remains two free functions. Specifying these free functions along with proper boundary conditions determines the magnetic geometry.

The magnetic field lines lie on magnetic flux surfaces which are defined by the surfaces of constant ψ (i.e. $B \cdot \nabla\psi = 0$). From Eq. (4.42), it is clear that the pressure is a surface quantity $p = p(\psi)$. Since the thermal conductivity is extremely large along a field line in comparison to the thermal conductivity across the field, it is generally a good approximation for purpose of transport analysis to take the electron and ion temperatures as surface quantities. This implies that the density is also constant on a magnetic flux surface since $p = p(\psi)$. Thus, the transport problem is reduced to a one-dimensional calculation for the diffusion of particles, current density and thermal energy across the magnetic flux surfaces. The BALDUR code alternates between calculating the magnetic equilibrium and solving the diffusion equations as

follows:

1. Calculate an equilibrium based on an initial guess for the two free functions.

2. Solve the time dependent equations for the diffusion of particles, thermal energy, and longitudinal current across the magnetic flux surfaces subject to the imposed boundary conditions at the edge.

3. Periodically update the magnetic equilibrium using the profiles obtained from solving the transport equations.

Assuming cylindrical flux surfaces, the diffusion equations solved in BALDUR are of the form

$$\frac{\partial n_i}{\partial t} = -\frac{1}{r}\frac{\partial}{\partial r}\left(r\Gamma_i\right) + S_i \ , \tag{4.46}$$

$$\frac{3}{2}\frac{\partial}{\partial t}\left(n_j T_j\right) = -\frac{1}{r}\frac{\partial}{\partial r}\left(rq_j\right) + Q_j \ , \tag{4.47}$$

$$\frac{\partial B_\theta}{\partial t} = \frac{c^2}{4\pi}\frac{\partial}{\partial r}\left[\frac{\eta}{r}\frac{\partial\left(rB_\theta\right)}{\partial r}\right] \ , \tag{4.48}$$

where the subscript $j = i, e$ for ions and electrons, Γ_j and q_j are the particle and heat fluxes, S_i and Q_j are the particle and heat sources, η is the resistivity and B_θ is the poloidal magnetic field. In general, the code allows the particle and heat fluxes to be related to the gradients in the density and temperature through a transport matrix. In this analysis, only the diagonal elements are considered which correspond to the "normal" particle and thermal diffusivities.

The electron thermal conductivity in Eq. (4.40) was implemented as a new subroutine in the BALDUR code. The details of this implementation and the actual subroutine are given in Appendix E. Neoclassical diffusion was assumed for the ions [36] as well as the resistivity. Since the primary purpose of the simulations was to test the thermal transport model, the unnecessary complications involved with particle transport were avoided by setting the density profile to match the experiment. The particle transport was set to zero so that the density profile remained fixed. The functional form used for the density profile was $n(\xi) = (n_o - n_{edge})(1 - \xi^{e_1})^{e_2} + n_{edge}$

where ξ is the normalized toroidal flux, n_o is the central density, n_{edge} is the edge density and e_1, e_2 are numerical coefficients. A typical density profile is shown in Fig. 4-7 with $e_1 \approx 2.7$ and $e_2 \approx 1$.

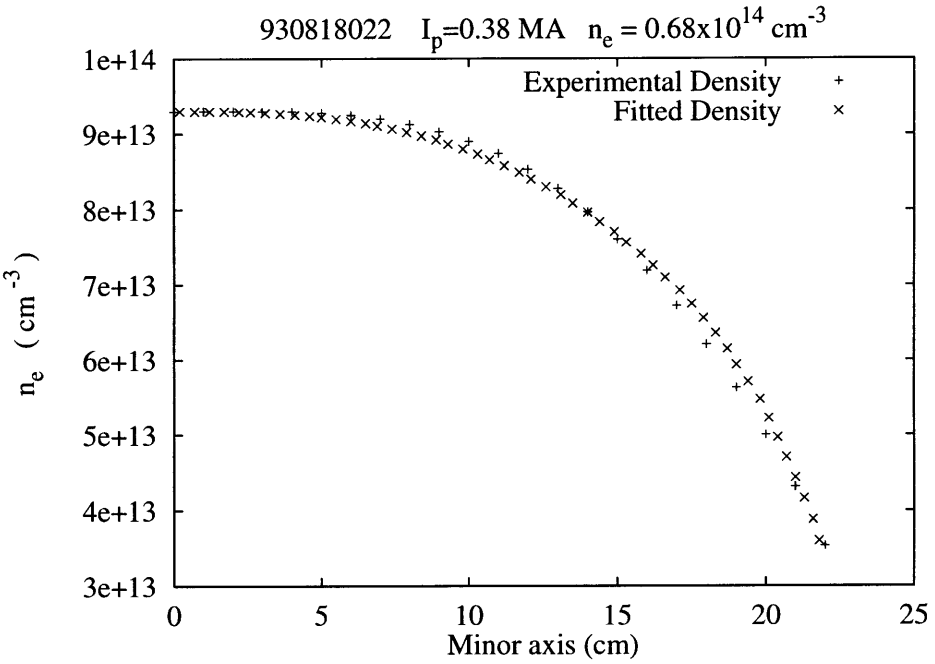

Figure 4-7: Typical electron density profile compared with functional fit used in simulations

The fraction of ICRF heating going to the electron and ion channels was estimated from a Fokker Planck simulation code to determine the distribution function of the minority species and subsequently the collisional transfer of energy to the electrons and main ion species. Typically, 80% of the energy is collisionally transfered to the electron population from the high energy tail of the minority species [54].

For high current discharges with sawteeth, a simple model was used to account for the flattening of the temperature profile within the $q = 1$ surface. The model was set to match the observed sawtooth period, flattening the temperature within the $q = 1$ surface and partially redistributing the current density. The model has an adjustable parameter which allows one to specify the amount of reconnection to some fraction of the original Kadomtsev model. Since there is substantial experimental evidence that

the q profile does not change drastically during the sawtooth [77], this parameter was set to zero resulting in no magnetic reconnection. For most of the discharges considered, the volume inside the $q = 1$ surface is rather small and the details of any sawtooth model do not drastically effect the resulting global parameters such as stored energy and energy confinement time.

The geometric parameters and boundary conditions were set to match a particular Alcator C-Mod discharge at equilibrium. The simulation was performed with an up-down symmetric plasma shape while the actual configurations had a bottom null point. This does not greatly affect the results, to the accuracy considered. The fraction of energy lost to radiation was also set to the experimentally observed value. Comparisons between the simulation and experiment were made by picking arbitrary initial conditions and running the time-dependent transport simulation forward in time until an equilibrium was reached.

4.6.2 Ohmic Discharges

Ohmic discharges where selected to be as close as possible to steady state and covering a wide range of the available parameter space. Parameters for the selected discharges are given in Table A.2. The simulated temperature profile and thermal diffusion coefficients for a typical ohmic discharge are shown in Fig. 4-8. The error-bars for the experimentally determined electron temperature profiles are approximately $\pm 10\%$ outside the $q = 1$ surface but can be considerably larger inside this region when there are strong sawtooth oscillations. The details of the comparison for the other selected discharges are given in Appendix A. Global quantities resulting from the simulation are compared to the experimental values in Table A.3. Simulated electron temperature profiles are compared with the experimentally measured electron temperature profiles in Figures A-1 through A-10. Comparison between the simulated and experimentally measured quantities is quite favorable for the discharges considered. Experimental ion temperature profiles were not available. The central ion temperature is estimated from a neutron count and used to calculate the ion stored energy assuming a functional form for the profile. The ion stored energies shown in Table A.3

are in good agreement considering the error bars for the kinetic stored energy [78] are ±10%. It is difficult to make comparisons for the electron temperature profile inside the $q = 1$ surface for high current discharges with strong sawtooth oscillations. Nevertheless, the simulated central temperature appears a bit high in a few of the ohmic discharges (see Figures A-6, A-7 and A-9). It is important to emphasize that the diffusion coefficient developed in this analysis does not include the effect of sawteeth. A simple model is used to flatten the temperature at a set period and comparisons are made shortly after the sawtooth crash. The error bars for the electron temperature in the sawtooth region can be considerably larger than the error estimate outside this region (typically ±10%). The high current ICRF discharges agree rather well with the measured electron temperature profiles. The ICRF discharges are more centrally peaked and do not exhibit the dramatic flattening present in some of the high current ohmic discharges.

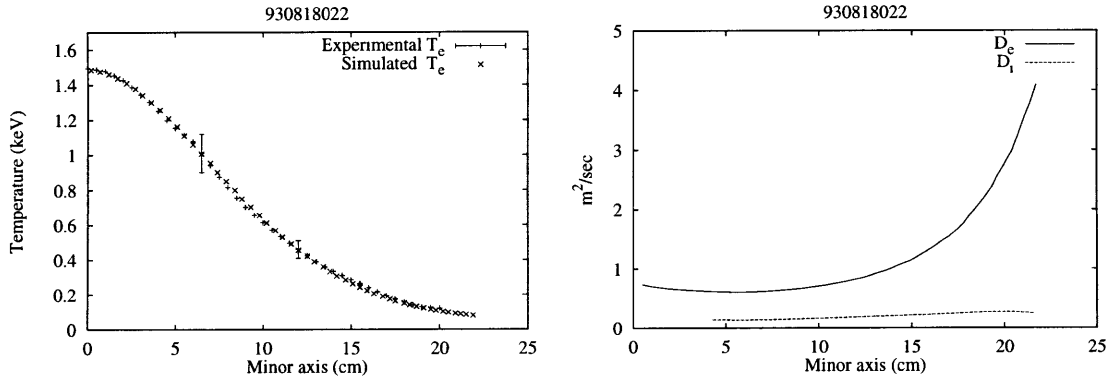

Figure 4-8: Simulated electron temperature profile and diffusion coefficients for a typical ohmic discharge

4.6.3 ICRF Discharges

A group of ICRF heated discharges were selected spanning the range of the heating power and chosen as close to steady state as possible. Parameters for the selected discharges are given in Table B.1. Global quantities resulting from the simulation are compared to the experimental values in Table B.2. Simulated electron temperature

profiles are compared with the experimentally measured electron temperature profiles in Figs. B-1 through B-10. The comparison between the simulated and experimentally measured quantities is quite favorable.

4.6.4 Sensitivity to Boundary Conditions

As mentioned previously, the transport simulation requires the electron and ion temperatures at the edge as a boundary condition. Since the edge temperatures are not always well measured, this introduces another important source of uncertainty in the transport analysis. In these simulations, it was assumed that the electron and ion temperature were equal at the edge $T_e = T_i$ and the edge temperature was extrapolated from the experimental ECE temperature profile. The simulated temperature profiles resulting from varying the edge temperature by $\pm 50\%$ are shown for a typical ohmic discharge in Fig. 4-9. The variation in the peak temperature is only 3% but variations in other quantities such as stored energy and energy confinement time are more significant $\pm$ 20%. This source of uncertainty is important to note in evaluating the fit of any particular discharge.

4.6.5 Relevance of Simulations

Although the proposed diffusion coefficient is constructed with the guidance of an experimental scaling, it should be emphasized that this does not guarantee that the coefficient can reproduce the actual temperature profiles. The scaling is only one piece of information in determining the form of the diffusion coefficient. The actual coefficient draws on other key elements such as profile consistency and the assumption of an underlying pressure driven instability. The only way to determine if such a coefficient can reproduce the actual discharges is to carry out a series of transport simulations and make careful comparisons with experiment. It is entirely possible to construct a coefficient which is consistent with the global scaling, yet cannot reproduce the profiles. Thus, the transport simulations are a necessary and vital part of the analysis.

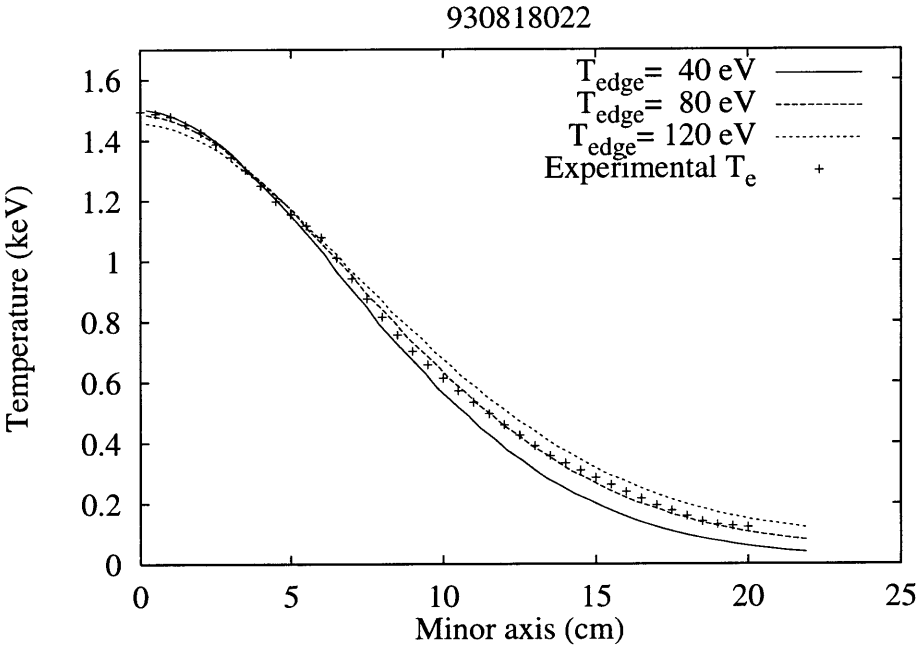

Figure 4-9: Simulated temperature profiles obtained by varying the edge boundary condition by $\pm 50\%$

There is another important reason for carefully checking that the thermal diffusion coefficient can reproduce the observed temperature profiles. The algebraic transport scaling from Sec. 4.3 can only give a rough estimate of whether a proposed experiment can reach ignition conditions. A more accurate analysis requires a time-dependent simulation to investigate the path to ignition. An accurate temperature profile is crucial in calculating the fusion power and consequently in predicting if ignition can be reached. It is not hard to imagine diffusion coefficients which have the same global scaling but a substantially different radial dependence. In these type of simulations, a diffusion coefficient which has been carefully benchmarked against the temperature profiles of actual experiments is highly desirable.

4.7 Extrapolation to Proposed Experiments

A primary purpose of transport scalings is to extrapolate the confinement characteristic of machines envisioned to operate at or near ignition conditions. There are currently several research programs which are pursuing studies of ignition machines. The machines considered are of tokamak design, but take drastically different approaches to the goal of studying the physics of an ignited plasma.

The first machine designed to reach ignition is the Ignitor experiment [67]. Ignitor is the natural development in the line of high magnetic field, high density experiments represented by the Alcator machines built at MIT and the FTU machines at Frascati. The Ignitor design seeks to exploit the good confinement characteristics of ohmic heating to the maximum extent in an attempt to reach ignition with high density ($n_o \approx 10^{21}$ m^{-3}) and relatively moderate temperatures ($T_{e0} \approx T_{i0} \approx 12$ keV). An ICRF heating system is included to accelerate the ignition process, but detailed numerical simulations indicate that ignition is possible with ohmic heating alone. Parameters for the proposed machine are shown in Table 4.2 along with the confinement time extrapolated from this analysis.

The second proposed experiment is the well-known international collaboration ITER (International Experimental Thermonuclear Reactor). This project started with the much more ambitious goal of demonstrating for the first time the technological feasibility of fusion energy as a source of electric power but with the limitations imposed by stability considerations, known density limit, expected rate of transport and technical feasibility, these goals have been revised. As shown in Table 4.2, the proposed design is dramatically larger than Ignitor, with much lower field and density.

Ignitor is designed to reach ignition with 20 MW of alpha particle heating and with an L-mode level of energy confinement. Extrapolations based on this analysis indicate that this is a reasonable goal. ITER is designed to obtain a prolonged fusion burn with significant α-particle poisoning and 300 MW of α-particle heating. To achieve this goal, the necessary confinement time is approximately $\tau_E \sim 6$ seconds. Based on this analysis, an enhancement in confinement of roughly 3.5 over the L-

mode level is required to meet this goal. Considering the best H-mode plasmas are typically a factor of 2 better confined than the equivalent L-mode plasma [78], this goal seems unrealistic.

Table 4.2: Extrapolation of energy confinement scaling Eq. (4.23) to proposed experiments

	Ignitor	**ITER**
I_p	12 MA	21 MA
P_H	20 MW (15)	300 MW (200)
B_T	13 T	5.7 T
$\overline{n}_e$	6×10^{20} m^{-3}	1×10^{20} m^{-3}
R	1.3 m	8.14 m
a	0.47 m	2.8 m
κ	1.8	1.6
δ	0.4	0.24
τ_E	0.49 sec (0.6)	1.7 sec (2.0)

4.8 Alternate Diffusion Coefficient with Heat Pinch

The diffusion coefficient developed in Sec. 4.5 is consistent with the observed transport scaling in Eq. (4.17) but was developed under the assumption that the heat flux is proportional to a local gradient in the temperature. Another possibility to consider is a heat flux of the form

$$\vec{q} = -nD^{th}\nabla T - \vec{q}_p \ , \tag{4.49}$$

where D^{th} is the thermal diffusion coefficient and $\vec{q}_p$ is a heat pinch. As noted by previous researchers [59, 58], a heat flux of this form will also give rise to a linear offset type scaling. This is easy to show by considering an energy balance over the outermost surface

$$\int \vec{q} \cdot d\vec{A} = P_H \ , \tag{4.50}$$

where P_H is the heating power. For simplicity, assume that the dominant diffusion is through the electrons and consider cylindrical geometry. Again assume a canonical

temperature profile of the form $T_e = T_{eo}\, exp[-\alpha(r) r^2/a^2]$ where α is a weak function of r. Inserting Eq. (4.49) and integrating Eq. (4.50) gives

$$\left[\frac{2\alpha n T_e D_e^{th}}{a} - q_p\right] (2\pi)^2 aR = P_H \ . \tag{4.51}$$

Consider a thermal diffusion coefficient of the form developed in Sec. 4.5 but without the inflow term

$$D_e^{th} \approx \frac{\mathcal{V}_o^o}{8\pi^2} \frac{I_p}{nT_e} \frac{1}{R} \frac{\beta_p}{q_E^{2/3}} \frac{1}{f_1} \ , \tag{4.52}$$

Inserting Eq. (4.52) into Eq. (4.51) and simplifying results in

$$\frac{\beta_p}{q_E^{2/3}} \approx f_1 \frac{P_H}{\alpha I_p \mathcal{V}_o^o} + f_1 \frac{(2\pi)^2 aR}{\alpha I_p \mathcal{V}_o^o} q_p \ , \tag{4.53}$$

which is identical in form to the scaling found in Eq. (4.17) where the offset term is now related to the heat pinch. A diffusion coefficient of the form shown in Eq. (4.52) along with an appropriate heat pinch term is also consistent with the global confinement scaling. Comparing the second term on the right hand side of Eq. (4.53) with the equivalent term in Eq. (4.17) results in a heat pinch of the form

$$q_p = \frac{\alpha}{(2\pi)^2} \frac{I_p \mathcal{V}_o^o}{aR} \frac{f_2}{f_1} = \frac{0.14\alpha}{(2\pi)^2} \left(\frac{I_p \mathcal{V}_o^o}{a^2}\right) \left(\frac{a}{d_i}\right)^{1/2} A_i^{1/4} \ . \tag{4.54}$$

It is important to note that this expression for the heat pinch is similar to the result reported by Kikuchi [60] for discharges in JT60. In a series of ohmic and neutral beam heated discharges, it was found that a heat pinch term proportional to $n_e B_p$ was consistent with the experimental observation.

The basic radial dependence of the heat pinch in Eq. (4.54) would be closely related to the ohmic heating profile with the weak function α allowing a small variation. Obviously, on a global basis it is not possible to distinguish this model from the purely diffusive model in Sec. 4.5 since both have the same global scaling.

4.9 H-Mode Regime

A regime of enhanced confinement can be induced when the average heating power exceeds a critical level. A recent analysis [79] on the threshold power to enter this regime indicates that it scales as

$$P_T = 0.65 \overline{n}_e^{0.93} B_T^{0.86} R^{2.15} \,, \tag{4.55}$$

where the power is in MW, the line averages density $\overline{n}_e$ is in m^{-3}, the toroidal field is in Tesla and the major radius is in meters.

It is well established that the enhanced confinement is associated with the onset of a transport barrier near the edge of the plasma column. Here it is assumed that the barrier is described by the addition of a localized inflow or energy flux reflection term in the relevant transport equation. Thus, the L-mode scaling of Eq. (4.17) and the associated diffusion coefficient in Eq. (4.40) are modified to include a third term. Based on data from Alcator C-Mod, DIII-D and JET a possible form for this is

$$\beta_p \approx q_E^{2/3} \left(f_1 \frac{P_H}{I_p \mathcal{V}_o} + f_2 \right) + C_H \left(\frac{a}{d_i} \right)^{1/2} q_E^{6/5} \left(\frac{R}{a} \right)^{2/3} \left(\frac{\omega_{pe}}{\Omega_{ce}} \right)^{2/3} \,, \tag{4.56}$$

where $C_H \approx 8.6 \times 10^{-3}$. A comparison between Eq. (4.56) and the H-mode database assembled for the ITER project [80] is made in Fig. 4-10. The data for Alcator C-Mod in this figure is from the Alcator transport database. The scaling for the energy confinement time resulting from Eq. (4.56) is compared with the same set of H-mode discharges in Fig. 4-11. The comparison is quite good for the machines considered. A detailed comparisons for each machine considered is given in Appendix D.

Since confinement in the H-Mode is dependent on the details of the edge physics, the inflow term might vary significantly in different machines. In addition, several different types of H-Modes have been identified [81] with different levels of enhanced confinement making it rather difficult to find a general scaling for the inflow term.

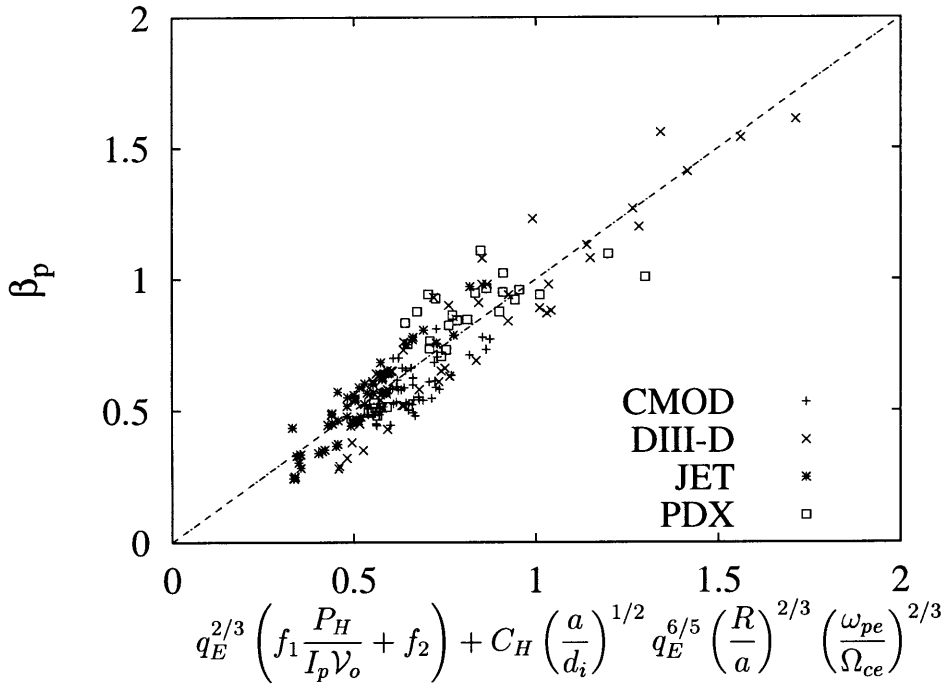

Figure 4-10: Comparison of β_p scaling in Eq. (4.56) with selected discharges in ITER H-mode database

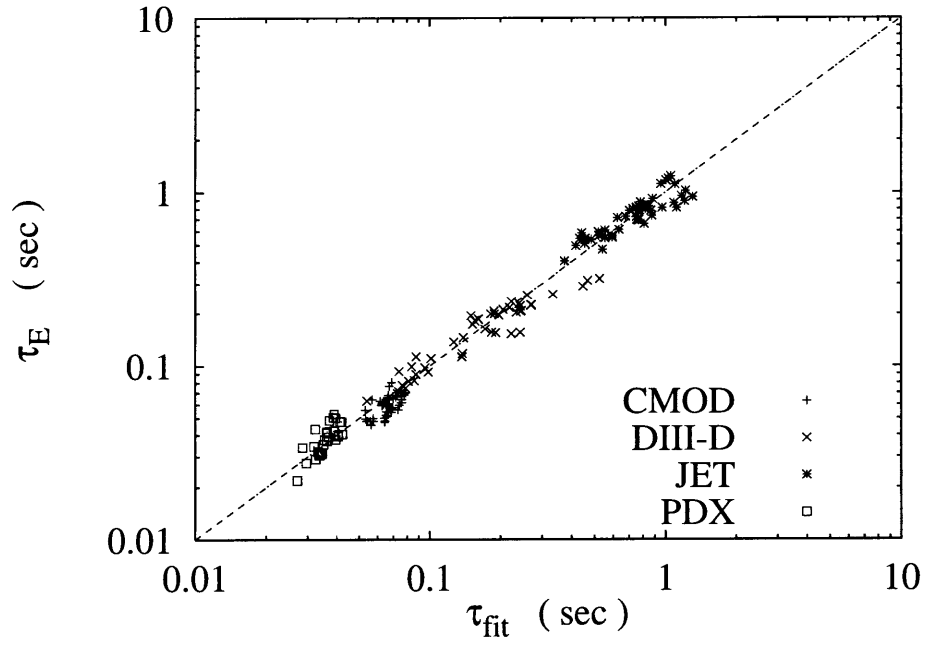

Figure 4-11: Comparison of τ_E scaling with selected discharges in ITER H-mode database

4.10 Summary

A novel scaling for the energy confinement of ohmic and L-mode plasmas has been identified in terms of relevant dimensionless parameters. The basic result is that $\beta_p/q_E^{2/3}$ increases linearly with the ratio of the total heating power to a characteristic ohmic heating power $P_H/(I_p\mathcal{V}_o^o)$ and that a significant off-set is found. This type of off-set was originally proposed in connection with plasmas produced by the Alcator C-Mod machine and has since been found in a number of other experiments. The off-set may be related to a heat pinch, an off-diagonal term in a transport matrix or some other process which tends to reduce the outward transport of energy in some region of the plasma. The relative importance of this off-set term is diminished when the total heating power greatly exceeds the characteristic ohmic level. This accounts for the confinement degradation typically observed in L-mode plasmas. In contrast to power law scalings, this analysis predicts that confinement times will saturate for large heating powers.

The composite scaling developed in this analysis is shown to provide a substantially better fit to experiment than a power law regression for six of the seven machines considered. The RMS error for the composite scaling of the stored energy is 13% which is nearly half the error of the best power law regression. The comparison is particularly favorable for the compact high field experiments where the RMS error for the power law scalings is 30%.

Extrapolations were made for the confinement characteristics of several proposed ignition experiments. The scaling for the energy confinement time from this analysis (see Eq. (4.23)) has a weaker dependence on geometry than the power law scalings. It is interesting to note that recent results from the Alcator C-Mod machine also indicate that the geometry dependence in standard power law scalings may be too strong [78]. The resulting prediction for the L-mode confinement of large machines such as ITER is not favorable for reaching the goal of ignition. The extrapolation for the Ignitor machine is consistent with previous estimates indicating that ignition is a reasonable goal.

A thermal transport coefficient is developed which is consistent with the composite scaling. In nearly two dozen ohmic and ICRF heated discharges, the transport coefficient is shown to reproduce the observed stored energies and energy confinement time. Comparison between the experimental and simulated electron temperature profile is quite good with the exception of a few high current ohmic discharges where the simulated central temperatures are marginally high. As mentioned previously, comparison of the temperature profile inside the $q = 1$ surface is difficult for plasmas with large sawteeth. The physics involved with sawtooth oscillations is not included in the thermal diffusion coefficient developed in this analysis so it is not surprising that differences can arise in discharges with large sawteeth.

The transport coefficient developed in this analysis may be useful in examining the performance of proposed experiments. The coefficient is comparatively simple in form and contains only two free parameters. A potential weakness in using the transport coefficient to predict the performance of future machines is that the edge temperature must be supplied as a boundary condition. The sensitivity analysis performed for this coefficient, indicates that the central temperature varies weakly with the edge temperature but that variations in the stored energy can be somewhat larger. The best approach would to be examine the most likely range of edge temperatures and give the corresponding uncertainties.

An important indication from this analysis is that confinement in toroidal plasmas is determined by both an outward diffusive process and a secondary mechanism which tends to reduce this outward flux. It is not possible to determine the specific nature of this secondary process from the global confinement data which is readily available, since phenomena with very different origins can have the same global scaling. Certainly, the idea warrants further study.

Appendix A

Comparison of Simulation with Alcator C-Mod Ohmic Discharges

In this appendix, detailed comparisons are made between the simulations described in Sec. 4.6 and experimentally measured results for ohmic plasmas. In Table A.1, the various parameters of interest are defined along with typical error bars [78]. The parameters for the selected discharges are given in Table A.2. Experimental and simulated global quantities are compared in Table A.3. The simulated temperature profiles are compared with the experimentally determined profiles in Figs. A-1 through A-10.

Table A.1: Description of plasma variables and typical error bars

Variable	Description	Typical Error Bar [78]
I_p	plasma current	3 kA
$\overline{n}_e$	line average density	5 - 10%
β_p	$8\pi\overline{p}/\langle B_p^2\rangle$	0.05 - 0.1
	where $p = n_i T_i + n_e T_e$ and $\overline{p}$ is the volume average	
V_L	loop voltage	
W_e	electron stored energy (from kinetics)	20%
W_i	ion stored energy (from kinetics)	20%
T_e	electron temperature from ECE diagnostic	$\pm$ 10%
P_{oh}	ohmic heating	
P_{rf}	ion cyclotron resonance heating power	10%
P_{rad}	radiative power loss	15 - 20%
Z_{eff}	$= \left[\sum_j Z_j^2 n_j\right] / n_e$ summed over ion species	

Table A.2: Experimental parameters of selected Alcator C-Mod ohmic discharges

shot	I_p (MA)	$\overline{n}_e$ 10^{14} (cm^{-3})	P_{oh} (MW)	P_{rad} (MW)	Z_{eff}
930818011*	0.38	0.83	0.50	0.22	1.8
930818022*	0.38	0.68	0.51	0.24	2.1
940603018	0.41	0.88	0.52	0.37	1.4
931021022	0.57	1.1	0.52	0.13	1.0
931008014	0.61	0.94	0.61	0.19	1.3
931006015	0.68	0.78	0.70	0.21	1.6
940603012	0.79	1.3	1.1	0.68	1.2
931013013	0.80	1.8	1.1	0.21	1.0
931021010	0.85	1.2	0.93	0.21	1.2
931012007	0.99	1.5	1.3	0.27	1.0
950209029	1.2	1.7			1.5

* These are hydrogen discharges.

Table A.3: Comparison of simulation with experiment for ohmic discharges

shot		τ_E (msec)	V_L (volt)	W_e (kJ)	W_i (kJ)
930818011	Exp.	23	1.5	7.2	5.1
	Sim.	20	1.7	6.5	6.3
930818022	Exp.	18	1.4	5.6	3.6
	Sim.	16	1.7	5.6	4.4
940603018	Exp.	26	1.15	7.4	6.5
	Sim.	21	1.33	6.9	5.8
931021022	Exp.	44	1.0	12	12
	Sim.	44	0.95	14	13
931008014	Exp.	42	0.99	14	12
	Sim.	43	1.13	15	13
931006015	Exp.	41	1.00	15	11
	Sim.	37	1.1	15	11
940603012	Exp.	40	1.4	18	16
	Sim.	38	1.3	19	18
931013013	Exp.	42	1.4	23	23
	Sim.	43	1.4	23	22
931021010	Exp.	41	1.2	20	18
	Sim.	44	1.1	22	20
931012007	Exp.	37	1.4	23	26
	Sim.	39	1.5	25	23
950209029	Exp.	32	1.8		
	Sim.	33	1.5	32	29

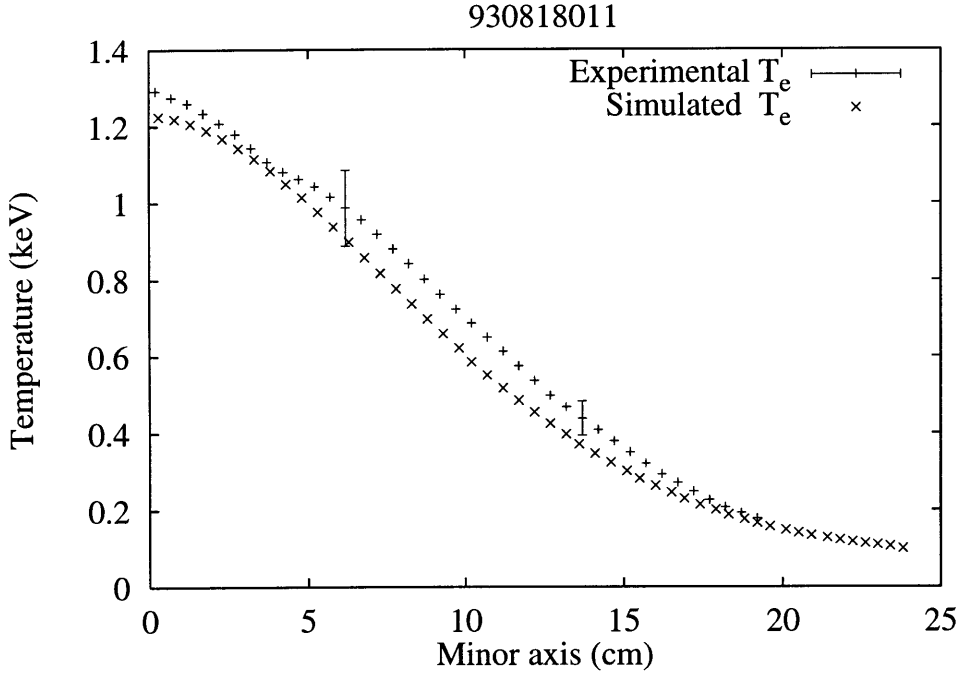

Figure A-1: Comparison of simulated and experimental ECE temperature profiles $I_p = 0.38$ MA, $\overline{n}_e = 0.83 \times 10^{14}$ cm^{-3}

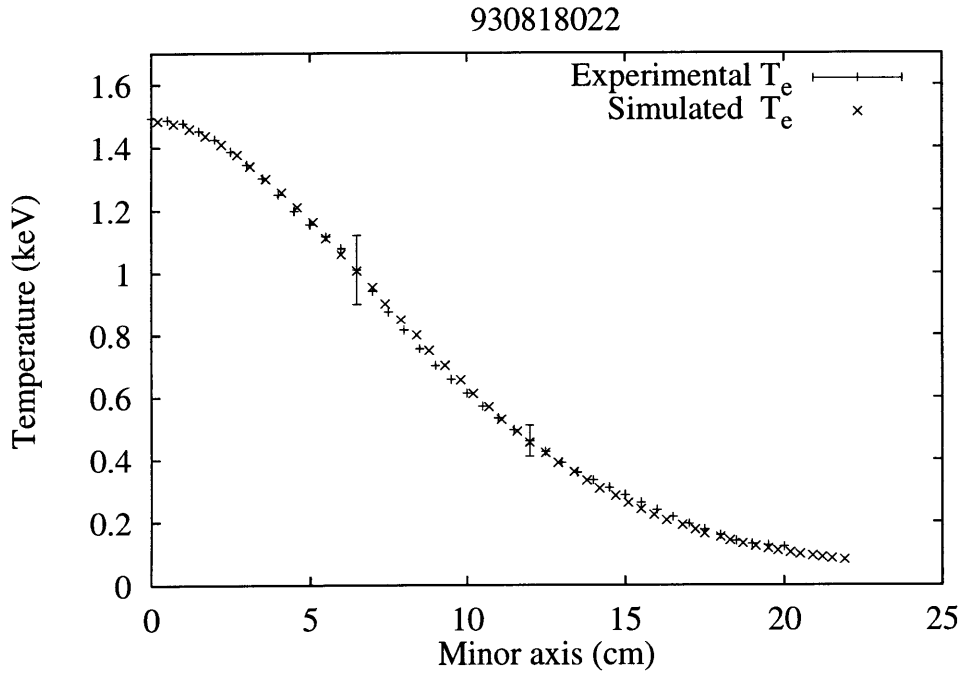

Figure A-2: Comparison of simulated and experimental ECE temperature profiles $I_p = 0.38$ MA, $\overline{n}_e = 0.68 \times 10^{14}$ cm^{-3}

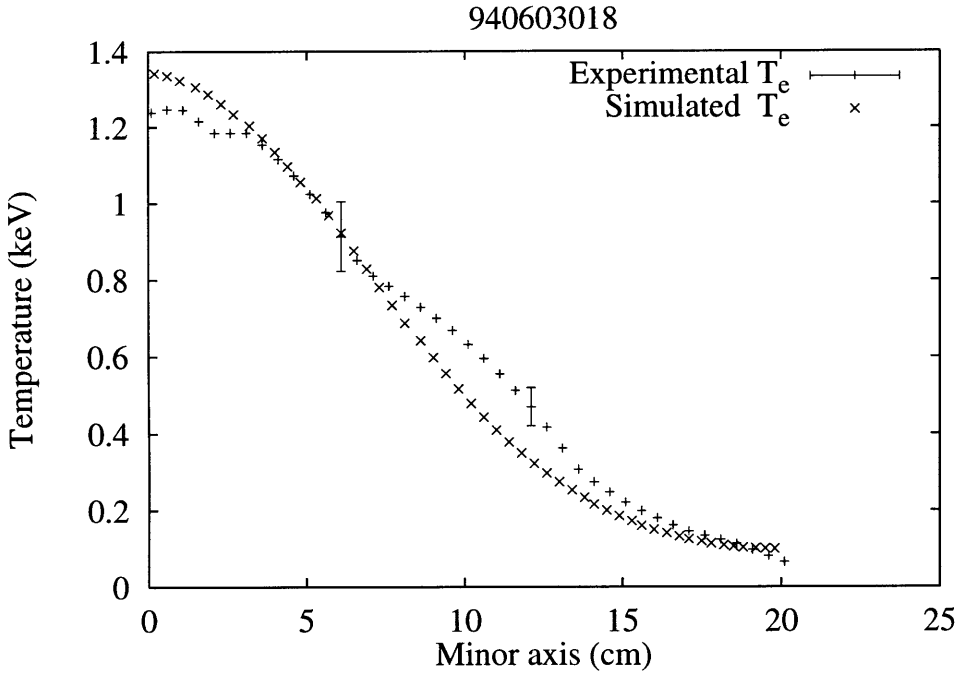

Figure A-3: Comparison of simulated and experimental ECE temperature profiles $I_p = 0.41$ MA, $\overline{n}_e = 0.88 \times 10^{14}$ cm^{-3}

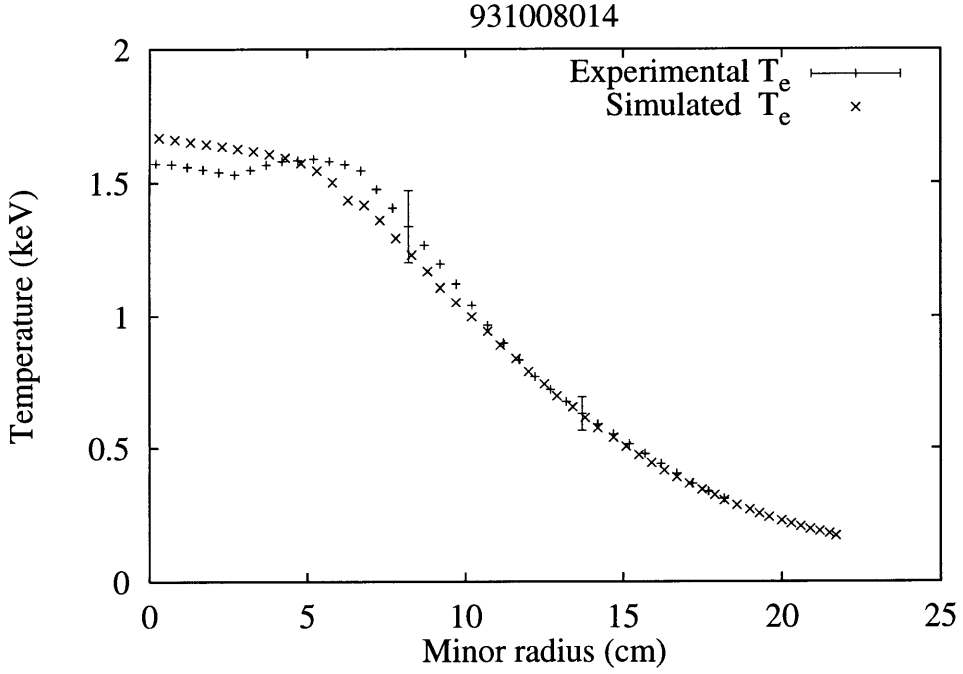

Figure A-4: Comparison of simulated and experimental ECE temperature profiles $I_p = 0.61$ MA, $\overline{n}_e = 0.94 \times 10^{14}$ cm^{-3}

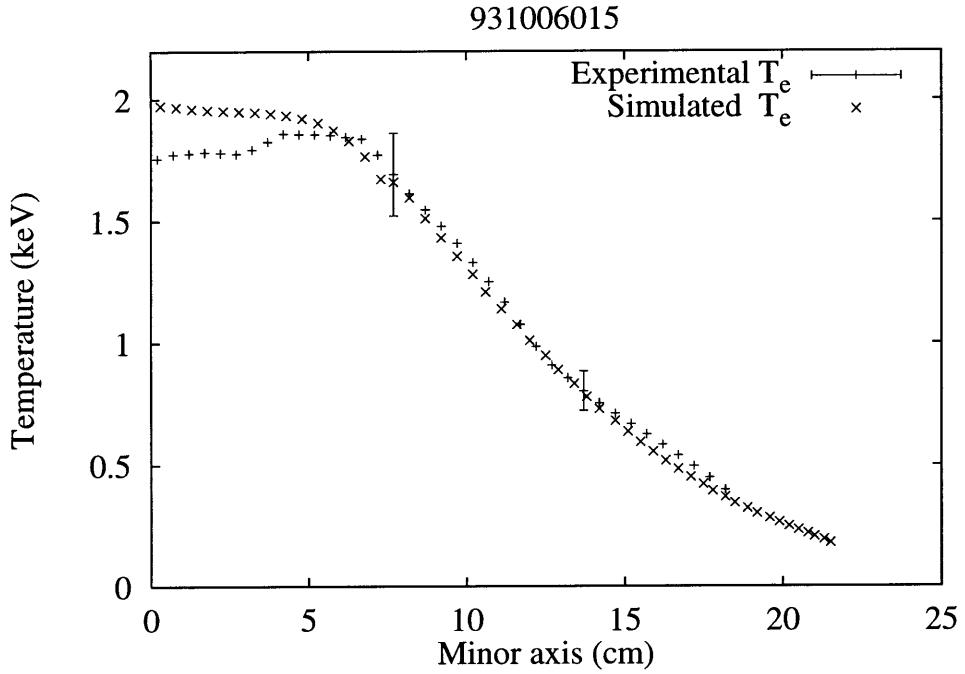

Figure A-5: Comparison of simulated and experimental ECE temperature profiles $I_p = 0.67$ MA, $\overline{n}_e = 0.78 \times 10^{14}$ cm^{-3}

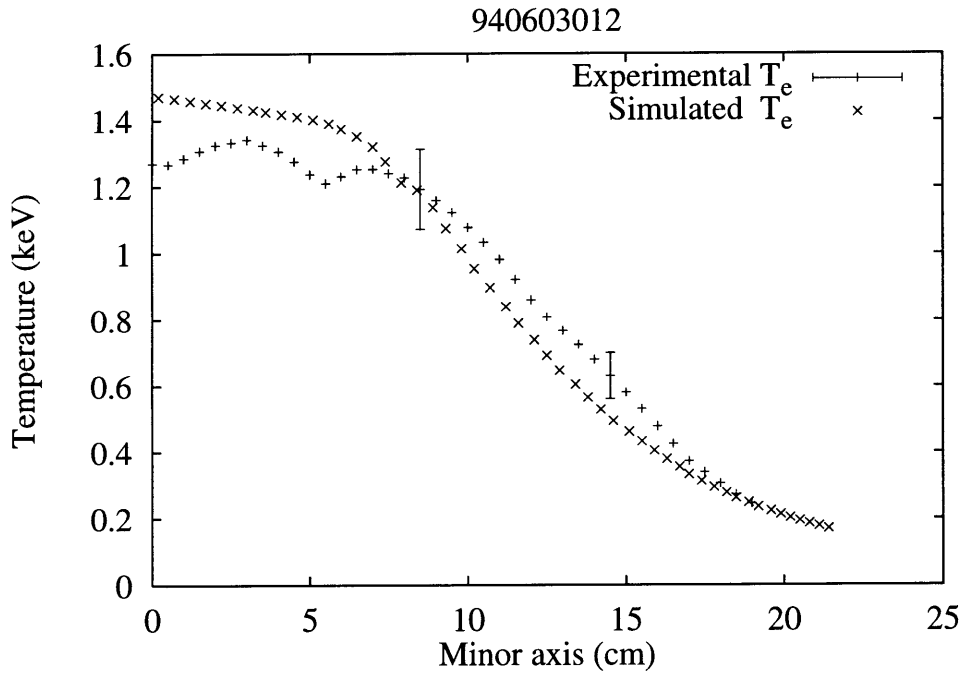

Figure A-6: Comparison of simulated and experimental ECE temperature profiles $I_p = 0.79$ MA , $\overline{n}_e = 1.33 \times 10^{14}$ cm^{-3}

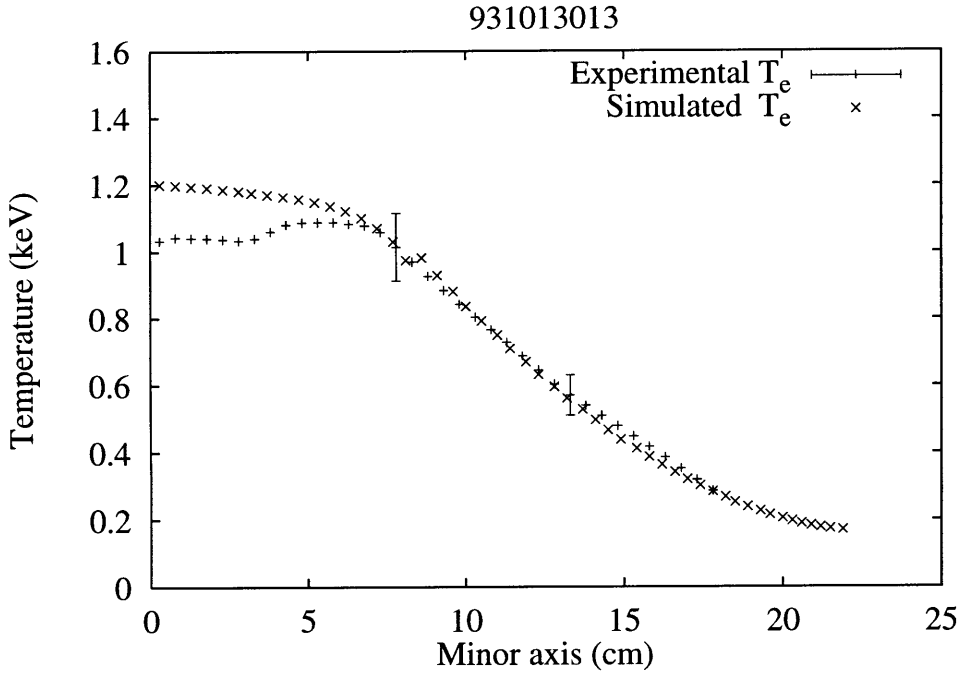

Figure A-7: Comparison of simulated and experimental ECE temperature profiles $I_p = 0.80$ MA, $\overline{n}_e = 1.75 \times 10^{14}$ cm^{-3}

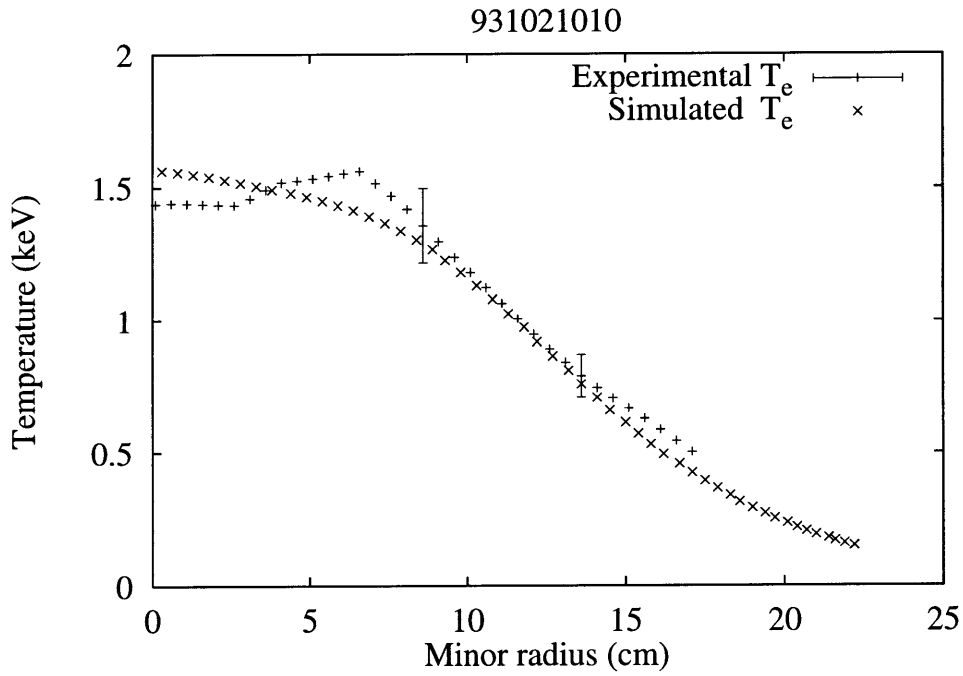

Figure A-8: Comparison of simulated and experimental ECE temperature profiles $I_p = 0.85$ MA, $\overline{n}_e = 1.15 \times 10^{14}$ cm^{-3}

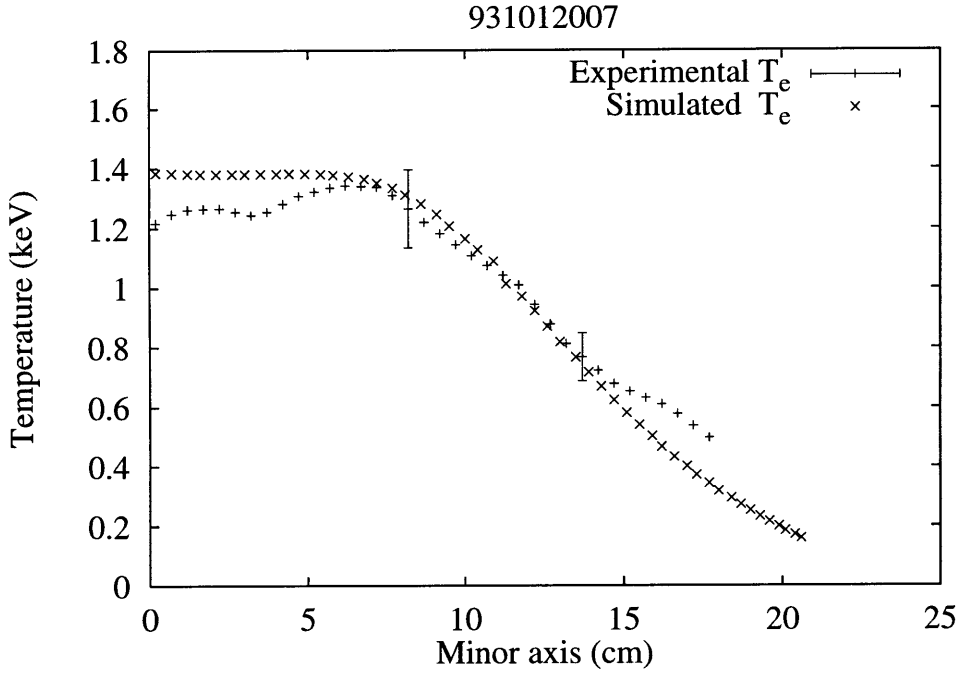

Figure A-9: Comparison of simulated and experimental ECE temperature profiles $I_p = 0.99$ MA, $\overline{n}_e = 1.45 \times 10^{14}$ cm^{-3}

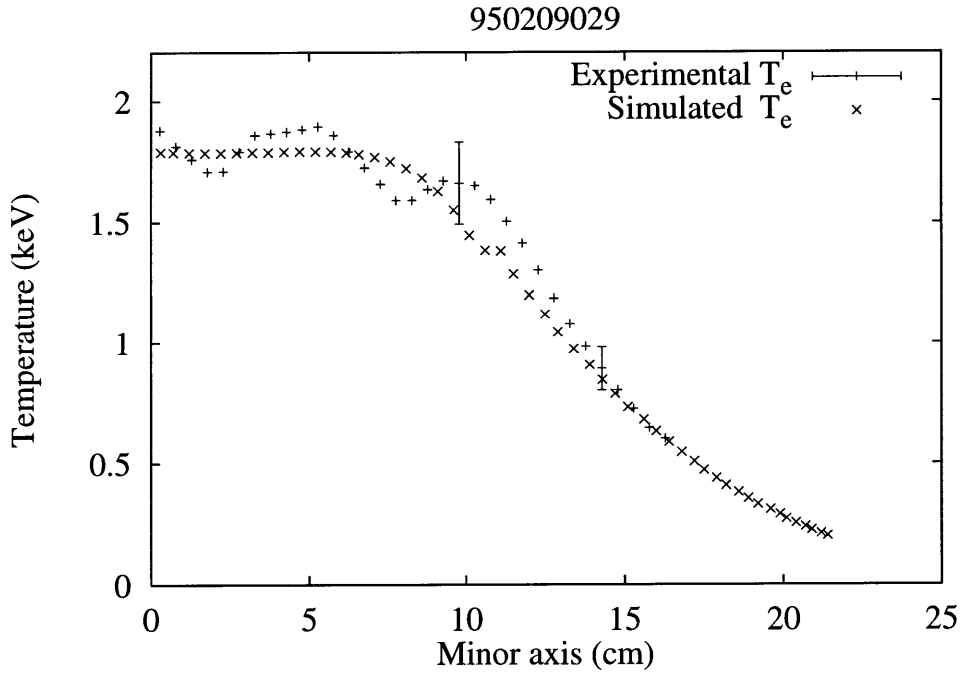

Figure A-10: Comparison of simulated and experimental ECE temperature profiles $I_p = 1.2$ MA, $\overline{n}_e = 1.67 \times 10^{14}$ cm^{-3}

Appendix B

Comparison of Simulation with Alcator C-Mod ICRF Discharges

In this appendix, detailed comparisons are made between the simulations described in Sec. 4.6 and experimentally measured results for ICRF plasmas. In Table A.1, the various parameters of interest are defined along with typical error bars. The parameters for the selected discharges are given in Table B.1 and cover a wide range of the available parameter space. Experimental and simulated global quantities are compared in Table B.2. The simulated temperature profiles are compared with the experimentally determined profiles in Figs. B-1 through B-10.

Table B.1: Experimental parameters of selected Alcator C-Mod ICRF discharges

shot	I_p (MA)	$\overline{n}_e$ (cm^{-3})	P_{rf} (MW)	P_{oh} (MW)	P_{rad} (MW)	Z_{eff}
950302010	1.01	1.55×10^{14}	0.8	1.3	1.4	2.6
950301016	0.64	1.43×10^{14}	0.9	0.6	0.9	1.3
950406036	1.01	2.34×10^{14}	1.2	1.4	1.5	1.9
950208028	0.85	1.62×10^{14}	1.3	0.9	1.2	1.6
950303010	1.02	2.72×10^{14}	1.4	1.4	1.2	1.7
940616025	0.44	0.91×10^{14}	1.5	0.3	0.8	1.9
940602019	0.82	1.51×10^{14}	1.7	0.9	1.1	1.5
950301025	0.64	1.29×10^{14}	2.2	0.5	2.0	3.5
950407016	1.01	1.72×10^{14}	2.9	1.3	3.5	3.0
950118033	0.82	1.00×10^{14}	3.4	1.0	3.4	2.4

Table B.2: Comparison of simulation with experiment for ICRF discharges

shot		τ_E (msec)	V_L (volt)	W_e (kJ)	W_i (kJ)
950302010	Exp.	35	1.3	42	33
	Sim.	31	1.3	34	32
950301016	Exp.	37	0.93	28	24
	Sim.	35	0.91	25	22
950406036	Exp.	34	1.4	49	37
	Sim.	34	1.3	46	43
950208028	Exp.	27	1.1	33	28
	Sim.	26	1.2	31	28
950303010	Exp.	32	1.3	46	40
	Sim.	33	1.5	51	47
940616025	Exp.	15	0.76	14	12
	Sim.	11	0.93	11	10
940602019	Exp.	24	1.	34	25
	Sim.	25	1.1	30	27
950301025	Exp.	25	0.75	35	26
	Sim.	21	0.80	29	27
950407016	Exp.	28	1.2	54	44
	Sim.	23	1.2	48	46
950118033	Exp.	18	1.1		
	Sim.	14	1.1	29	29

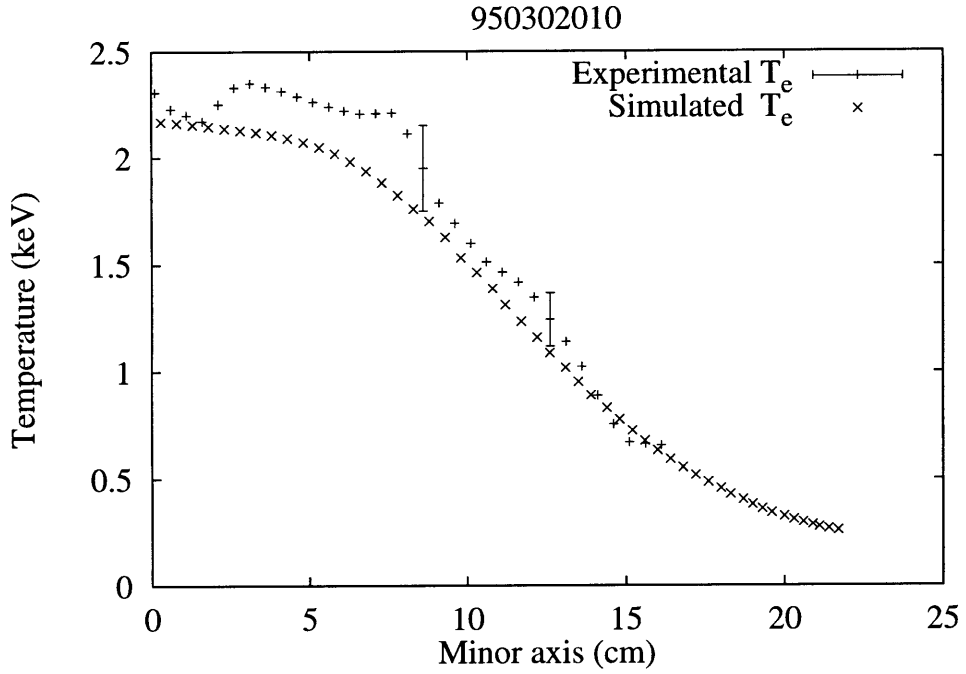

Figure B-1: Comparison of simulated and experimental ECE temperature profiles $I_p = 1.01$ MA, $\overline{n}_e = 1.6 \times 10^{14}$ cm^{-3}, $P_{rf} = 0.78$ MW

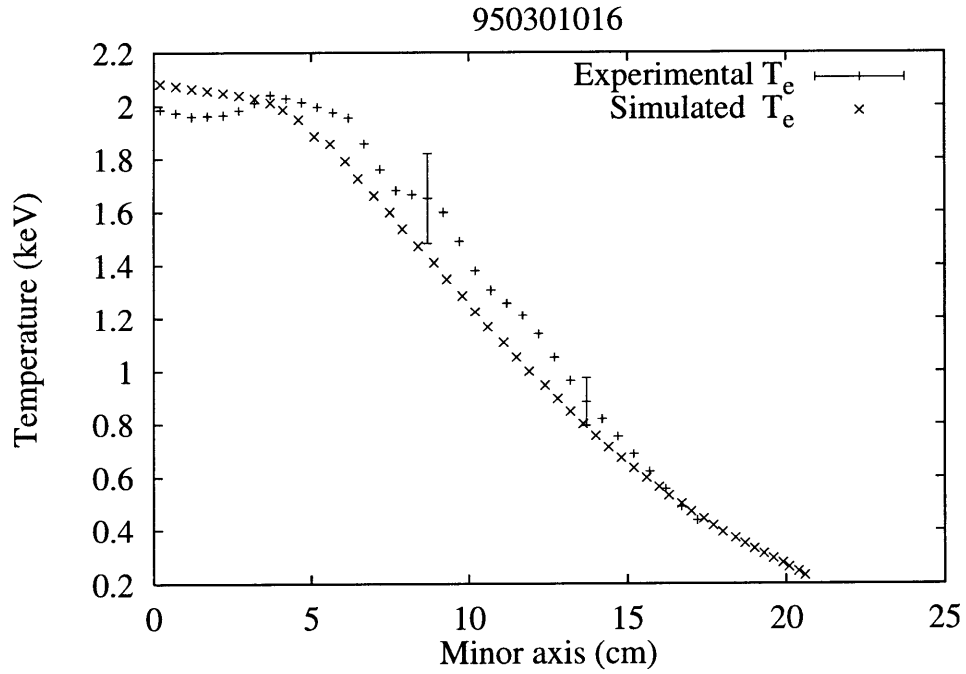

Figure B-2: Comparison of simulated and experimental ECE temperature profiles $I_p = 0.65$ MA, $\overline{n}_e = 1.4 \times 10^{14}$ cm^{-3}, $P_{rf} = 0.9$ MW

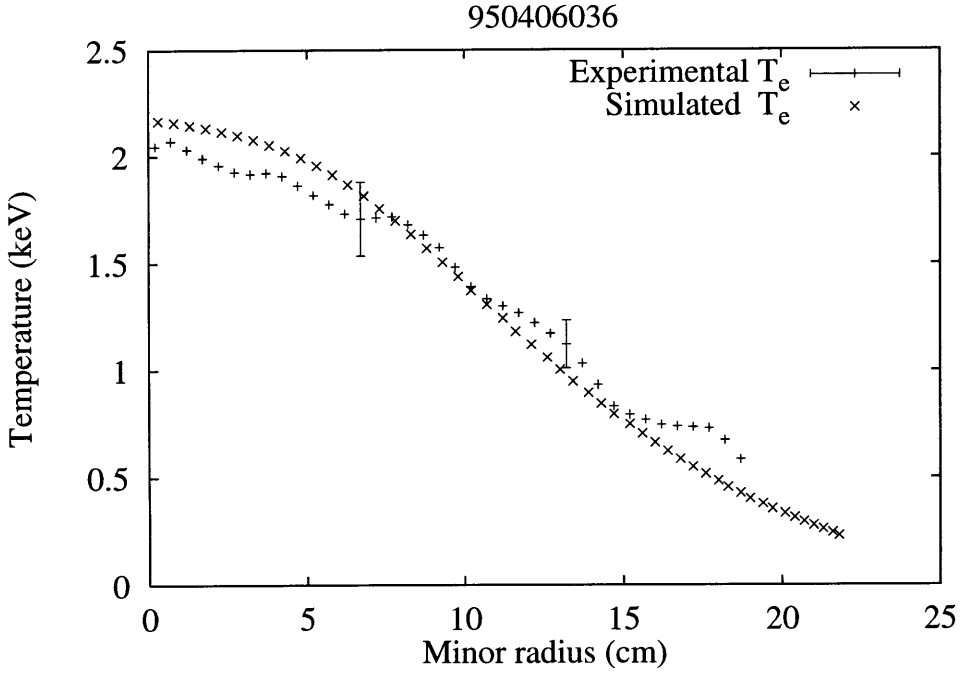

Figure B-3: Comparison of simulated and experimental ECE temperature profiles $I_p = 1.01$ MA, $\overline{n}_e = 1.2 \times 10^{14}$ cm^{-3}, $P_{rf} = 1.2$ MW

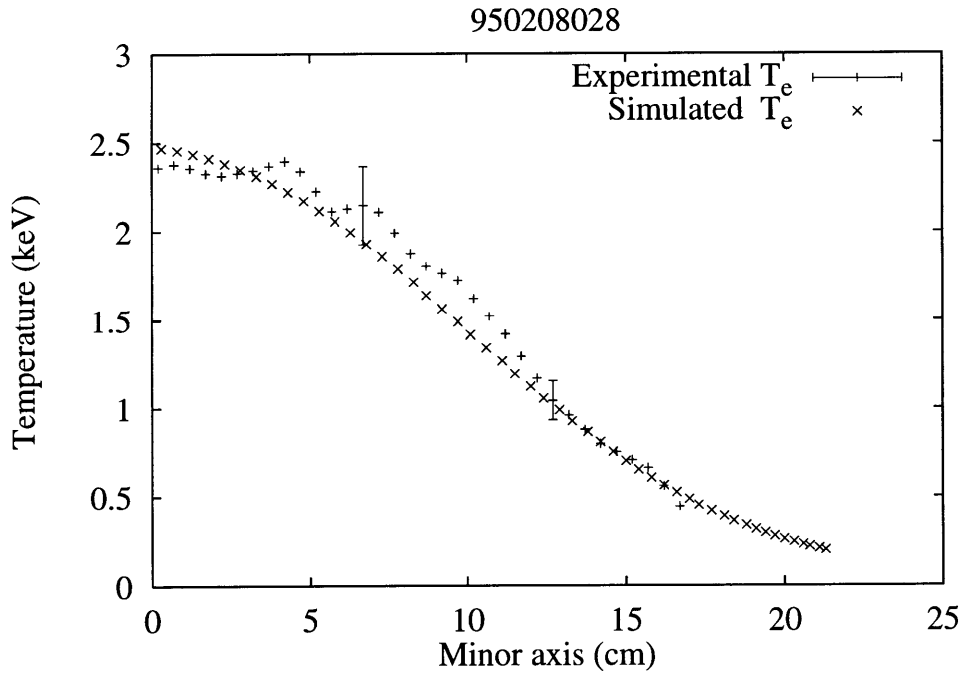

Figure B-4: Comparison of simulated and experimental ECE temperature profiles $I_p = 0.85$ MA, $\overline{n}_e = 1.6 \times 10^{14}$ cm^{-3}, $P_{rf} = 1.3$ MW

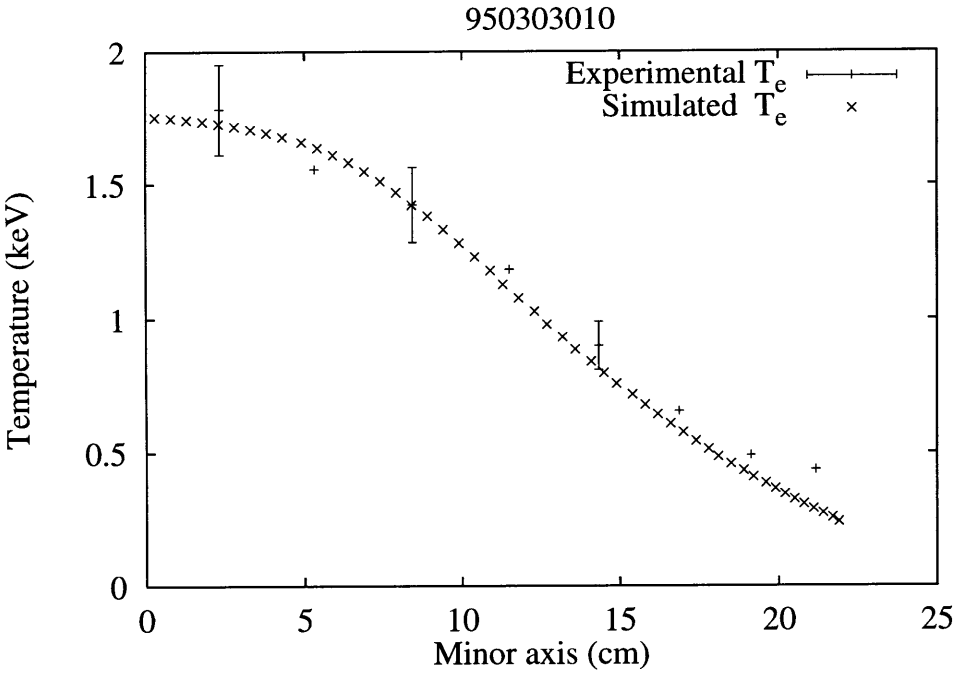

Figure B-5: Comparison of simulated and experimental ECE temperature profiles $I_p = 1.02$ MA, $\overline{n}_e = 2.7 \times 10^{14}$ cm^{-3}, $P_{rf} = 1.4$ MW

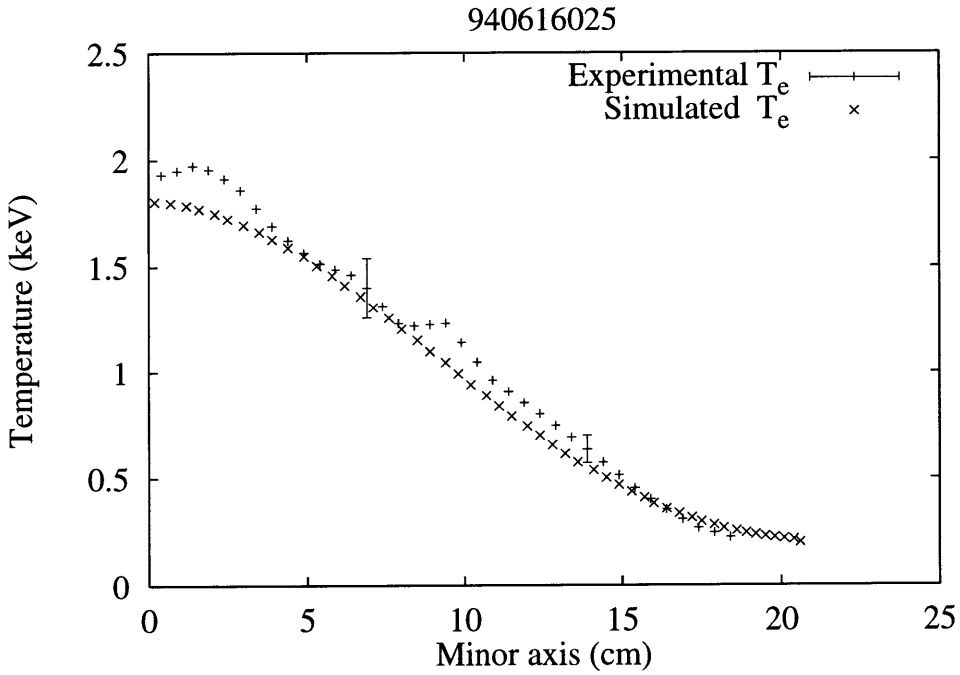

Figure B-6: Comparison of simulated and experimental ECE temperature profiles $I_p = 0.44$ MA, $\overline{n}_e = 0.9 \times 10^{14}$ cm^{-3}, $P_{rf} = 1.5$ MW

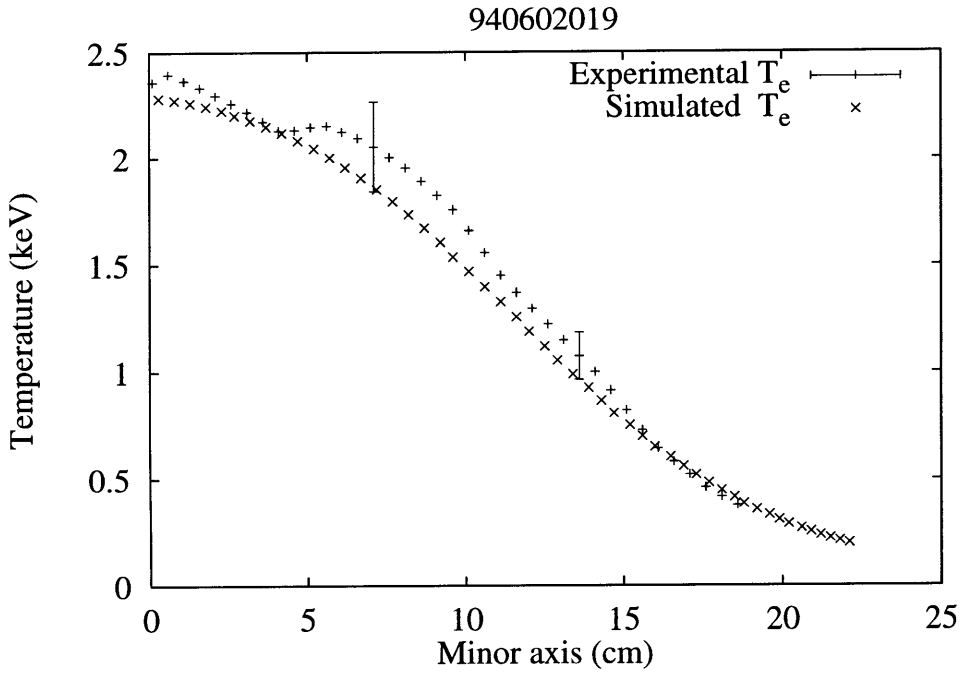

Figure B-7: Comparison of simulated and experimental ECE temperature profiles $I_p = 0.82$ MA, $\overline{n}_e = 1.5 \times 10^{14}$ cm^{-3}, $P_{rf} = 1.7$ MW

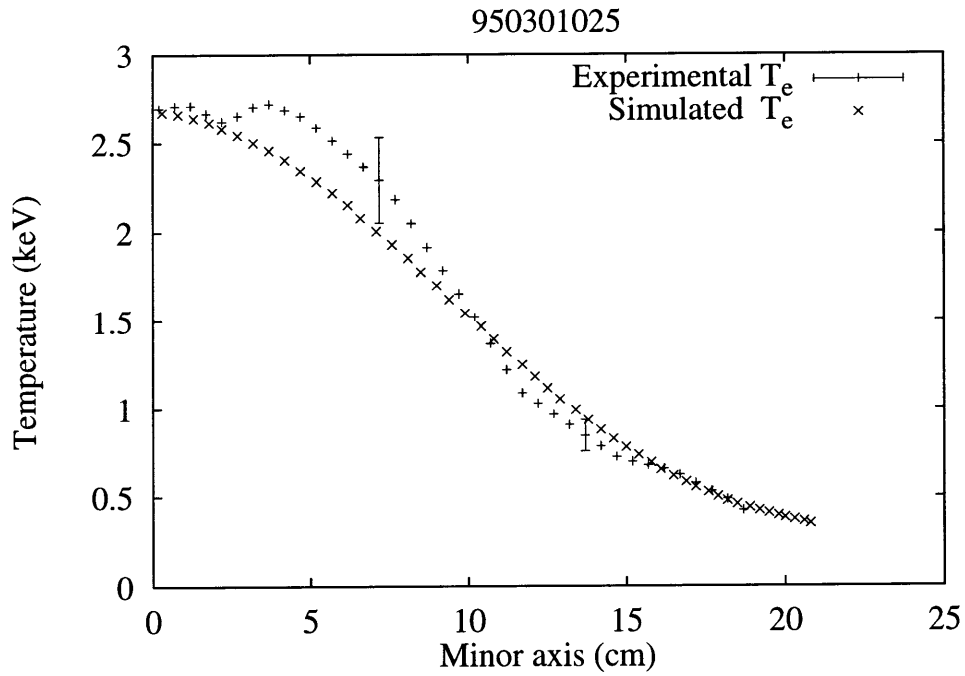

Figure B-8: Comparison of simulated and experimental ECE temperature profiles $I_p = 0.64$ MA, $\overline{n}_e = 1.3 \times 10^{14}$ cm^{-3}, $P_{rf} = 2.2$ MW

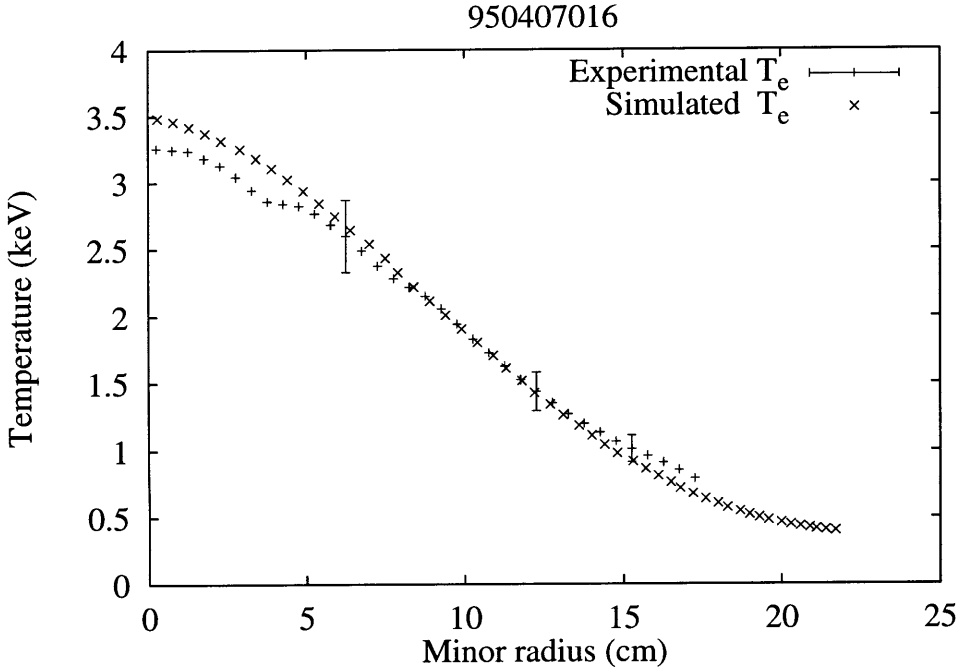

Figure B-9: Comparison of simulated and experimental ECE temperature profiles $I_p = 1.01$ MA, $\overline{n}_e = 1.7 \times 10^{14}$ cm^{-3}, $P_{rf} = 2.9$ MW

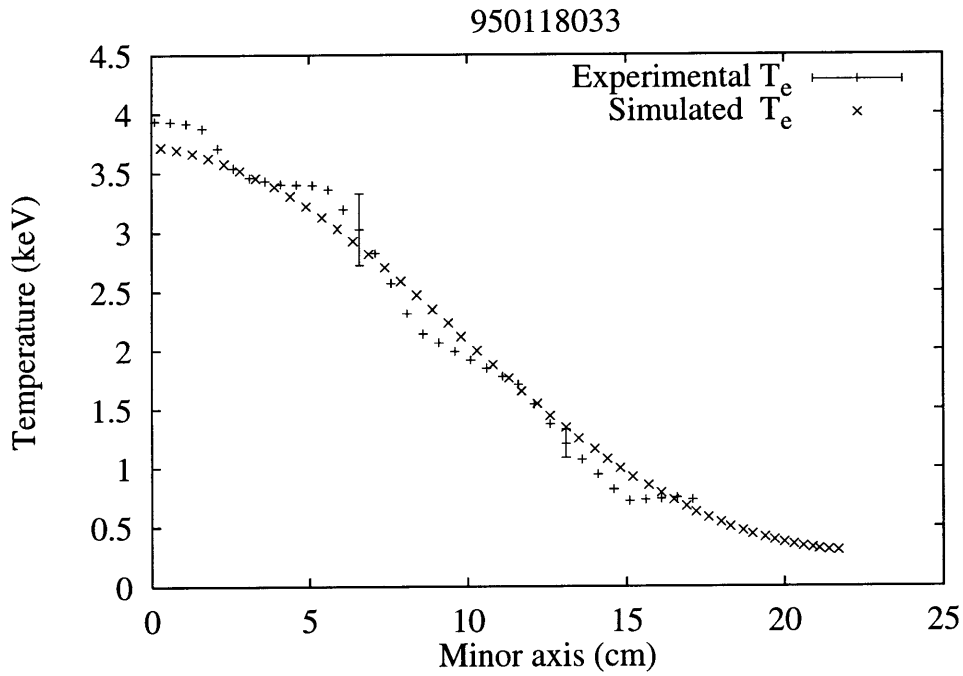

Figure B-10: Comparison of simulated and experimental ECE temperature profiles $I_p = 0.83$ MA, $\overline{n}_e = 1. \times 10^{14}$ cm^{-3}, $P_{rf} = 3.4$ MW

Appendix C

Comparison of L-Mode Scaling with ITER Database

In this appendix, a detailed comparison of the scalings discussed in Chapter 4 are presented. The experimental data is from the database assembled for the ITER project [74]. Discharges were selected from this database based on the selection criteria discussed on page 96. Scalings are showed in both dimensionless form for β_p and in terms of the total stored energy W for each of the machines considered.

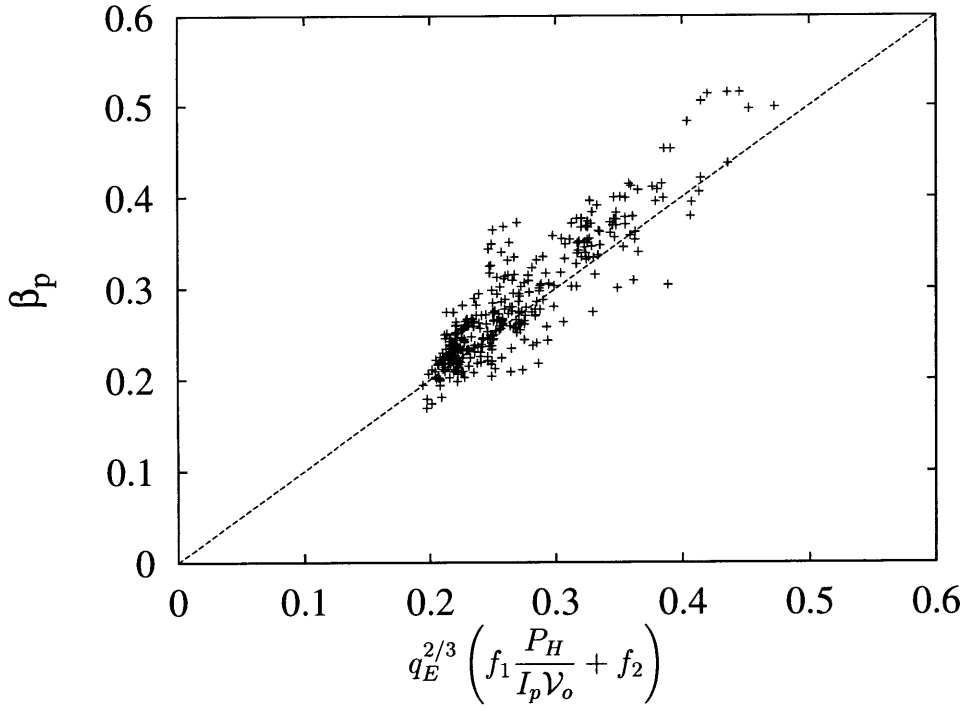

Figure C-1: Comparison of β_p scaling in Eq. (4.17) with discharges from Alcator C-Mod

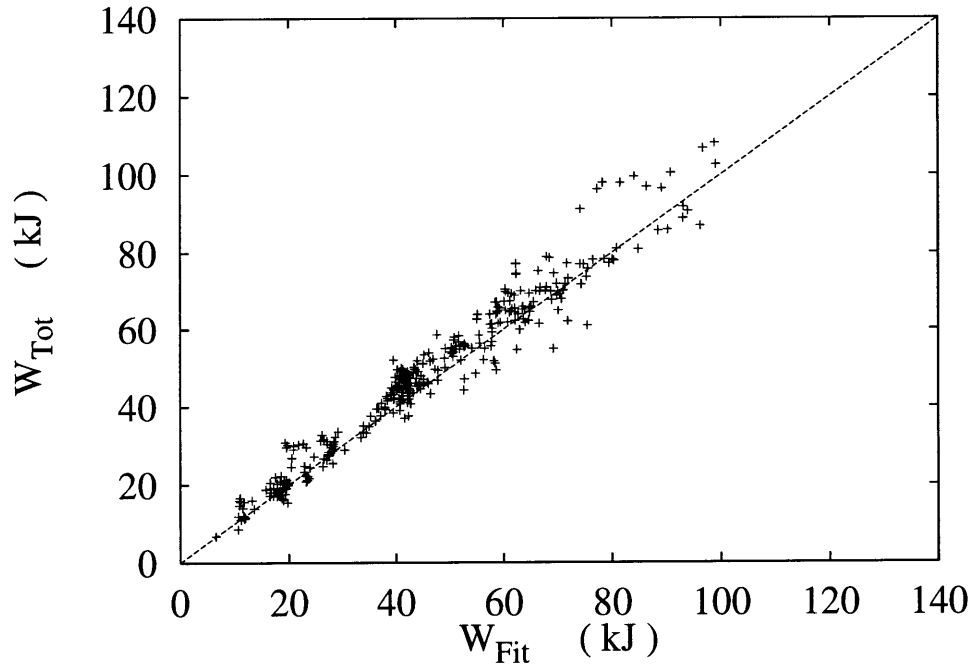

Figure C-2: Comparison of W scaling in Eq. (4.22) with discharges from Alcator C-Mod

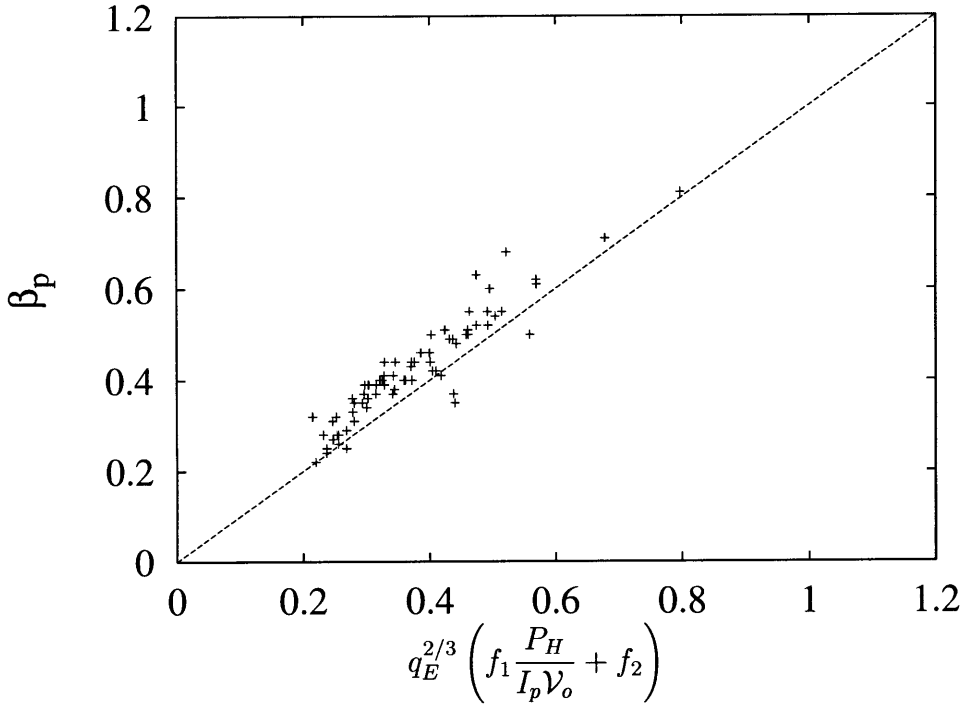

Figure C-3: Comparison of β_p scaling in Eq. (4.17) with discharges from DIII-D

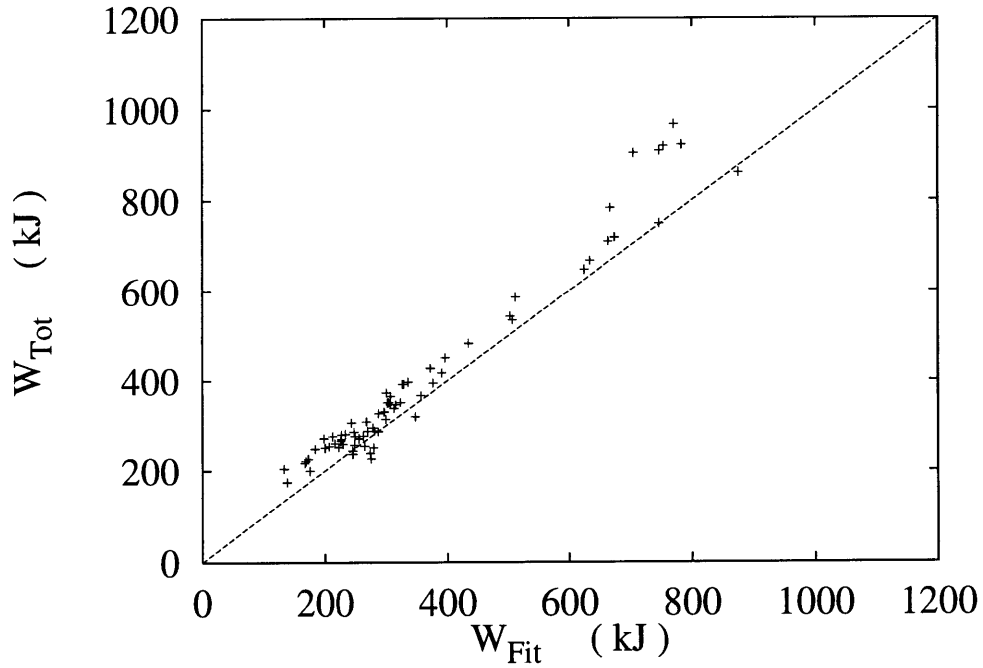

Figure C-4: Comparison of W scaling in Eq. (4.22) with discharges from DIII-D

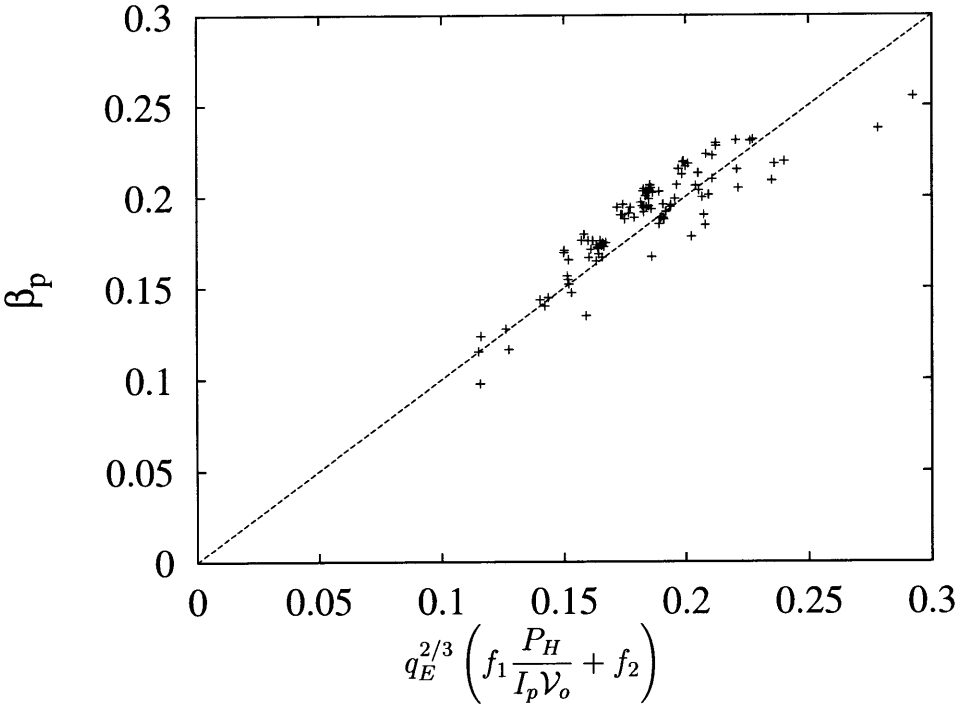

Figure C-5: Comparison of β_p scaling in Eq. (4.17) with discharges from JET

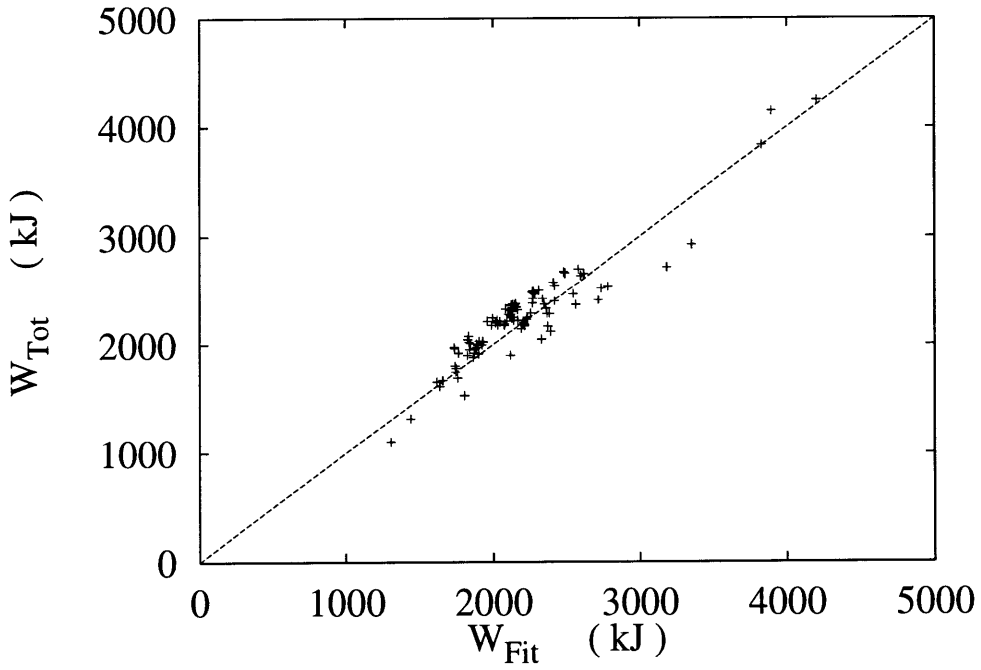

Figure C-6: Comparison of W scaling in Eq. (4.22) with discharges from JET

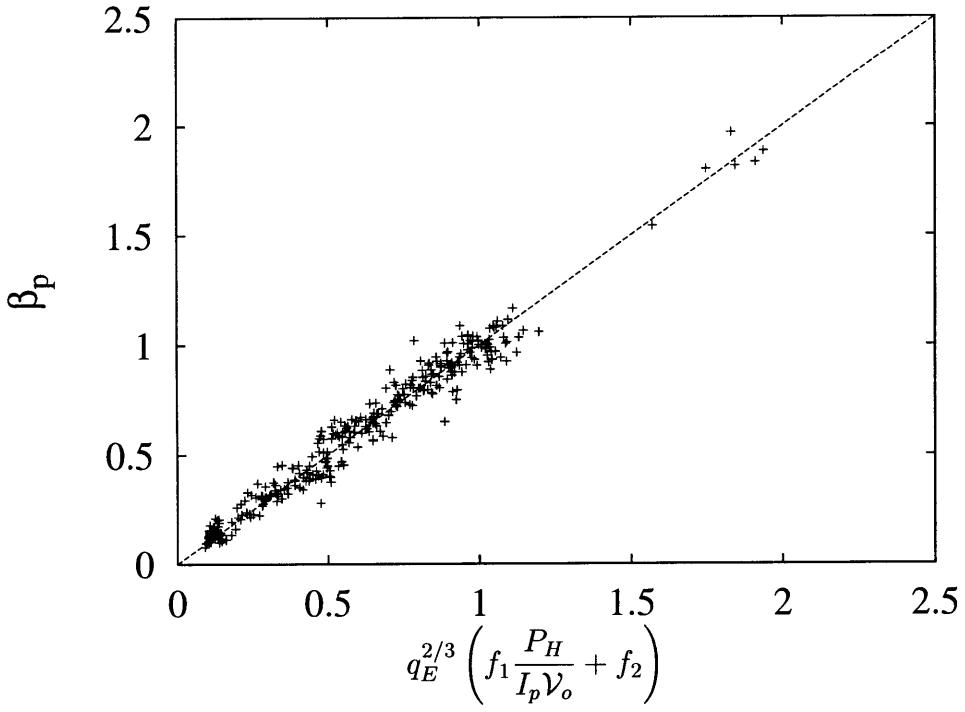

Figure C-7: Comparison of β_p scaling in Eq. (4.17) with discharges from JT-60

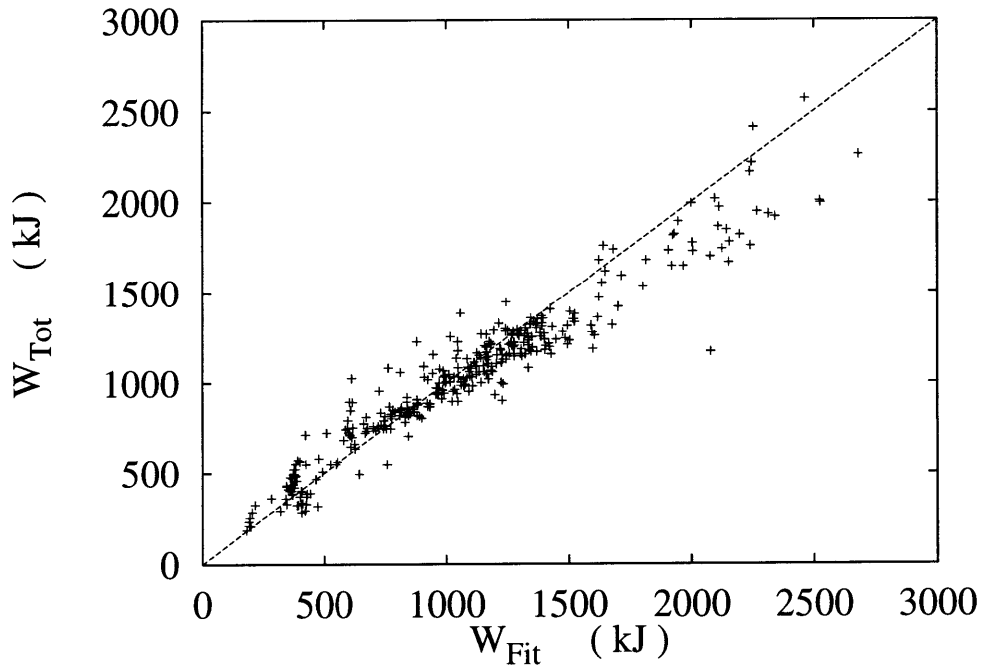

Figure C-8: Comparison of W scaling in Eq. (4.22) with discharges from JT-60

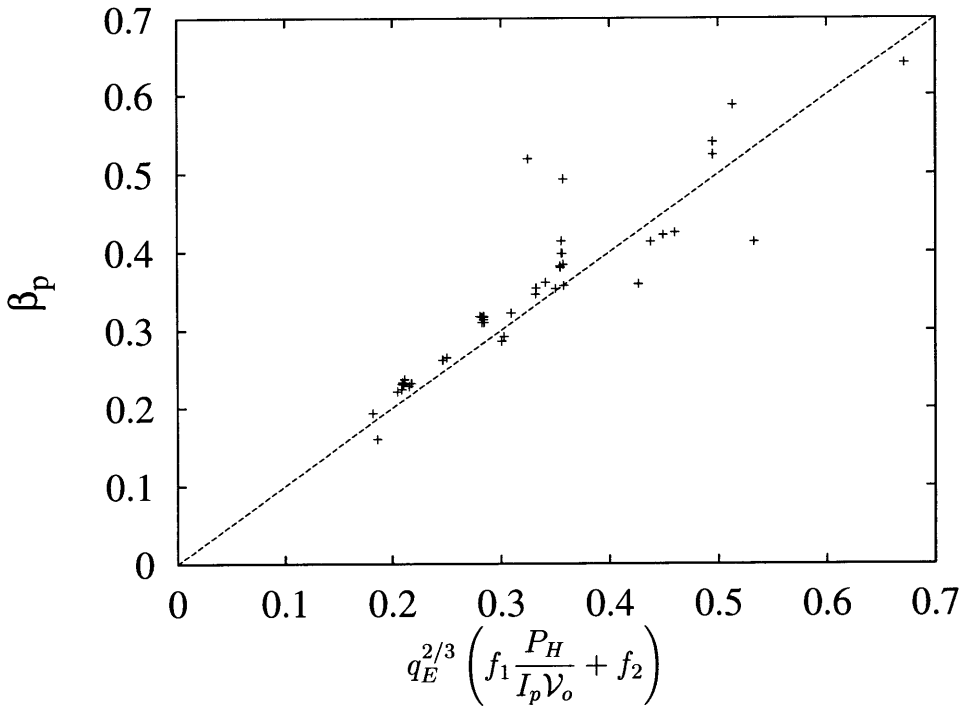

Figure C-9: Comparison of β_p scaling in Eq. (4.17) with discharges from TFTR

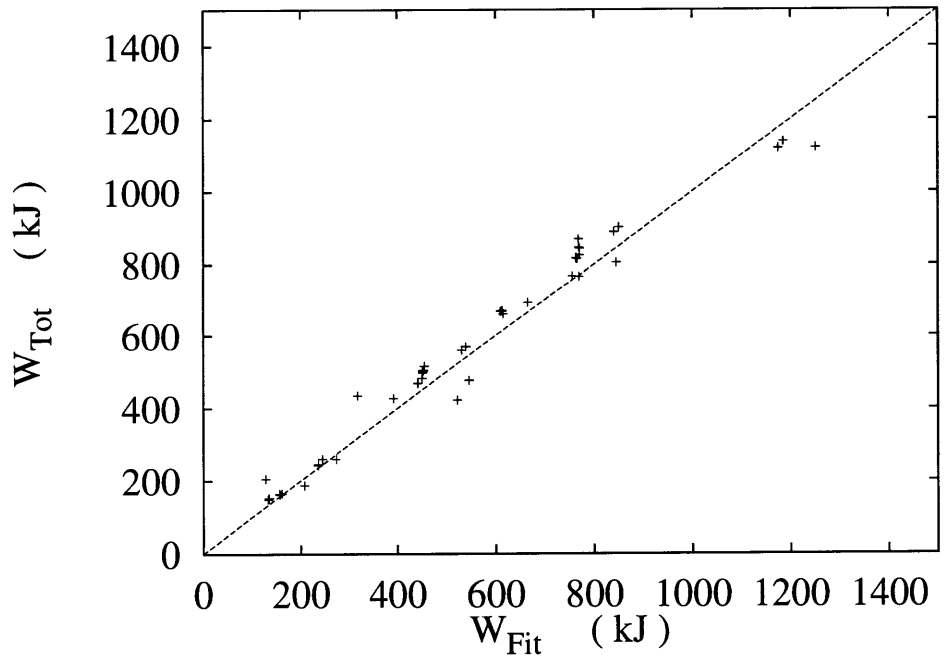

Figure C-10: Comparison of W scaling in Eq. (4.22) with discharges from TFTR

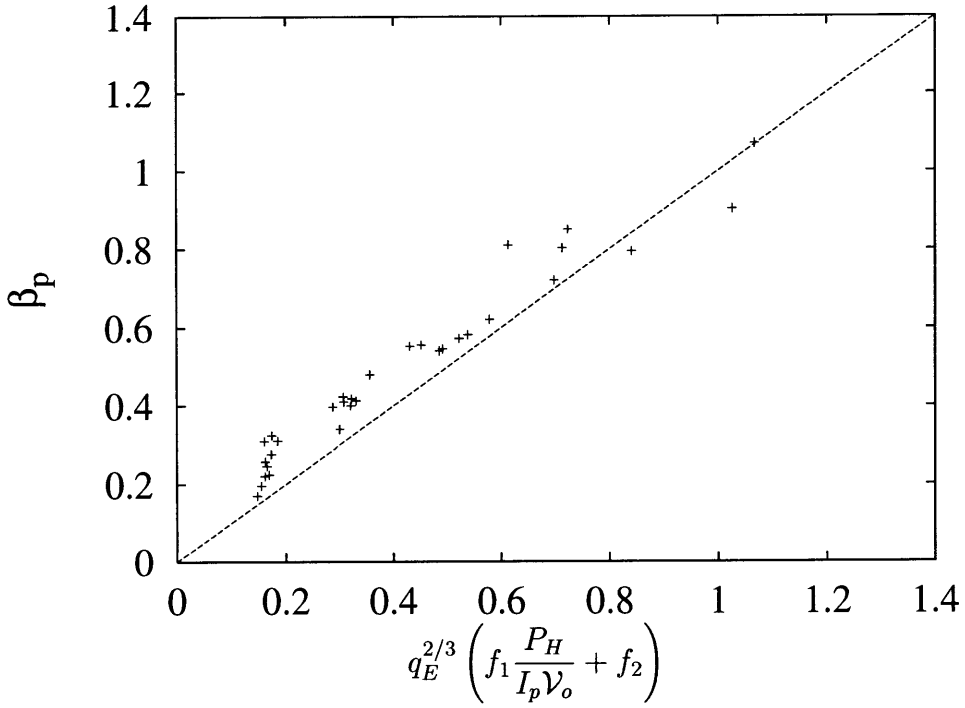

Figure C-11: Comparison of β_p scaling in Eq. (4.17) with discharges from PDX

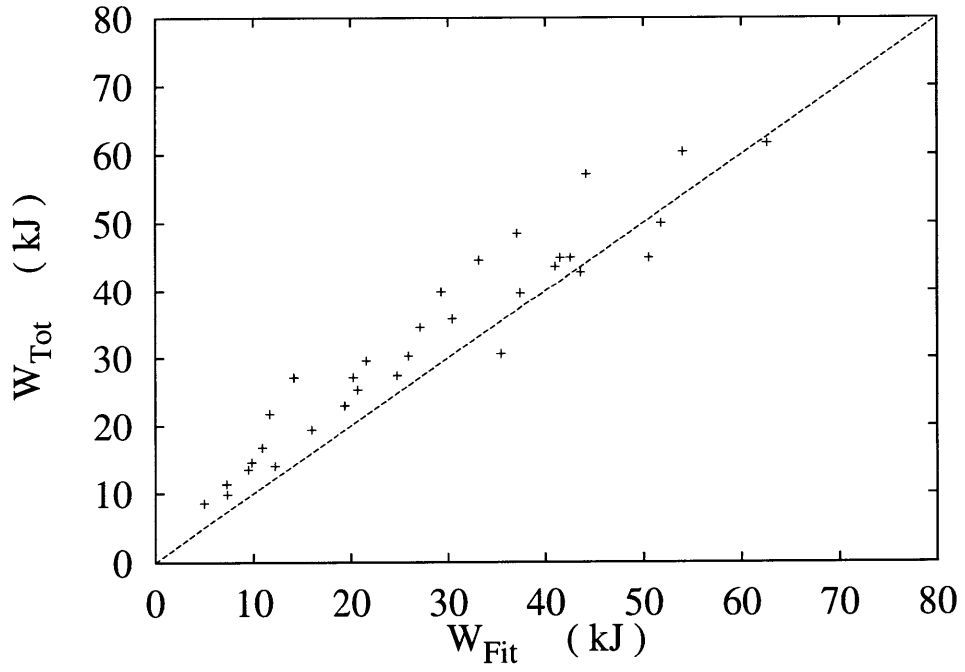

Figure C-12: Comparison of W scaling in Eq. (4.22) with discharges from PDX

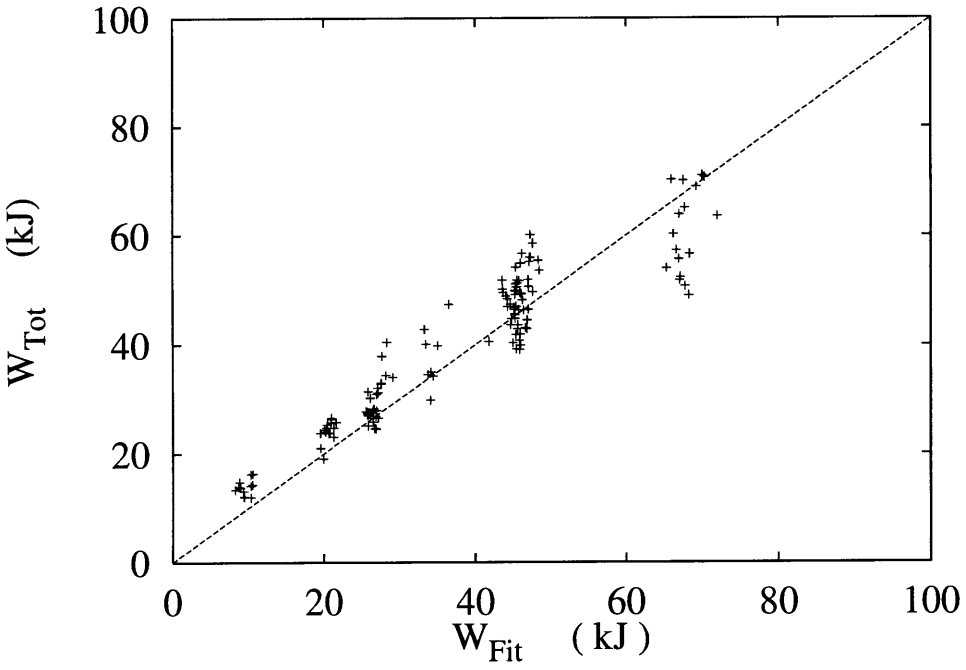

Figure C-13: Comparison of W scaling in Eq. (4.22) with discharges from FTU

Appendix D

Comparison of H-Mode Scaling with ITER Database

In this appendix, a comparison of the scaling discussed in Sec. 4.9 is presented. The experimental data is from the H-mode database assembled for the ITER project [80]. Discharges were selected from this database based on the selection criteria discussed on page 96. Scalings are shown in both dimensionless form for β_p and in terms of the total stored energy W. The machines considered are JET, DIII-D and Alcator C-Mod.

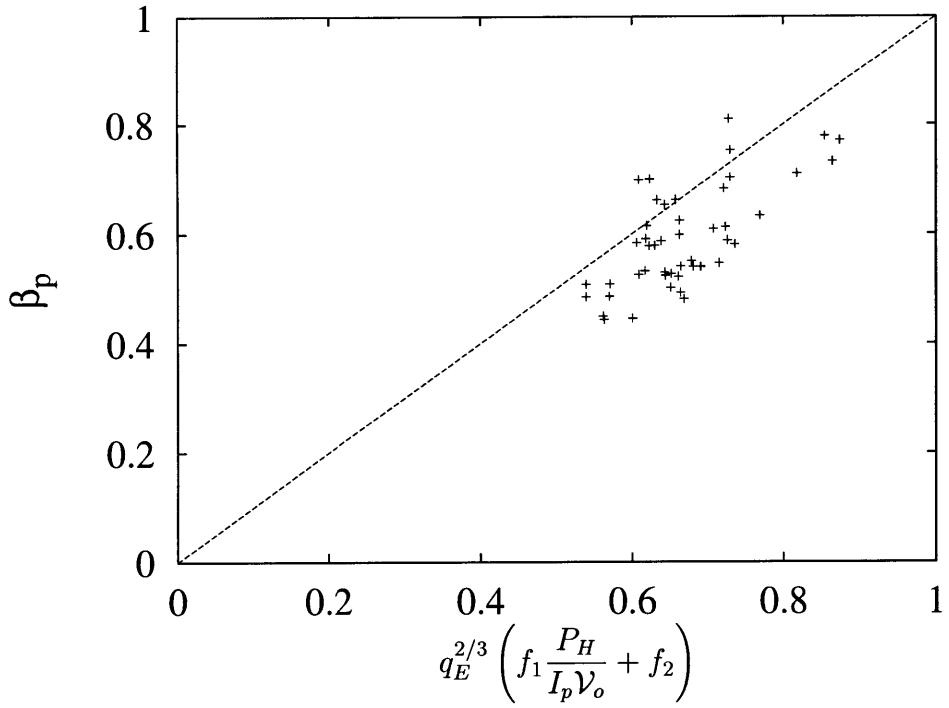

Figure D-1: Comparison of β_p scaling in Eq. (4.56) with H-mode discharges from Alcator C-Mod

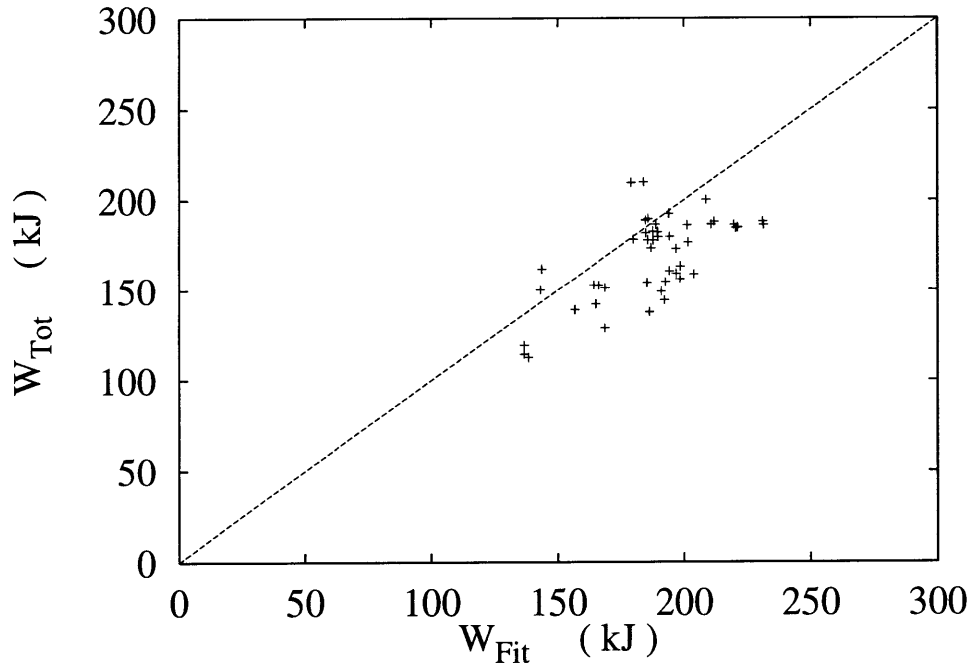

Figure D-2: Comparison of W scaling with H-Mode discharges from Alcator C-Mod

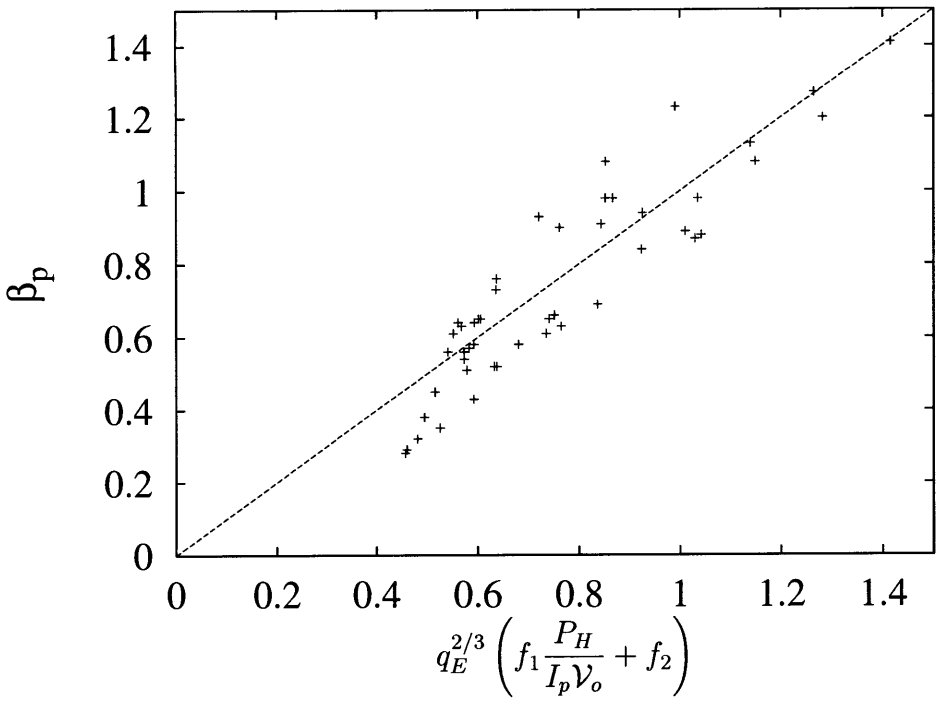

Figure D-3: Comparison of β_p scaling in Eq. (4.56) with H-Mode discharges from DIII-D

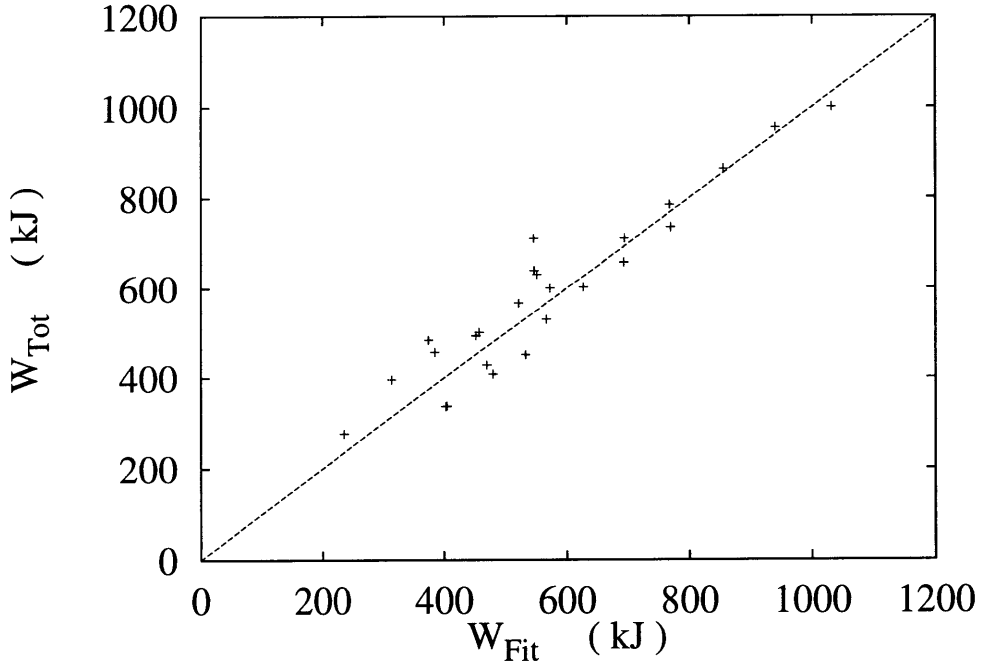

Figure D-4: Comparison of W scaling with H-Mode discharges from DIII-D

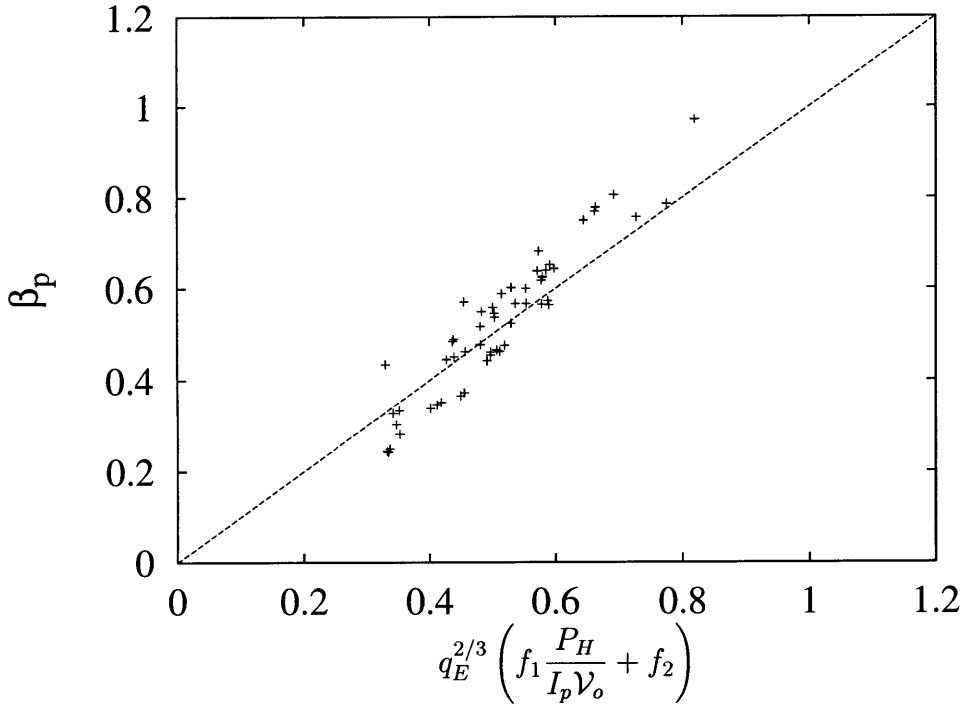

Figure D-5: Comparison of β_p scaling in (4.56) with H-Mode discharges from JET

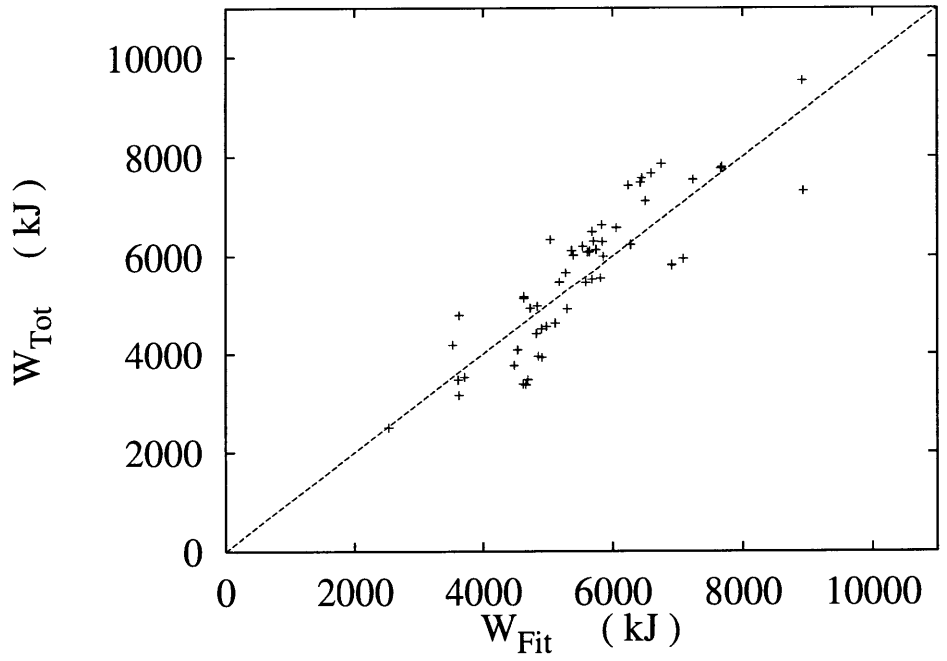

Figure D-6: Comparison of W scaling with H-Mode discharges from JET

Appendix E

Fortran Code

E.1 Diffusion Coefficient

The following subroutine implements the thermal transport coefficient discussed in Sec. 4.5 for use in the BALDUR code. It replaces the subroutines "cmg.f" in the original BALDUR code. An effort was made to use the same notation for the basic variables in Eq. (4.40).

```
c  Subroutine calculates the electron thermal diffusion coefficient
c  for generalized  2D geometry based on the model proposed by
c  Coppi and Daughton : presented at IAEA, paper F1-CN-64/GP-14, 1996
c  and at 1997 EPS Conference, "Composite Transport Coefficients
c  for well confined plasmas",  paper p3.109
c
c  It returns D_e in units of cm^2/sec

      subroutine cmg(icmg)

      include '../com/cbaldr.m'
      include '../com/commhd.m'
      include '../com/comhd3.m'
      include '../com/cd3he.m'
      include '../com/cmg.m'

      common/cmgub/xdpdi(n9),xnueub(n9),xbetub(n9),xrbpol(n9),r_p(n9),
     &r_t(n9)
      dimension zai(n9)
      dimension zp(n9),zptot(n9)
```

```
      real nue,nustar

c   computed at zone boundaries
c   units cm2/s; alcmg = 0.25, epscmg = 0.2 standard
c     alpcmg = 0.7; gcmg=4.5 H-mode, 9.0 L-mode
      jza=mzones
c
c   toroidal current curtor in (amps) from torcur
c   tes(.,.,) *useh in keV, lengths in (m) from deqbald
      do 8 jz=lcentr,mzones
      zstara(jz)=0.
      xbetub(jz)=0.
      do 4 ih=1,mhyd
    4    zstara(jz)=zstara(jz)+rhohs(ih,1,jz)/aspec(ih)
      if(mimp.eq.0) go to 8
      do 6 ii=1,mimp
       ji=ii+lhydn
    6   zstara(jz)=zstara(jz)+c2mean(ii,1,jz)*rhois(ii,1,jz)/aspec(ji)
    8   zstara(jz)=zstara(jz)/rhoels(1,jz)

c  Find the maximum pressure gradient

      jmax=0
      dpmax=0
      do 19 jz=lcentr+1+cfutz(493),mzones-1
      dpdr=-(rhoels(1,jz+1)*tes(1,jz+1)-rhoels(1,jz-1)*tes(1,jz-1))
     & /(xbouni(jz+1)-xbouni(jz-1))*avi(jz,5,1)
      if (abs(dpdr).gt.dpmax) then
         dpmax=dpdr
         jmax=jz
      endif
 19   continue
      bpolsq1=avi(mzones,7,1)*(r0ref*bpoli(mzones)*avi(mzones,2,1))**2
      pref=dpmax*avi(jmax,15,1)*usie*usid
      betastar=(8*3.1415927e-7*pref)/bpolsq1

c  Overall constant for Fd  -  see Eq. 4.40 - 4.41

      c2=cfutz(492)

c  Constant in Fd - see Equation 4.41

      c3=cfutz(494)

c  Constant in V_0 -  see Equation 4.18

      c1=cfutz(495)
```

```
c  Average Mass

      ai=cfutz(496)

c Various other definitions

      qstar=rmini**2*b0ref*avi(mzones,16,1)/(rmaji*curtor(mzones)*2e-7)
      alpha_v=0.18
      a=rmini*100
      R=rmaji*100
      c=3e10
      pi=3.1415927
      ratio=1840.
      tev=tes(1,jmax)/1.6022e-12
      wpe=5.64e4*sqrt(rhoels(1,jmax))
      wpi=1.32e3*sqrt(rhoels(1,jmax))
      di=c/wpi
      de=c/wpe
      wce=1.76e7*(bzi*1e4)
c  Definition of Fd - See Eq. 4.41
      fd=c2*(a/di)**0.5*ai**0.25*(c3*10.*betastar/qstar**0.67*
     &(wce/wpe)**0.33/ai**0.5-0.25*R/a)

      nue=2.91e-6*rhoels(1,jmax)*cloges(1,jmax)/tev**1.5
      vthe=4.19e7*sqrt(tev)
      omegab=sqrt(a/r)*vthe/(qstar*r)
      nustar=nue/omegab*(r/a)
c  Definition of Voltage Scale - See Eq. 4.18
      vo=alpha_v*(wpi*de**2*nue/vthe**2)**0.4*tev*(nustar/(1+nustar)+
     &c1*(wpi/nue)**0.67*(c/(4*pi*vthe))**2/ratio)

c     Calculate coefficient

      do 20 jz=lcentr+1,mzones
      xcmg0(jz)=(vo/300)*curtor(jz)*uisi/(tes(1,jz)*rhoels(1,jz))*
     &avi(mzones,12,1)/(avi(jz,3,1)**2*avi(jz,6,1)*uisl)*fd
 20   continue

      do 104 j=lcentr,mzones
      zai(j)=0.
      do 102 ih=1,mhyd
 102  zai(j)=zai(j)+rhohs(ih,1,j)*aspec(ih)
      do 103 ii=1,mimp
 103  zai(j)=zai(j)+rhois(ii,1,j)*aspec(ii+lhydn)
      zai(j)=zai(j)/rhoins(1,j)
 104  continue
```

```
c   xnueub not well defined at mzones
      do 105 jz=lcentr,mzones-1
 105  xnueub(jz)=1.2589e-37*rgcs(jz,1)*q(jz)*xzeff(1,jz)*
     1 cloges(1,jz)*rhoels(1,jz)/tes(1,jz)**2
      xnueub(mzones)=xnueub(mzones-1)
c   calc zp on zone centers for integral volint
      do 106 j=lcentr,mzones
 106  zp(j)=rhoels(2,j)*tes(2,j)+rhoins(2,j)*tis(2,j)
      zwtot=volint(lcentr,ledge,zp,zptot)
      zwtot=zwtot/vols(jza,1)
      do 115 j=lcentr+1,mzones
 115  zptot(j) = zptot(j)/vols(j,1)
      do 116 j=lcentr,mzones
 116  zp(j)=rhoels(1,j)*tes(1,j)+rhoins(1,j)*tis(1,j)
      zbt=4.0*twopi
      do 108 j=lcentr+1,mzones
 108   xbetub(j)=zbt*(zptot(j)-
     1 zp(j))/((bpols(1,j)*r0ref*avi(j,2,1))**2*avi(j,7,1))
      xbetub(lcentr)=xbetub(lcentr+1)
c   to inc xub near r=0, use rho_G in place of ators
      zrhog = 0.5*ators(jza,1)
 1020   continue
c   total anom ion chi_i = xub = cfutz(496) * xub0
      do 112 jz=lcentr,mzones
 112  xub(jz)= 0.0

c   Total electron anom chi_e = xcmg
      do 114 jz=lcentr,mzones
 114  xcmg(jz) = xcmg0(jz)

  64  continue
      do 70 jz=lcentr,mzones
  70  dxcmg(jz)=epscmg*xcmg(jz)
c   inward pinch vxcmg; note vxcmg<0 inward
      do 72 jz=lcentr,mzones
  72  xnueub(jz)=1.2589e-37*rgcs(jz,1)*q(jz)*xzeff(1,jz)*
     1 cloges(1,jz)*rhoels(1,jz)/tes(1,jz)**2
c     zalp=0.1*alpcmg/vols(mzones,1)
      zalp=alpcmg/vols(mzones,1)*uisl**2
      do 80 jz=lcentr,mzones
  80    vxcmg(jz)=-zalp*dxcmg(jz)*(1.+4.1*sqrt(xnueub(jz)))*avi(jz,3,1)/
     1  avi(jz,2,1)
        vxcmg(mzones)=0.
      return
      end
```

Bibliography

[1] B. Coppi, M. N. Rosenbluth, and R. N. Sudan. *Annals of Physics*, 55(2):207, 1969.

[2] B. Basu and B. Coppi. *Geophys. Res. Lett.*, 15:417, 1988.

[3] B. Basu and B. Coppi. *J. Geophys. Res.*, 94:5316, 1989.

[4] A. Simon. *Phys. of Fluids*, 6(3):382, 1963.

[5] F.C. Hoh. *Physics of Fluids*, 6:1184, 1963.

[6] D. D'Ippolito and N. Krall. *Phys. of Fluids*, 17(10):1848, 1974.

[7] F.W. Perkins and J.H. Doles III. *J. Geophys. Res.*, 80(1):211, 1975.

[8] J.D. Huba, S.L. Ossakow, P. Satyanarayana, and P.N. Guzdar. *J. Geophys. Res.*, 88(A1):425, 1983.

[9] P. Liewer, S. Karmesin, and J. Brackbill. *J. Geophys. Res*, 101(A8):17119, 1996.

[10] L.M. Linson and J.B. Workman. *J. Geophys. Res.*, 75:3211, 1970.

[11] M. Kelly, M. Larsen, and C. LaHoz. *J. Geophys. Res.*, 86:9087, 1981.

[12] R.T. Tsunoda. *J. Geophys. Res.*, 86:139, 1981.

[13] E. Ott. *J. Geophys. Res.*, 83:2066, 1978.

[14] A.I. Ershkovich and D.A. Mendis. *Astrophys. J.*, 302:849, 1986.

[15] A.I. Ershkovich, J.F. McKenzie, and W.I. Axford. *Astrophys. J.*, 344:932, 1989.

[16] J.W. Dungey. *J. Atmos. Terr. Phys.*, 9:304, 1956.

[17] B. Coppi. *Non-Equilibrium Thermodynamics.* The University of Chicago Press, Chicago and London, 1965.

[18] P.J. Catto. *Phys. Plasmas*, 1:1936, 1994.

[19] P. Helander, S.I. Krasheninnikov, and P.J. Catto. *Phys. Plasmas*, 1:3174, 1994.

[20] S.I. Braginskii. *Reviews of Plasma Physics*, volume 1. Interscience, New York, 1965.

[21] R.D. Hazeltine and J.D. Meiss. *Plasma Confinement.* Addison-Wesley, 1992.

[22] D.R. Schultz, S. Yu. Ovchinnikov, and S.V. Passovets. *Atomic and Molecular Processes in Fusion Edge Plasmas.* Plenum Press, New York, 1995.

[23] R.K. Janev, W.D. Langer, K. Evans, and D.E. Post. *Elementary Processes in Hydrogen-Helium Plasmas.* Springer-Verlag, Berlin, 1987.

[24] B. Basu and B. Coppi. Plasma depletion processes in the ionosphere and the equatorial spread f. Technical Report PTP-84/18, MIT, 1984.

[25] B. Coppi and M. Rosenbluth. Collisional interchange instabilities in shear and $\int d\ell/B$ stabilized systems. In *Plasma Physics and Controlled Nuclear Fusion Research*, number CN-21/105. IAEA, 1966.

[26] B. Coppi, J. Filreis, and F. Pegoraro. *Ann. of Phys.*, 121:1, 1979.

[27] B. Basu. *J. Geophys. Res.*, 102:17305, 1997.

[28] J.D. Huba P.N. Guzdar, P. Satyanarayana and S.L. Ossakow. *Geophys. Res. Lett.*, 9:547, 1982.

[29] J.D. Huba P. Satyanarayana, P.N. Guzdar and S.L. Ossakow. *J. Geophys. Res.*, 89:2945, 1984.

[30] B. Basu and B. Coppi. Plasma depletion processes in the ionosphere and the equatorial spread f. Technical Report PTP-97/1, MIT, 1997.

[31] D. Lumma, J.L. Terry, and B. Lipschultz. Radiative and 3-body recombination in the alcator c-mod divertor. *to appear in Nucl. Fusion*, 1997.

[32] S.I. Krasheninnikov, A. Yu. Pigarov, D.A. Knoll, B. LaBombard, B. Lipschultz, D.J. Sigmar, T.K. Soboleva, J.L. Terry, and F. Wising. Plasma recombination and molecular effects in tokamak divertors and divertor simulators. *to appear in Phys. Plasmas*, 1997.

[33] P.C. Frisch. *Science*, 265:1423, 1994.

[34] A.F. Davidsen. *Science*, 259:327, 1993.

[35] R. Lallement, J.L. Bertaux, and J.T. Clarke. *Science*, 260:1095, 1993.

[36] F.L. Hinton and R.D. Hazeltine. *Rev. Mod. Phys.*, 48:239, 1976.

[37] B. Coppi and G. Rewoldt. *Phys. Rev. Lett.*, 33:1329, 1974.

[38] B. Coppi and F. Pegoraro. *Nucl. Fusion*, 17:969, 1977.

[39] B. Coppi, S. Migliuolo, and Y-K. Pu. *Phys. of Fluids B*, 2:2322, 1990.

[40] G. Rewoldt and W.M. Tang. *Phys. Fluids B*, 2:319, 1990.

[41] E. Mazzucato. *Phys. Rev. Lett*, 48:1828, 1982.

[42] T. Crowley and E. Mazzucato. *Nucl. Fusion*, 25:2055, 1987.

[43] D.L. Brower, W.A. Peebles, and N.C. Luhmann. *Nucl. Fusion*, 27:2055, 1987.

[44] B. Coppi and G. Rewoldt. *Advances in Plasma Physics*, volume 6. Interscience, New York, 1976.

[45] B. Coppi. *Riv. Nuovo Cimento*, 1:357, 1969.

[46] B.B. Kadomtsev and O.P. Pogutse. *Sov. Phys. Dokl.*, 14:470, 1969.

[47] F. Pegoraro. Odd ion instability driven by the magnetic curvature drift. Technical Report PTP-76/6, MIT, 1976.

[48] B. Coppi. In *Plasma Physics and Controlled Nuclear Fusion Research*, number CN-53/I-2-6. IAEA, 1990.

[49] B. Coppi, H.P. Furth, M.N. Rosenbluth, and R.Z. Sagdeev. *Phys. Rev. Lett.*, 17:377, 1966.

[50] B. Coppi, G. Rewoldt, and T. Schep. *Phys. of Fluids*, 19:1144, 1976.

[51] B. Coppi. *Comments Plasma Phys. Control. Fusion*, 5:261, 1980.

[52] W. Dorland, M. Kotschenreuther, M.A. Beer, G.W. Hammett, R.E. Waltz, R.R. Domingues, P.M. Valanju, W.H. Miner, J.W. Dong, W. Horton, F.L. Wailbroeck, T. Tajima, and M.J. LeBrun. In *Plasma Physics and Controlled Nuclear Fusion Research*, number CN-60/D-P6. IAEA, 1996.

[53] M. Kotschenreuther, W. Dorland, M.A. Beer, and G.W. Hammett. *Phys. of Plasmas*, 2:2381, 1995.

[54] J. Schachter. *Local Transport Analysis for the Alcator C-Mod Tokamak.* PhD thesis, MIT, 1997.

[55] T.C. Luce, C.C. Petty, and J.C.M. de Haas. *Phys. Rev. Lett.*, 68(1):52, 1992.

[56] C.C. Petty and T.C. Luce. *Nucl. Fusion*, 34(1):121, 1994.

[57] Yu.N. Dnestrovskii, Yu. V. Esipchik, S.W. Lysenko, and K.N. Tarasyan. *JETP Lett.*, 46:398, 1987.

[58] J.P. Christiansen, J.D. Callen, J.G. Cordey, and K. Thomsen. *Nucl. Fusion*, 28(5):817, 1988.

[59] J.D. Callen, J.P. Christiansen, J.D. Callen, J.G. Cordey, P.R. Thomas, and K. Thomsen. *Nucl. Fusion*, 27(11):1857, 1987.

[60] M. Kikuchi and M. Azumi. *Nucl. Fusion*, 30(11):2211, 1990.

[61] B. Coppi and C. Spight. *Phys. Rev. Lett.*, 41:8, 1978.

[62] B. Coppi and N. Sharky. *Nucl. Fusion*, 21:1363, 1981.

[63] P. Terry. *Phys. Fluids B*, 1:1932, 1989.

[64] B. Coppi. In *Plasma Physics and Controlled Nuclear Fusion Research*, volume 3, page 643. IAEA, 1994.

[65] B. Coppi and F. Pegoraro. *Phys. Fluids B*, 3:2582, 1991.

[66] P.H. Rebut, M. Brusati, M. Hugon, and P.P. Lallia. In *Plasma Physics and Controlled Nuclear Fusion Research*, volume 2. IAEA, 1987.

[67] B. Coppi, A. Airoldi, F. Bombarda, G. Cenacchi, W. Daughton, P. Detragiache, C. Ferro, M. Gasparotto, M. Haegi, L. Lanzavecchia, R. Maggiora, G.M. McCraken, S. Migliuolo, A. Pizzuto, M. Riccitelli, M. Roccella, J.A. Snipes, L.E. Sugiyama, and G. Vecchi. In *Plasma Physics and Controlled Nuclear Fusion Research*, number F1-CN-64/BP-14. IAEA, 1996.

[68] J.C. DeBoo, K.H. Burrell, S. Ejima, A.G. Kellman, and N. Ohyabu. *Nucl. Fusion*, 26:211, 1986.

[69] M. Kikuchi, T. Hirayama, K. Shimizo, K. Tani, H. Yoshida, H. Yokomizo, T. Fukuda, A. Sakasai, Y Koide, T. Sugie, H. Horiike, M. Kuriyama, H. Ninomiya, N. Hosogane, and R. Yoshino. *Nucl. Fusion*, 27(8):1239, 1987.

[70] Y. Koide and et al. *Phys. Rev. Lett.*, 72:3662, 1994.

[71] G. Mahan, B. Sales, and J. Sharp. *Physics Today*, page 42, March 1997.

[72] B. Coppi and E. Mazzucato. *Phys. Letters*, 71A:337, 1979.

[73] B. Coppi and W. Daughton. Composite transport coefficients for well confined plasmas. In 24^{th} *EPS Conference on Controlled Fusion and Plasma Physics.* EPS, 1997. paper p3.109.

[74] S.M. Kaye and the ITER Confinement Database Working Group. *to appear in Nucl. Fusion*, 1997.

[75] P.N. Yushmanov and et al. *Nucl. Fusion*, 30:1999, 1990.

[76] C.E. Singer, D.E. Post, D.R. Mikkelsen, M.H. Redi, A. McKenney, A.Silverman, F.G.P. Seidl, P.H. Rutherford, R.J.Hawryluk, W.D. Langer, L.Foote, D.B. Heifetz, W.A. Houlberg, M.H. Hughes, R.V. Jensen, G. Lister, and J. Ogden. *Computer Physics Comm.*, 49:275, 1988.

[77] J. O'Rourke. *Plasma Phys. Cont. Fusion*, 33:289, 1991.

[78] M. Greenwald, R.L. Boivin, F. Bombarda, P.T. Bonoli, C.L. Fiore, D. Garnier, J.A. Goetz, S.N. Golovato, M.A. Graf, R.S. Granetz, S. Horne, A. Hubbard, I.H. Hutchinson, J.H. Irby, B. LaBomard, B. Lipschultz, E.S. Marmar, M.J. May, G.M. McCracken, P. O'shea, J.E. Rice, J.Schacter, J.A. Snipes, P.C. Stek, Y.Takase, J.L.Terry, Y. Wang, R.Watterson, B.Welch, and S.M. Wolfe. *Nucl. Fusion*, 37(6):793, 1997.

[79] J.A. Snipes and The ITER H-Mode Threshold Database Working Group. An analysis of the h-mode threshold in iter. In 24^{th} *EPS Conference on Controlled Fusion and Plasma Physics*. EPS, 1997. paper 416.

[80] Thomsen, D.J. Campbell, J.G. Cordey, O. Kardaun, F. Ryter, U.Stroth, A. Kus adn J.C. Deboo, D.P. Schissel, Y. Miura, N. Suzuki, M. Mori, T. Matsuda, H. Tamai, T.Takizuka, S.I. Itoh, K. Itoh, and S.M Kaye. *Nucl. Fusion*, 34:131, 1994.

[81] J.A. Snipes, R. Boibin, C. Fiore, J.A. Goeta, A. Hubbord, I.H. Hutchinson, J. Irby, B. LaBombard, B. Lipschults, E.S. Marmar, J. Rice, P.C. Stek, Y. Takase, J.L. Terry, and S.M. Wolfe. Enhanced d_α,h-modes in alcator c-mod. In 24^{th} *EPS Conference on Controlled Fusion and Plasma Physics*. EPS, 1997. paper 415.